On-Orbit Performance and Calibration of the Soft X-ray Telescope on *Yohkoh*

Loren W. Acton

Abstract This paper documents details of the on-orbit performance, data problem solving, and calibration of the *Yohkoh* Soft X-ray Telescope (SXT) experiment. This information is important to a full understanding of the strengths and weaknesses of the SXT data set.

Section 2 presents an example of SXT flare data and its analysis. Section 3 provides a summary of SXT calibration issues and how they have been addressed. The remainder of the paper presents details of work by the experiment team to understand and ameliorate the many instrument anomalies and changes which impacted the observations. Section 6 discusses the accuracy of *Yohkoh* pointing determination.

Keywords: Corona, Flares, Instrumental Effects, X-Ray Bursts, Data Management, Data Calibration

Table of Contents

✉ L. W. Acton
e-mail.acton@physics.montana.edu

Department of Physics, Montana State University, P.O. Box 173840, Bozeman, MT 59717-3840 USA

1. Introduction

Scientific operation of the Japan-US-UK solar activity mission *Yohkoh* extended from September 1991 to mid-December 2001. The *Yohkoh* mission and instrumentation are described in the collection of articles edited by Švestka and Uchida (1991). The individual papers are also available on the *Yohkoh* Legacy Archive (YLA) website (Takeda *et al.*, 2009; Takeda, 2015). The solar observations by *Yohkoh* are of continuing scientific importance and have been archived in their entirety in the YLA (http://solar.physics.montana.edu/ylegacy/). The user-friendly YLA includes extensive documentation on mission operations and data search, browse and reference resources as well as fully reduced and calibrated data, flare lists, movie makers, etc. the *Yohkoh* data archive at the Solar Data Analysis Center of NASA Goddard Space Flight Center carry all mission data but without all of the ancillary resources available at the YLA.

The soft x-ray telescope (SXT) was a primary *Yohkoh* instrument (Tsuneta *et al.*, 1991). SXT operating modes were very flexible but the telescope normally acquired full sun images of the quiet corona (Full Frame Images or FFI) at five arcsec angular and approximately five minute temporal resolution through one of five thin-film x-ray analysis filters (Table 6). In parallel, partial sun images (Partial Frame Images or PFI) were acquired of, usually, the brightest active region at full angular resolution (2.455 arcsec pixel) and about 30 second temporal resolution with automatic exposure control. In flare mode FFIs were not acquired so that the full SXT telemetry allocation could be devoted to PFI observations with a time resolution as short as 2.4 seconds, depending on the designated size of the observing region, also with automatic exposure control.

The SXT acquired over 8.2×10^5 full sun and 5.9×10^6 partial sun images between 3 September 1991 and 14 December 2001. The full-sun data have had short and long exposures combined (level-2 products) into 3.0×10^5 SXT Science Composite (SSC) images to increase the intensity range of each image. Each SSC has a corresponding statistical uncertainty image. The most cosmetically perfect 296 574 of the thin-filter level-2 composites have been processed to level-3 for cinematographic viewing and morphological analysis. These SXT observations were unprecedented in resolution and cadence and remain a valuable and unique record of high-energy solar activity from the peak of sunspot cycle 22 to the peak of cycle 23.

2. Flares of 6 February 1992

2.1. Flare Observations

To illustrate the richness of SXT data we have chosen a west limb flare recorded early in the mission. On 6 February 1992, beginning at 03:16 UT, *Yohkoh* recorded a flare (GOES class M7.6) which was well observed by both the Soft (SXT) and Hard (HXT) X-ray Telescopes. The *Yohkoh* flare flag was triggered at 03:16:05 at which time the PFI field of view moved from heliographic S16W34 to N06W89, the location of the flare, and the PFI flare sequence was initiated. This
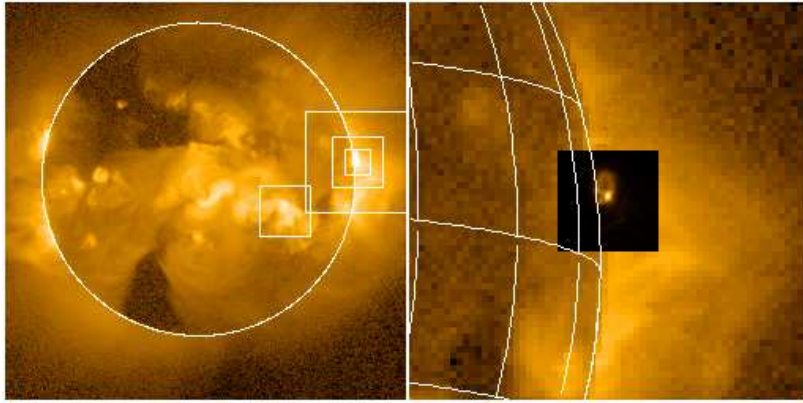
Figure 1. Left: Composite FFI image comprising a 2668 ms exposure taken 6 Febraury 1992 03:13:31 and a 78 ms exposure at 03:15:39 using the AlMg filter. The solar limb is drawn in and the white squares show the position and size of PFI fields of view for this *Yohkoh* orbit. Right: Portion of FFI with co-aligned PFI inset, a Be filter exposure taken at 03:16:47, shown in Figure 3 at larger scale. North is up and east is right on all figures.

particular flare program took a series of 64×64 pixel full resolution (FR) images interleaving thin aluminum (Al.1), thick aluminum (Al12), narrow-band optical (NB), and beryllium (Be) filters (see Table 6 for filter details). This sequence was occasionally interrupted by quarter and half resolution Al.1 images at fixed exposure intended to record any faint ejecta over a larger field of view. The image cadence was about two seconds.

The GOES x-ray event comprised 3 individual flares, all anchored in NOAA active region 7030 at N05W82 heliographic. Figure 1, an FFI obtained shortly before the *Yohkoh* flare flag was triggered, shows a bit of CCD saturation at the west limb from the flare emission. The inset, obtained shortly after the flare flag, clearly shows the loop-top emission of flare A.

Figure 2 displays several light curves of flare features discussed below. Note that, as revealed by Figure 1 and the GOES light curve, the gradual loop-top flares A and B have begun well before the flare flag was triggered.

Figure 3 presents an SXT Be filter image of each of the 3 flares near the time of their peak emission. These peak times are indicated by vertical dotted lines on Figure 4, a figure created to show the spatial evolution of the flare emission. Initially, the loop-top kernels dominate. Later, the brightest pixel of the Be images shifts to the hard x-ray (HXR) loop in the north. The softer Al12 and Al.1 channels follow about 1 minute later. The movement of the brightest soft x-ray (SXR) emission toward the top of the north loop over the following ten minutes is evident from the figure. Very roughly, the plane-of-sky movement of this brightest feature corresponds to a velocity of approximately 30 km sec^{-1}. The flare features are resolved by the SXT apart from possible arcsec substructures within the features. The FWHM of the SXT point spread function (PSF) at this position on the image plane is about 2.1 arcsec (Martens, Acton, and Lemen, 1995). The pixel size is 2.455 arcsec (Tsuneta *et al.*, 1991).

The brightest x-ray kernels of loop-top flares A and B do not appear to move. Flare HX, on the other hand, brightens first at its easternmost footpoint in time
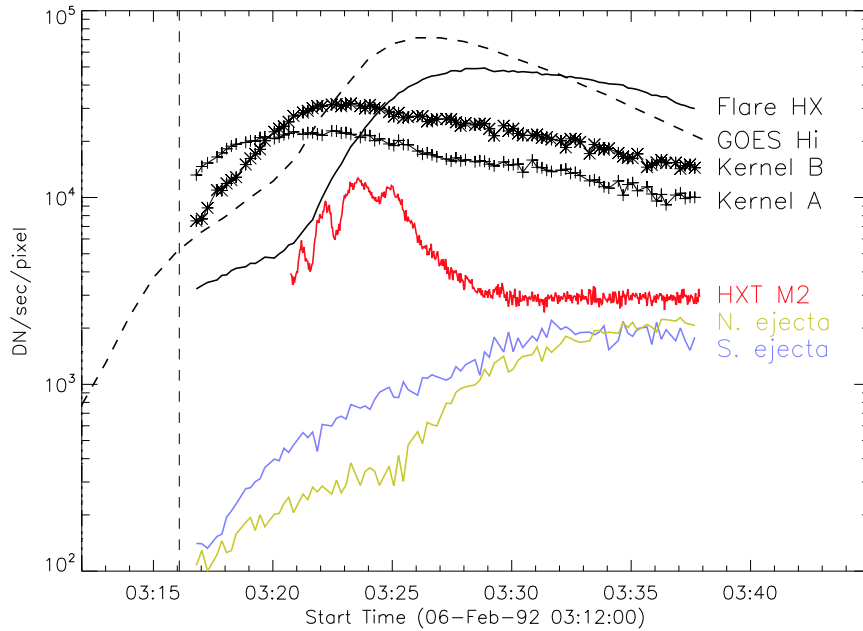
Figure 2. X-ray light curves of the indicated features. The SXT curves and abscissa scale refer to Be filter data. The GOES and HXT curves are scaled for convenience. The broken vertical line shows the time of the *Yohkoh* flare flag. Figures 3 and 9 show the image areas averaged for the various light curves.

coincidence with the hard x-ray burst. Thereafter the peak emission climbs up the loop to reach the top at the time of maximum SXR brightness. The dynamic evolution of this series of separate flares is well illustrated in the time-lapse movie comprised of the SXT Be 119μm filter images with 2.455 arcsec pixel and 15 second time resolution. This movie, entitled SXT_LIMBFLARE, is available as online material.

The HXT observations of flare HX are presented in Figure 5 (Sato *et al.*, 2006; Takeda, 2015). While flares A and B were not accompanied by detectable HXR emission there are strong time and spatial correlations of the HXR and SXR brightenings of flare HX. These are discussed in section 2.2.

2.2. Flare Analysis

The SXT image sequences used in the following sections have been co-aligned, corrected for CCD background and x-ray scattering, and exposure normalized by the use of the SolarSoft program *sxt_prep.pro*.

The SXT flare sequence employed for observation of the 3 February 1992 flares cycled through the Al.1, Al12, and Be filters. This enables derivation of a two-temperature differential emission measure (DEM) distribution. We have used the program *firdem.pro* to analyze the SXT data. DEM examples are shown in Figure 6. While only an approximation of real DEM, these results represent
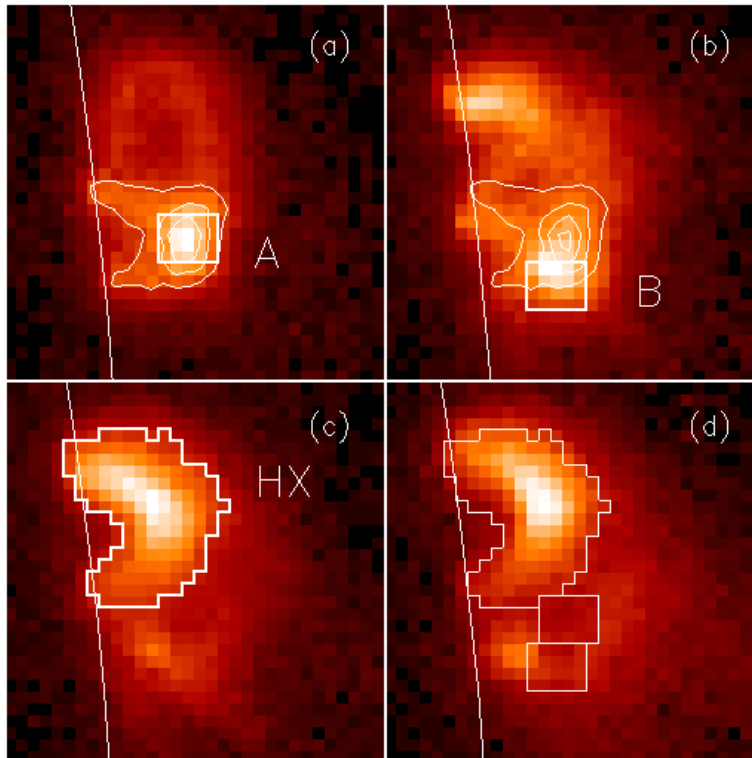
Figure 3. Images of the 6 February 1992 limb flare acquired at 03:16:47 (a), 03:22:39 (b), 03:29:03 (c), and 03:37:39 (d). Images a, b, and c were taken near the time of peak intensity of flares A, B, and HX. The heavy white contour lines in a, b, and c (all reproduced in panel d) show the flare areas chosen for analysis. The flare contour lines of panel a are reproduced in panel b to demonstrate that flare B takes place on a distinctly different loop that flare A.

Table 1. Flare Areas and Volumes

Feature	Area (pixels)	Thickness (pixel)	Volume (cm^3)
Flare A	20	4	4.3×10^{26}
Flare B	20	4	4.3×10^{26}
Flare HX	136	9	6.6×10^{27}

the coronal plasma properties better than a simple two-filter ratio solution. The temperatures presented below are DEM-weighted average temperatures from the *firdem.pro* curves . The resulting time sequences of temperature and density (based on the feature volumes from Table 1) are presented in Figure 7.

As illustrated in Figure 5 flare HX was well observed by HXT, sith signals above 30 keV in the HXT-M2 channel. We have searched the SXT observations for SXR emission time-correlated with the HXT-M2 bursts. Our results are
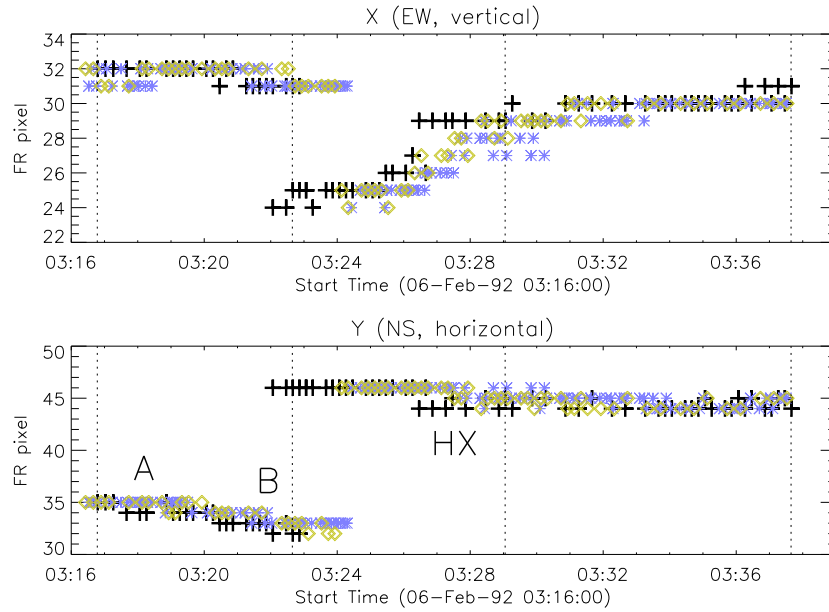
Figure 4. Position (pixel number) of the brightest pixel, with time, for each x-ray analysis filter. The letters denote which flare was dominant at the time. The dotted vertical lines indicate the the times of the images displayed in Figure 3.

displayed in Figure 8 showing a substantial area of correlation at the north footpoint of flare HX and a hint of much weaker correlation at the south footpoint of the HX loop. The strongest correlation (0.62) is in pixel (23,46), indicated in red in Figure 9. The correlation area shown in Figure 9 comprises all pixels with correlation greater than 0.4.

The right panel of Figure 8 displays the x-ray light curves through the correlation interval. For our correlation analysis the low frequency component was removed by subtracting a boxcar-smoothed time sequence with a boxcar width of approximately 110 seconds from each light curve. The analysis was done separately for each SXT filter. Each displayed the strongest correlation in pixel (23,46). The correlation map of Figure 8 is the average of the three individual filter maps. Note that the highest intensity contour of Figure 8 is precisely above the pixel of strongest correlation (23,46).

2.3. Flare Summary

The global properties of this flare event are summarized in Figure 9. The SXT narrow-band visible light image clearly shows the NOAA sunspot region 7030 and its surrounding faculae at the limb. SXT image pixels of particular interest in the discussion to follow are indicated. The right panel, a log-scaled sum of Be filter images of the entire event, reveals 2 beams of ejecta associated with the flares, the general diffuse brightening of the region, and a small loop which brightened to the south of the flaring region.
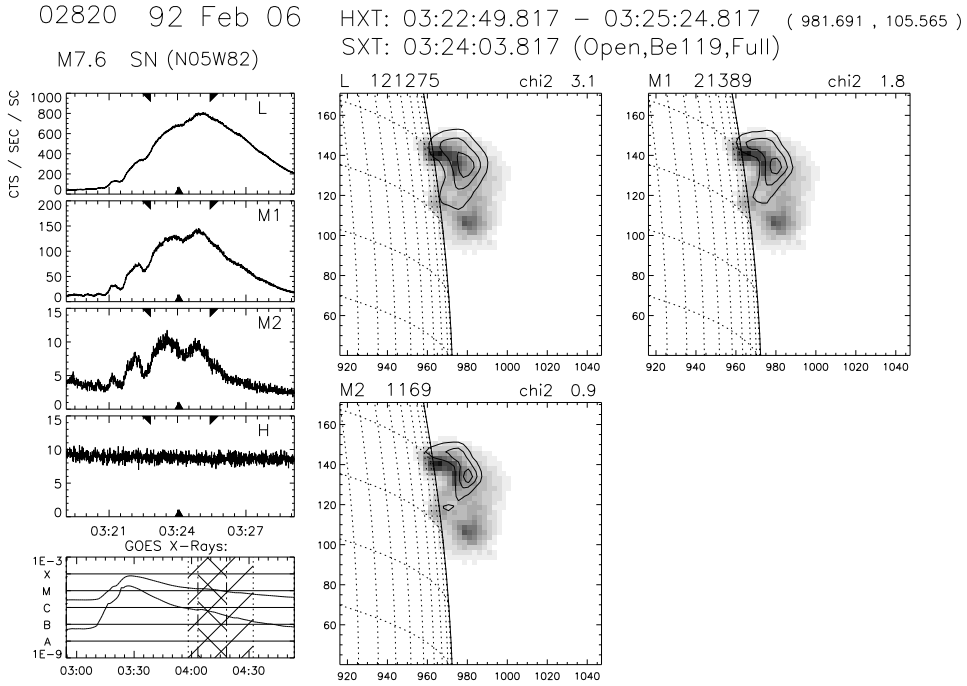
Figure 5. Left hand column displays HXT and GOES light curves. Upper tick marks denote the time interval of the HXT data used to create the HXT flare images shown by contour lines in the three frames to the right. The lower tick mark denotes the time of the SXT Be filter image underlaid on the HXT contours. It appears that at this time the brightest portion of the SXR loop lies below the HXR loop by about five arcsec (4000 km).
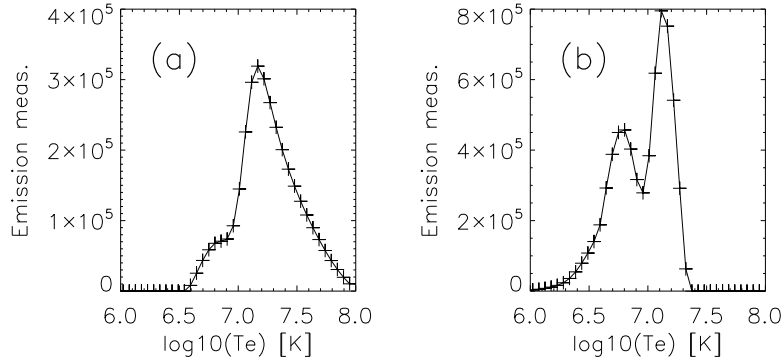
Figure 6. Examples of DEM for flare HX. Panel (a) is for 03:24:03 near the peak of the HXR flare. Panel (b) shows the DEM for 03:37:15 in the flare decay phase. Units of emission measure are per 0.05 step in $\log 10(T_e)$.
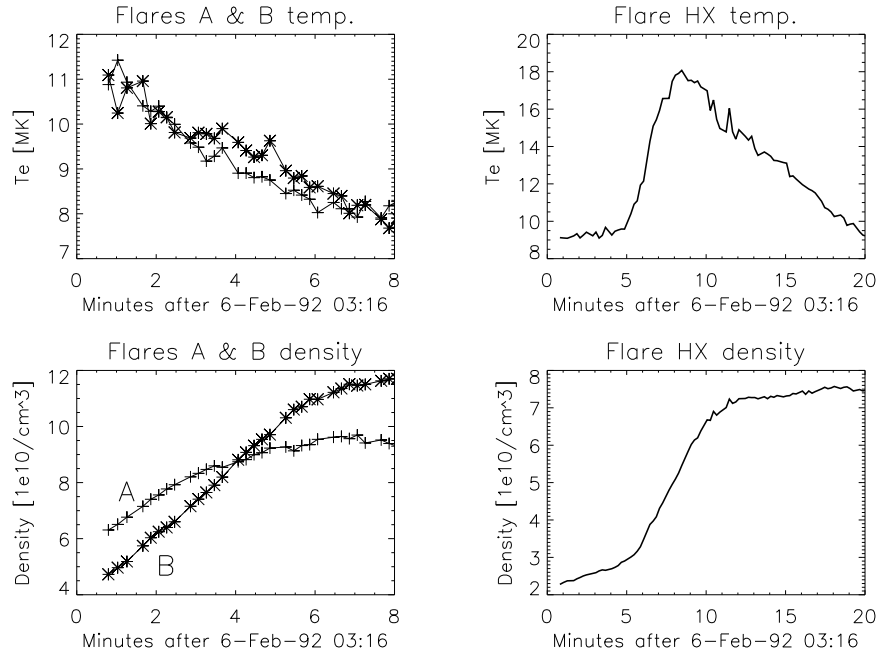
Figure 7. Temperature and density, versus time, for flares A, B, and HX. Areas sampled are shown in Figures 3 and 9. Volumes estimated for each feature are given in Table 1.
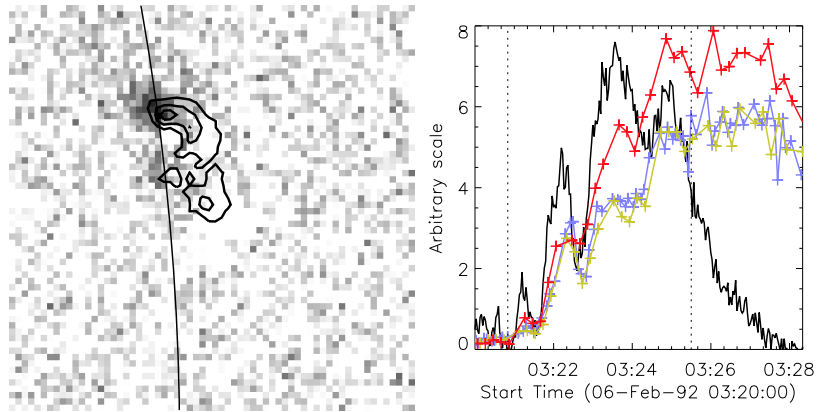
Figure 8. Left: Time sequence correlation map of HXR and SXR emission overlaid with solar limb and contours of the Be-filter image of 6-Feb-92 03:24:03. Right: Light curves of HXT-M2 (black), SXT Be (red), Al12 (yellow), and Al.1 (blue). The SXT light curves are for pixel (23,46). Dotted vertical lines define the time interval used in the correlation analysis.

Figure 9. Left: Visible (431 nm) image obtained at 03:16:11 with the solar limb draw in. Blue contours are from the Be filter image taken at 03:16:47 and yellow contours from the image acquired at 03:28:13 near the peak of flare HX. The white and red pixels at upper left is the area where SXR brightenings with correlation above 0.4 with 30-50 keV HXR bursts (see Figure 8). The 3 white pixels to the right denote the locations of the brightest pixels of the 3 flares. Right: Log-scaled sum of 88 Be-filter images acqu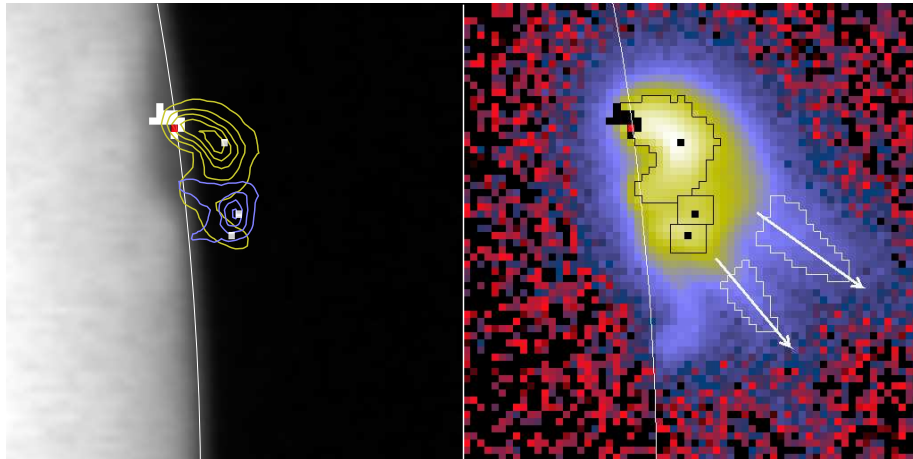ired between 03:16:47 and 03:37:39. North is up. Arrows indicate the direction of flare ejecta. Black single pixels correspond in location to the white pixels in the left image. Black contours outline the analyzed areas of flares A, B, and HX. Black and white contours identify the areas averaged to produce the light curves in Figure 2.

The 6 February 1992 west limb flare complex holds some very interesting comparisons. Flares A and B are identical twins for which the intense flare kernel forms and stays at loop-top. Both flares had attained maximum temperature in advance of the first SXT observations and increased in density and intensity even as the kernels cooled. These flares produced a jet of ejecta that was already in progress at the time of first SXT observation. Doschek, Strong, and Tsuneta (1995) have analyzed four different loop-top flare kernels in detail, including results from the *Yohkoh* bent crystal spectrometer (BCS) in their investigation. Their results for temperature and density are broadly consistent with the loop-top kernels of the 6 February 1992 flare. Preś and Kołomański (2009) have considered loop-top flares observed by SXT, Trace, EIS, and RHESSI and conclude that loop-top x-ray sources are genuinely diffuse rather than filamentary.

Flare HX was a different kind of beast. Here there was a strong correlation in location and time between HXR and SXR. The initial action was localized at the north footpoint of the flare and the SXT loop appeared to fill from that location. Initially the brightest part of the SXR loop appeared to lie below the HXR loop but, with time, it rose to that location (see online movie SXT_LIMBFLARE).

A more in-depth study of these flares is being prepared for publication.

3. SXT Calibration

All elements of the SXT optical train (section 5) were calibrated in the laboratory. End-to-end testing of the SXT under vacuum verified focus and, although not rigorously in flight configuration, were consistent with piecewise calibration results. SXT Calibration Note 5 (Lemen and Hudson, 1990), 29 (Acton, 1992), and 30 (Lemen, 1992), which are available in the YLA, detail aspects of pre-launch calibration and testing

Several items important to the calibration of the SXT are discussed in this section.

- X-ray scatter.
- X-ray vignette.
- Entrance filter failures.
- Analysis filter failures.
- Contamination of the x-ray mirror.
- Contamination of the CCD.
- Change in gain of CCD amplifier.
- Ionizing radiation damage to the CCD.
- Damage to the CCD by high energy particles.
- Errors and uncertainties.

3.1. X-ray Scatter

Figure imperfections and dust cause x-rays to scatter off of grazing incidence x-ray mirrors (Zhao and Van Speybroeck, 2003; Spiga, 2007). Most scattering goes into the axial plane, i.e., perpendicular to the mirror surface (Aschenbach, 1985).

Although the point spread function of the SXT was well characterized the laboratory data were inadequate to define the scattering wings (Martens, Acton, and Lemen, 1995). Because the *Yohkoh* flare flag is inoperative during predicted passages through the south Atlantic anomaly (SAA) FFI images continue to be acquired. Flares occurring during this period have strong overexposure at the flare site but with scattering wings ("starburst" images) well recorded, such as is illustrated in Figure 10. Several studies of such starburst images are presented in http://solar.physics.montana.edu/ylegacy/observ_notes.html. The scatter correction algorithms have been used in studies of coronal holes and other faint coronal structures, e.g., (Hara *et al.*, 1994; Foley, Culhane, and Acton, 1997). The SolarSoft program *sxt_decon.pro* corrects by deconvolution, as best we know how, for scattering. Unfortunately, although the scattering goes approximately as r^{-2} it is observed to vary with epoch, azimuth, and photon energy (Acton, 1995). E.g., higher energy photons scatter more. All YLA level-2 and level-3 data products have employed *sxt_decon.pro* for scatter correction.

David McKenzie evaluated the scattering fraction by analysis of 35 over-the-limb flares throughout the mission, and analysis of spikey arcade from 18-dec-98. His result for the scattering fraction of each SXT analysis filter is
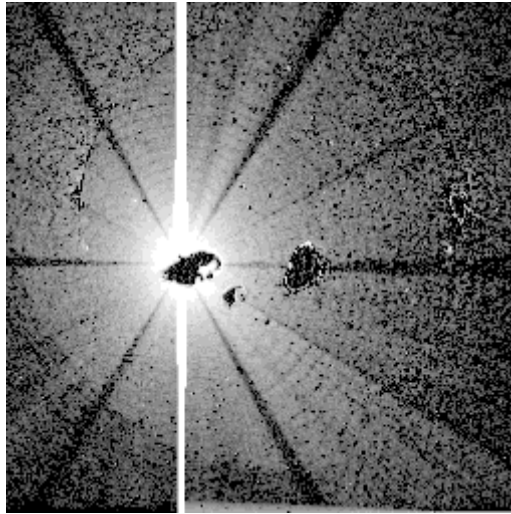
Figure 10. AlMg "starburst" image (scaled to the poser 0.3 to reveal faint parts) showing scattered x-rays from the C6.7 flare at 14 October 1995 06:58:02 with the pre-flare image of 06:53:22 subtracted. The radial dark spokes are shadows of the entrance filter frames. The faint arc in the lower left is a vignetting effect. The thin semi-circumferential arcs are shadows of the filter support mesh.

Al.1	0.035
AlMg	0.035
Mg	0.05 (estimated)
Al12	0.20
Be	0.20

These values are set as the default scattering fractions in *sxt_psf.com* which is called by *sxt_decon.pro*, the program used to correct, as best we know how, for scattering wings. The default scattering slope is r^{-2}.

3.2. X-ray Vignetting

The design of grazing-incidence x-ray telescopes makes them more subject to off-axis vignetting than traditional optical telescopes. Fuller, Lemen, and Acton (1994) present the SXT off-axis calibration measurements and derive the vignetting function used in the correction program *sxt_off_axis.pro*. The chosen vignette function is based on both laboratory and flight observations and is modelled as two non-concentric cones. This vignette correction has been applied to all YLA level-2 and level-3 data products.

Shin and Sakurai (2013) numerically simulated SXT vignetting and concluded that the adopted SXT vignetting function is better described by a model taking into account that fact that the optical and geometric axes of the telescope are offset. The differences between the two corrections do not appear to be large but are probably real. Unfortunately, an improved correction algorithm has not been published so the YLA products currently employ the Fuller, *et al.* function.

3.3. Entrance Filter Failures

By far the most troublesome calibration problems for the SXT have been estimation of the change in spectral sensitivity related to entrance filter failures and correction for the stray visible light which entered the telescope. During the mission the routine stray-light-monitor signals tracked stray light levels within the instrument and provided immediate notice of new failures. Having no means to determine the fraction of filter(s) which had failed we initially assumed that an entire 30° sector had failed at each stray light step. With the detailed analyses presented in section 8, and the availability of the entire SXT data set to study, it has proven possible to improve the estimate of the increase in spectral sensitivity for each failure epoch. Conclusions of which sectors failed at each stray light step is presented in Table 8. Analysis of entrance filter open area, used for SXT sensitivity computation, is summarized in section 8.8.

Techniques for removing stray visible light from the x-ray images are discussed in section 9.

3.4. Analysis Filters

The only SXT analysis filter known to have changed properties was the thin aluminum filter. The changes comprised the opening of three or more pinholes. Fortunately, none of these pinholes were in the filter area where the solar x-ray image fell for normal pointing so they had an insignificant impact on x-ray sensitivity. However, the stray visible light diffracting through the pinholes and that passing directly through the filter material (at approximately the 10^{-6} level) contaminated the x-ray image at a level comparable to the quiet x-ray coronal signal. This contamination is partially corrected through the use of terminator images (see section 9) but remains a problem for quiet sun analysis. Fortunately, the signal levels of active regions and flares are sufficiently great that stray light contamination is of minor importance. Fortunately, for browsing, the quiet sun the AlMg images, which are the least affectedby stray light, are nearly the same in appearance as the Al.1 images.

3.5. X-ray Mirror

The on-orbit contamination of SXT aspect sensor optics (section 7) and the CCD (section 10) suggests the possibility of contamination of the x-ray mirror. Such contamination would have impacted x-ray reflectivity and scatter. We have not seen evidence of changes in x-ray scatter in the data, although subtle changes could easily have escaped notice. The mission-long comparison of SXT and GOES signals in Figure 11, while only approximate because of the significantly different band passes of the two instruments, shows no indication of a drastic change in SXT x-ray sensitivity.

3.6. CCD Contamination

Contamination of the CCD to a level that could be detected in thin-filter x-ray images was observed after a few months of operation in the form of small dashes
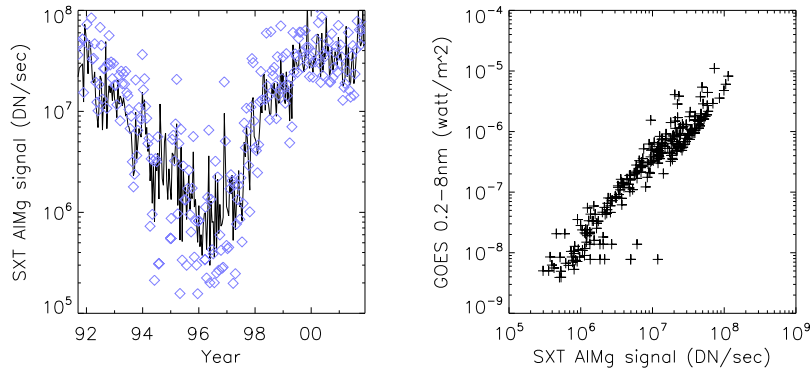
Figure 11. Comparison of concurrent bi-weekly samples of 0.2-8 nm GOES flux and the total signal in SXT AlMg composite images. Blue diamonds in LH panel are GOES signals multiplied by 4×10^{13}. For very quiet conditions the GOES data may bottom-out, accounting for some of the outlying points in the right hand figure.

of decreased signal aligned with the CCD gate structure (along the CCD rows). The contamination artefacts disappeared when the CCD temperature was raised to about 0°C. In 1992 the CCD was permitted to warm up to 0°C three times and baked out to +24°C once. Beginning in January 1993 regular bakeouts of the CCD were implemented. The dates of all CCD warmups and bakeouts are provided in the Yohkoh Legacy Archive and section 10.3. The need for and frequency of bakeouts decreased with time as *Yohkoh* outgassed. We have no evidence of residual contamination on the CCD following bakeouts.

3.7. CCD Camera Gain

The pre-launch CCD camera gain was set to approximately 100 electrons DN^{-1} to best match the saturation levels of the analog-to-digital-converter and the CCD full-well capacity and 100 electrons DN^{-1} was used as default thereafter. In-flight measurements of camera gain were challenging for a number of reasons but indicated a gain of about 90 electrons DN^{-1}. SXT analysis software was updated (but not until 2014!) to reflect this change. Derivation of emission measures from SXT data accomplished prior to 2014 may therefore be low by 10 percent because of this error. See section 10 for further discussion of CCD properties and camera gain.

3.8. Ionization Damage to the CCD

While damage to the CCD response from ionizing x-ray radiation was quickly evident in aspect sensor images we have discovered no evidence that it reached a level that affected x-ray sensitivity. It was observed that severe x-ray overexposure caused an increase in dark current (section 10.2.2) signal which disappeared over periods of a few days. If appropriate dark frames weren't acquired in and around these transient events the corrected image in overexposed areas could be

either too high or too low. In general, SXT data in the YLA have been screened to eliminate cases of severe ill correction.

3.9. Energetic Particle Damage to the CCD

Si lattice dislocations of CCD pixels cause electron traps and loss of charge transfer efficiency, which is equivalent to a loss of x-ray sensitivity. This happens on a pixel by pixel basis and, in some cases, appeared to anneal out over time. Evidence of such damage are so-called dark spikes, i.e., pixels of high dark current. Stable dark spikes are removed from the x-ray images by subtraction of dark frames which also include the dark spikes. Gburek and Sylwester (2002) describe and illustrate the dark spike issue. The number of dark spikes increased steadily through the life of *Yohkoh* as illustrated in Figure 12.
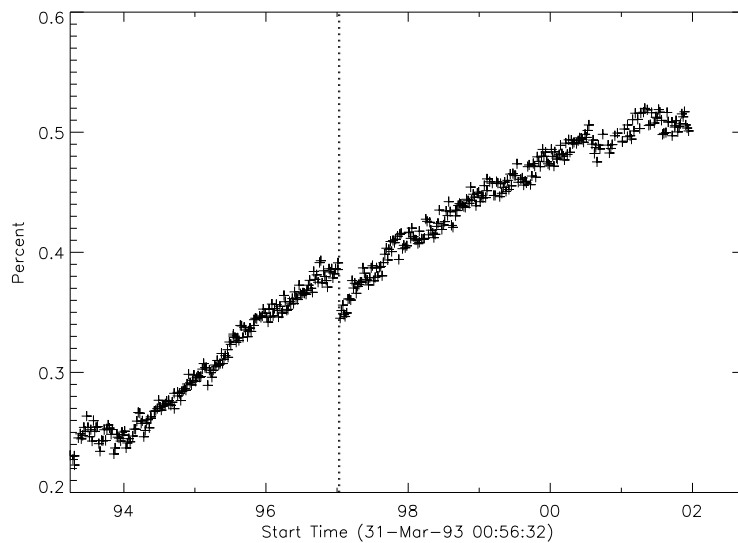

Figure 12. Percentage of FR pixels having a dark signal more than five standard deviations above the average dark signal. Vertical dotted line denotes the six day CCD bakeout of January 1997. It seems that the resulting drop in the trend of dark spike increase was only temporary.

3.10. Errors and Uncertainties

Pre-launch calibration of the effective area of the SXT (Lemen, 1993) aimed to attain an absolute accuracy of a few percent or better. The uncertainty introduced by decompression of downlinked data are returned by *sxt_prep.pro*. An estimate of the uncertainty introduced by counting statistics is returned by the program *sxt_dn_uncert.pro*. The uncertainty in CCD camera amplifier gain (section 10.1) enters directly in the conversion of instrument units into emission measure and could be as large as ten percent. Deconvolution of scattered x-rays (section 3.1) by *sxt_decon.pro* and correction for telescope vignetting (section 3.2)

by *sxt_off_axis.pro* are certainly not perfect but are difficult to quantify. Errors associated with stray light correction and dark signal subtraction (Acton, 1997) have not been quantified. These unquantified errors may be substantial for faint coronal sources, e.g., coronal holes, but it is certain that the corrected images are closer to the truth than if the corrections are not applied. Systematic errors from, e.g., mirror or filter contamination are possible but unknown. All of the SXT data products in the YLA have been adjusted for all known and quantified instrumental effects, as appropriate.

4. SXT Operational Anomalies

The SXT achieved design performance, returning excellent soft x-ray images for the duration of the mission. Unfortunately, the instrument experienced technical anomalies that complicated data reduction and analysis. It is the purpose of this document to describe and explain these issues and to detail the corrective measures that have enabled fruitful solar studies throughout the *Yohkoh* mission. The SXT data are unique in spectral response, observing epoch, and the solar conditions recorded.

In brief, the SXT on-orbit anomalies included:

(a) Attitude errors requiring, when possible, manual corrections to the *Yohkoh* attitude (ATT) data base (Section 6).

(b) A steep decrease in the signal level through the optical aspect sensor beginning immediately after launch (Section 7).

(c) A series of failures of entrance filters during the mission which introduced visible stray light into the telescope, compromising x-ray images and altering the spectral response of the SXT (Sections 8 and 9).

(d) Pinholes and optical transmission through the thin aluminum x-ray analysis filter affected the x-ray image (Section 9).

(e) Time-dependent x-ray radiation damage to the CCD which impacted sensitivity to visible light and, to much a lesser degree, x-ray sensitivity (Section 10).

(f) Energetic charged particle damage to the CCD causing dark spikes and changes in dark signal (Section 10).

(g) Condensation of some contaminant on the CCD requiring periodic bakeouts to remove it (Section 10.3).

(h) Telemetry drop outs causing gaps in SXT images.

The SXT_Observation_Notes section of the YLA (http://solar.physics.montana.edu/ylegacy/observ_notes.html) provides extensive analysis and illustration of these and other data anomalies. This paper will document the steps that have been taken to create the best and most accurate data products from SXT. Subsequent sections include illustrations and descriptions of the anomalies, how each affected the SXT images, and corrections applied when creating the higher-level data products.
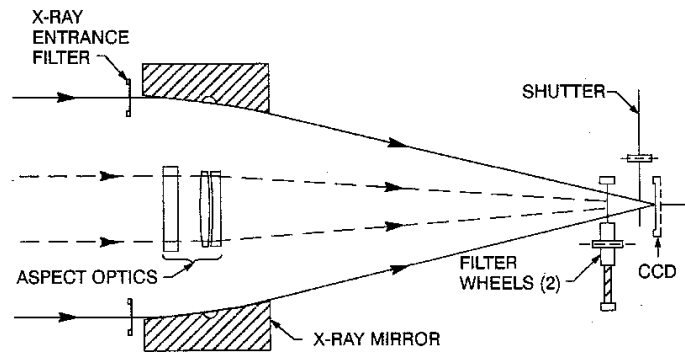
Figure 13. Schematic diagram of key elements of the SXT.

5. The SXT Optical Train

The Soft X-ray Telescope on *Yohkoh* comprises a 2-element grazing incidence mirror feeding a CCD detector in the focal plane (Tsuneta *et al.*, 1991). The entrance aperture, defined by the projected area of the first element of the mirror, is an annulus 0.362 mm wide and 230.65 mm in diameter (Acton, 1999). A confocal optical telescope (called the aspect sensor) is nested within the x-ray mirror. Dual filter wheels with both x-ray and optical filters and a rotating shutter complete the instrument. Extensive technical details of the SXT, including many engineering drawings, are presented in the Solar-A Experiment Interface Control Agreement (EICA, 1990).

Figure 14 illustrates the front end of the SXT with the individual 30° sectors numbered clockwise from 1 to 12. In the sections that follow we will refer to this Figure in detailing the sequence of entrance filter failures throughout the operational life of SXT.

Dual entrance filters were employed on the SXT to guard against pinholes in the opaque metallic coating permitting light to enter the telescope. The coatings were made as thin as possible in order to provide the greatest feasible x-ray transmission. Thus, even apart from pinholes, a single filter is not completely opaque, transmitting of the order of 10^{-7} to 10^{-6} in the visible.

The individual filters are mounted on frames each of which covers a 60° sector of the entrance annulus. Each frame comprises two individual 30° sections as shown in Figure 15. The filter membrane is lexan 180 nm thick covered with 70 nm of Ti and 90 nm of Al with the Al being the outer coating. As may be seen in Figure 16 the outer filter is positioned so that the Al coating faces the sun while the inner filter has the lexan in the solar direction. This mounting scheme permitted purchasing only a single type of filter assembly but it exposed the lexan of the inner filter to the sun and space following the failure of an outer filter.
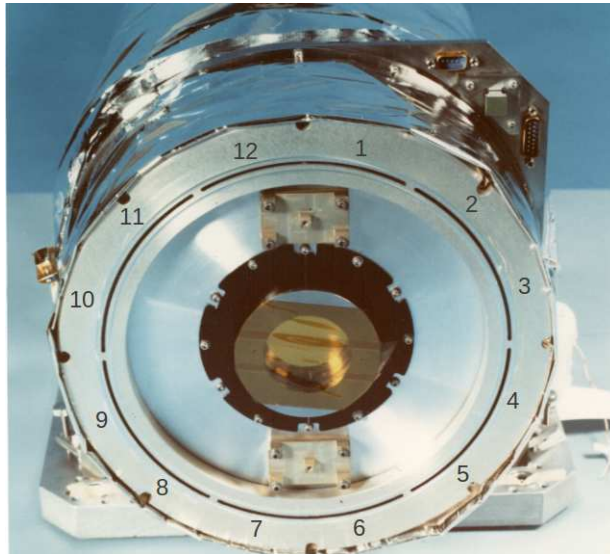
Figure 14. SXT entrance annulus with filter sectors numbered.

Figure 15. SXT entrance filter frame. The filter membrane itself has been destroyed in testing, showing the catastrophic degradation typical of the failure of thin films of this type.
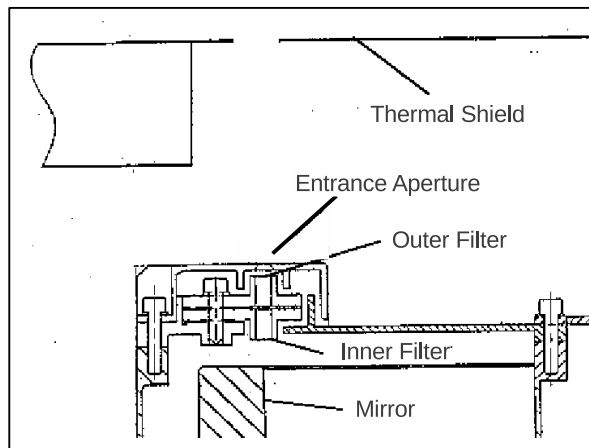

Figure 16. Positioning of SXT entrance filters.

6. *Yohkoh* Pointing

The *Yohkoh* attitude control system (ACS) was designed to point at sun-center with stability of order one arcsec s^{-1} and several arcsec min^{-1} (Ogawara *et al.*, 1991). The spacecraft (S/C) included two sun sensors, a star tracker and geomagnetic sensors for attitude determination. For on-orbit alignment determination the SXT included a small white-light telescope referred to as the aspect sensor (Tsuneta *et al.*, 1991). The HXT aspect system (HXA) employed linear CCDs, operating in the visible as limb sensors, to provide pointing information in X and Y to one or two arcsec accuracy (Kosugi *et al.*, 1991). The *Yohkoh* attitude (ATT) data are derived from HXA signals. Between HXA measurements the X and Y ATT data are computed by interpolation of S/C gyro data which is transmitted at a higher rate.

The *Yohkoh* ACS normally maintained solar north upwards on the SXT CCD. I.e., the solar rotation axis should parallel the CCD pixel columns. Roll was determined from S/C gyro data with reference to the Canopus star tracker. When Canopus was occulted roll was determined from the gyros alone. Inflight calibration based on SXT visible-light aspect images and analysis of Mercury transit observations (Wuelser *et al.*, 1998) revealed an offset in roll, i.e., SXT CCD columns are rotated 0.7 degrees clockwise from S/C coordinates on the SXT images. The roll angle given in ATT records is the S/C roll angle. The Yohkoh/SXT/SolarSoft program *get_roll.pro*, and all other SXT data processing programs, correct for the 0.7 degree offset so that the SXT processed images in the YLA all have solar north straight up.

Preparation of the *Yohkoh* ATT data base is carried out as part of creation of level-0 data products from the downlinked telemetry. One ATT record is created for each and every SXT image. The records contain the coordinates of sun-center in full resolution pixel (FR) units (2.455 *arcsec pixel*$^{-1}$) of the SXT charge coupled device (CCD) detector. The ATT file format is detailed in appendix A.

The ATT values incorporate a number of adjustments based upon inflight calibration (Wuelser *et al.*, 1998). ATT information is incorporated in the header of SXT FITS-format images available through the YLA. For *Yohkoh* mission-specific (XDA) format data the ATT files are separate files.

6.1. *Yohkoh* Attitude Errors

There are several sources of error in the ATT data.

1. Imperfect illumination of the HXA for certain pointings.

2. Ageing of the HXA.

3. Failure of one of the S/C gyros.

4. Increase in gyro drift rate with age.

5. Loss of fine pointing, i.e., pointing not under control of the fine sun sensors.

6. HXA samples weren't taken frequently enough at medium telemetry rate to provide anchors for gyro signal interpolation at the end of orbits near sunset. This problem became evident late in the mission when gyro drift was high.

7. Loss of the SXT aspect telescope on 13 November 1992 due to failure of an entrance filter. After this time it was no longer possible to acquire aspect sensor images.

8. Corrupted or missing TLM downlink data.

Pointing anomalies tended to occur at times of loss of fine pointing in connection with non-standard operation such as partial solar eclipses. As *Yohkoh* aged the frequency of poor ATT data increased.

From time to time the ATT data base has had corrections applied as pointing maladies were identified and improved calibration became available. As of the time of this writing the ATT data base is in version 23 (ATT_23). The version in use at the termination of *Yohkoh* scientific operation on 14 December 2001 was ATT_08. Full frame images (FFI) are more amenable to ATT correction than partial frame images (PFI) because the entire solar limb is available for adjustment of the ATT records by limb fitting. The corrected values are not, in general, as accurate as the good ATT values derived from telemetry but are considerably better than the original, uncorrected, values. Figure 17 illustrates ATT errors identified and corrected in the ATT_23 data base.

6.1.1. ATT Roll Errors

Because S/C roll changed smoothly and fairly slowly roll corrections for a given interval have been applied by interpolation or extrapolation to every affected roll record. Thus, roll corrections have been applied when appropriate to both SXT partial frame (PFI) and full frame (FFI) records. In contrast, yaw-pitch (X-Y) errors change quickly so corrections are only possible for full frame images where limb fitting is possible.

The large roll corrections in 1998 reflected *Yohkoh* entering safe-hold mode following the partial eclipse of 22 August 1998. Until late 2000 most roll corrections resulted from corrupted or missing telemetry. In these cases the roll value was set to the first valid roll datum following the corrupted records. The accuracy of these extrapolations are generally better than 0.1 degrees. Roughly 2.1 percent of SXT ATT records have been adjusted for roll.
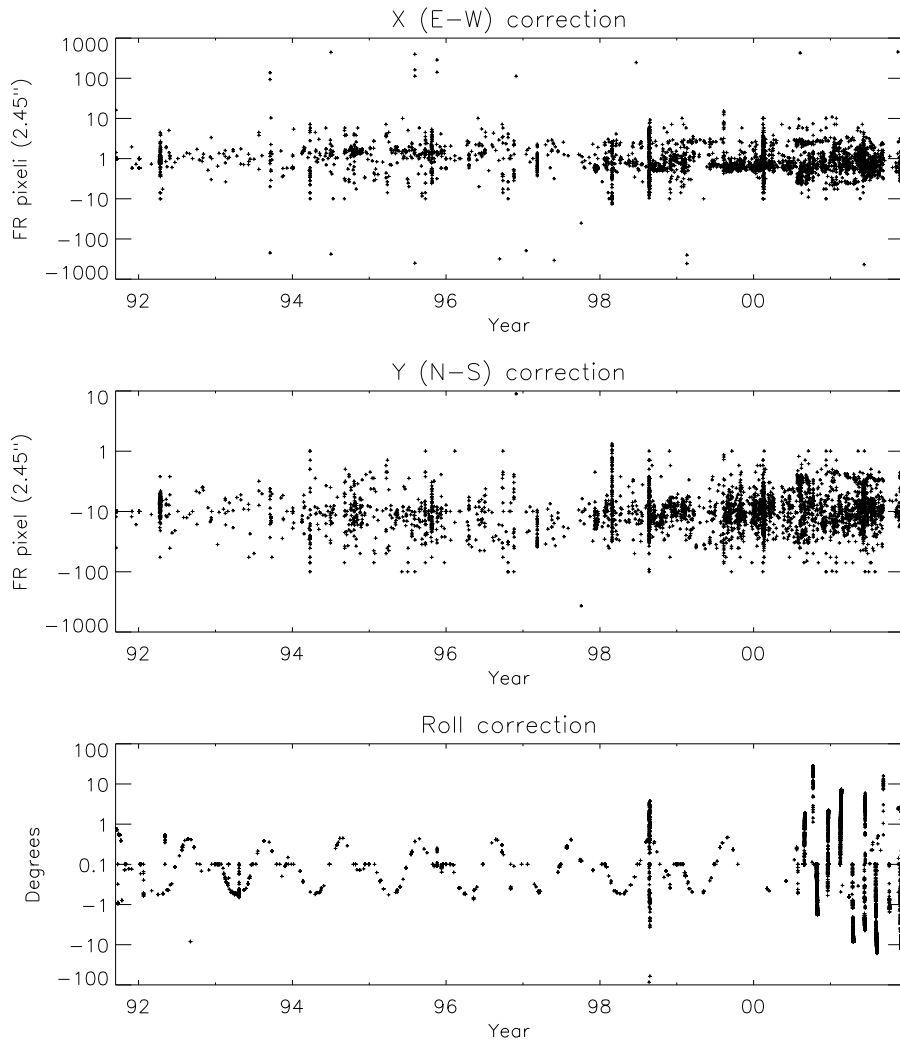
Figure 17. Corrections applied to the *Yohkoh* attitude data base.

6.1.2. ATT X-Y Errors

The SXT requires precision attitude information for every image in order to co-align x-ray images for time-lapse review and for registration of images with other sources of solar imagery, e.g., magnetograms, H-alpha pictures, etc.

It has proven possible to quantify ATT-XY errors for SXT full frame images (FFI) because the solar limb is always recorded. Our procedure for searching for pointing problems is as follows. First, composite (level-2) images are prepared by combining short and long exposures to eliminate areas of detector saturation as much as possible. These composite images are formed from either two or three exposures depending on the duration of the longest exposure.
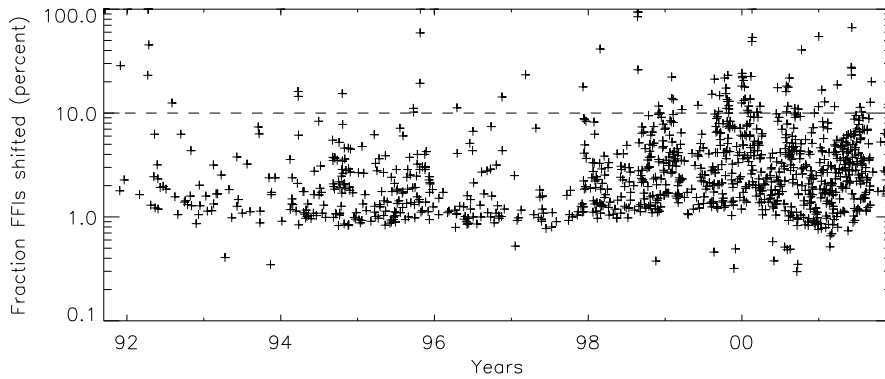
Figure 18. The percentage of FFIs requiring ATT-XY adjustment for each day of the *Yohkoh* mission for which ATT adjustment was applied.

The next step is to clean artefacts from the composite images, logarithmically compress the signals, and rebin the quarter resolution (9.82 *arcsec pixel^{-1}*) images to half resolution (4.91 *arcsec pixel^{-1}*). These processed images are co-aligned based on the best ATT data available, collected into image cubes, and run as movies at different frame rates. In movie mode shifts of 5–10 arcsec are readily discernible. If active regions are seen to shift position on the disk from frame to frame, but the limb doesn't move simultaneously, this indicates that the ATT data for the short exposure(s) of the composite image are in error.

Images with incorrect ATT values are flagged for further processing. The necessary X-Y corrections to ATT are derived by fitting a circle (of the proper diameter for the epoch) to the full-disk x-ray image and comparing the circle center to the sun center position recorded in the ATT record. The ATT corrections thus derived have been incorporated into the ATT data base. Figure 17 illustrates the ATT adjustments. About 1.5 percent of FFIs (4562 in X and 4568 in Y of 298,288 images) have had their ATT data thus adjusted. This has been an iterative process as small errors show up better after large image shifts are corrected. Small (< 10 *arcsec*) ATT errors undoubtedly still remain. However, the mission-long movie available through the YLA now runs quite smoothly, even through times of solar eclipse.

6.2. ATT Reliability

The accuracy of *Yohkoh* ATT data has been checked by limb-fitting SXT aspect sensor images acquired prior to November 1992. Due to the 4.91 *arcsec* pixelization of the images it is not feasible to obtain a fitting accuracy better than about 2.5 *arcsec* although it appears that the best ATTs are good to one *arcsec*.

During the 3746 days of *Yohkoh* scientific operation there were 3699 days producing data with ATT records. Of these 3699 days there were 1120 days, slightly less than one-third, which required ATT-XY correction. Recall that ATT correction in X and Y is only feasible for full frame images (FFI) and has only

Table 2. Dates with Questionable ATT

13-Sep-91	14-Sep-91	15-Sep-91	18-Sep-91
19-Sep-91	20-Sep-91	01-Dec-91	04-Jan-92
09-Apr-92	10-Apr-92	11-Apr-92	12-Apr-92
13-Apr-92	14-Apr-92	02-Aug-92	01-Jan-94
24-Mar-94	25-Mar-94	20-Oct-94	23-Sep-95
24-Sep-95	24-Oct-95	25-Oct-95	26-Oct-95
31-Dec-95	17-Apr-96	17-Nov-96	09-Mar-97
07-Dec-97	26-Mar-98	22-Aug-98	23-Aug-98
25-Aug-98	26-Aug-98	01-Dec-98	01-Feb-99
02-Feb-99	09-Feb-99	22-Mar-99	06-Jun-99
11-Aug-99	23-Aug-99	12-Sep-99	17-Sep-99
10-Oct-99	16-Oct-99	17-Oct-99	19-Oct-99
22-Oct-99	24-Oct-99	26-Oct-99	29-Oct-99
31-Oct-99	01-Nov-99	30-Dec-99	31-Dec-99
01-Jan-00	02-Jan-00	03-Jan-00	09-Jan-00
10-Jan-00	13-Jan-00	16-Jan-00	26-Jan-00
31-Jan-00	01-Feb-00	09-Feb-00	13-Feb-00
17-Feb-00	18-Feb-00	19-Feb-00	12-Mar-00
14-Mar-00	27-Mar-00	18-Jun-00	28-Jul-00
30-Jul-00	31-Jul-00	06-Aug-00	07-Aug-00
13-Aug-00	08-Sep-00	24-Sep-00	10-Oct-00
30-Dec-00	31-Dec-00	14-Jan-01	28-Jan-01
16-Mar-01	29-Mar-01	03-Jun-01	04-Jun-01
05-Jun-01	06-Jun-01	15-Jul-01	22-Jul-01
02-Sep-01	07-Sep-01	25-Nov-01	26-Nov-01
14-Dec-01			

been done for those FFIs of adequate quality to be incorporated into level-2 composite images. In most cases these ATT corrections were needed for one or a few FFIs on any given day. For such days nearly all of other ATT values (i.e., ATT for the PFIs also) will be correct and the images can be co-aligned, etc., with confidence.

For days with more than, say, 10 percent of the FFIs requiring ATT correction in X and/or Y extra caution should be exercised in the use of SXT pointing (ATT) data. Figure 18 illustrates, for every day of the *Yohkoh* mission for which an ATT adjustment was required (1120 days), the fraction of composite FFI's requiring ATT-XY adjustment. There are 101 of 3699 days for which more than ten percent of composite FFIs required ATT-XY shifts. These dates are listed in Table 8 and justify extra care for co-registration of partial frame images (PFI).

7. SXT Aspect Sensor

The SXT aspect sensor comprises an objective group followed by the aspect sensor door, four filters in the forward filter wheel and the CCD detector in the
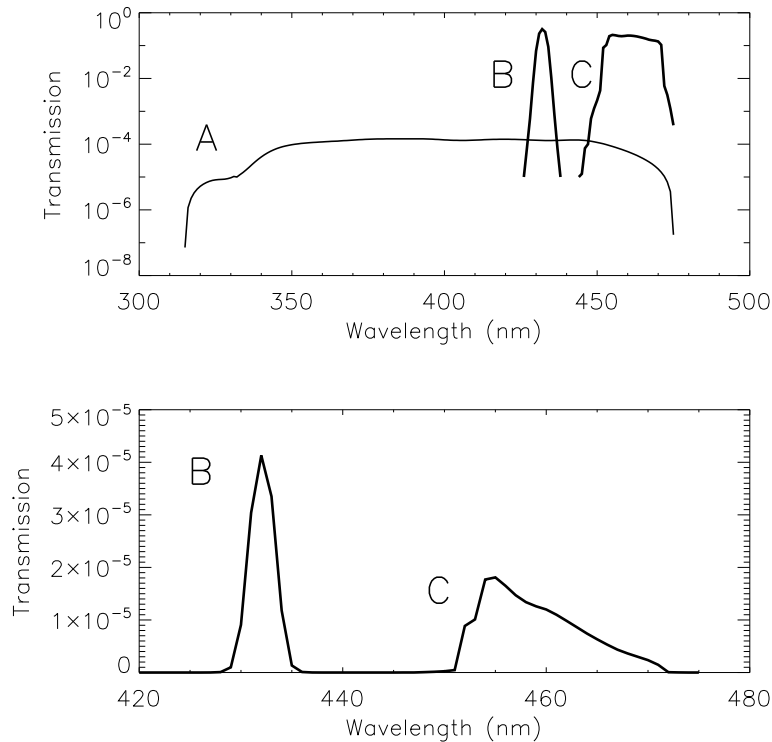
Figure 19. Transmission of aspect sensor optics. (A) lens assembly, (B) narrow-band filter, and (C) wide-band filter. Top panel: individual elements. Bottom panel: combined transmission.

focal plane (Tsuneta *et al.*, 1991). The objective group included an entrance window with a white light attenuator coating, a bandpass filter, and a doublet lens. Technical details of the aspect sensor telescope are given by Grillot and Cruz (1990). The material properties of these optical elements are given in Table 3. All components were made of certified radiation resistant materials except for the Hoya CM-500. This glass was tested in a proton beam to 1000 times the expected three year dose at the anticipated *Yohkoh* orbit. All optical elements were anti-reflection coated.

The forward filter wheel of the SXT included four filters for use with the aspect sensor telescope. Their description is given in Table 4. The wide-band (WB) and narrow-band (NB) filters are equipped with 2.5 mm of Schott UG-5 absorbing glass on the rear side to reduce, to acceptable levels, ghosts from light reflected off of the surface of the CCD. Figure 19 presents the transmission and passbands of the optical assemblies of the SXT aspect sensor telescope.

The relative alignment of the X-ray and optical images is discussed in SXT Calibration Note 36 (**?**). The values given there were initially determined by T. Metcalf in 1992. The final calibration, given in the YLA and incorporated in all SolarSoft analysis software for SXT, was determined by L. Acton in 2008 using

Table 3. Aspect Objective Group Components

1.	Synthetic fused silica plus 50 nm Al.
2.	Hoya CM-500 blue glass with far visible-near IR coating.
3.	Bi-convex Schott BK7-G18 (cerium stabilized) lens.
4.	Concave-convex LF5-G15 lens.

Table 4. Aspect Sensor Filters

1.	Wide band (WB), 18.5 nm FWHM centered at 460 nm.
2.	Opal glass diffuser.
3.	Quartz defocusing lens for UV flood of CCD.
4.	Narrow band (NB), 3 nm FWHM centered at 431 nm.

all available optical images. The absolute and relative offsets are given by the program *gt_sxt_axis.pro*. I.e., the WB image falls 0.25 ± 0.23 full resolution pixels east and 1.08 ± 0.25 pixels north of the x-ray axis. The NB image falls 0.90 ± 0.23 arcsec east and 1.36 ± 0.27 arcsec north of the x-ray axis.

7.1. Aspect Signal Decline

It became immediately obvious that the intensity of the optical images was decreasing approximately exponentially as illustrated in Figure 20.

7.1.1. Spectral Dependence of Aspect Image Signal Decay

Figure 20 shows that the NB and WB channels did not decay at exactly the same rate. This difference is better illustrated by the intensity ratio plot in Figure 21.

Figure 21 shows that the obscuring material was initially more absorbing at 431 nm than it was at 460 nm. As the layer became thicker the ratio stabilized around 5.0. For the first three CCD warmups the ratio increased (NB signal increased proportionally more) while for the fourth warmup the ratio decreased. This puzzling observation will be further discussed in the following two subsections.

7.1.2. Effect of CCD Warmup

Figure 22 summarizes the response of the NB channel for the four CCD warmups in 1992. Note that for these warmups the increase in NB signal intensity continued for the duration of the warmup, as if an absorbing layer continued to evaporate throughout the interval. It does not appear that further increase in the bakeout temperature had much effect on the rate of evaporation as illustrated in panel B of Figure 22.

The decrease in NB intensity at the fourth CCD warmup revealed in panel D of Figure 22 is very puzzling. As shown in Figure 23 the WB images show
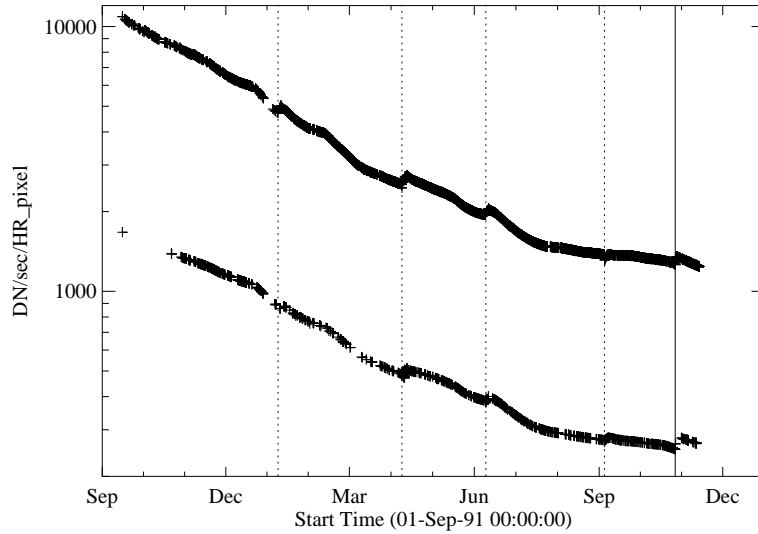
Figure 20. Total intensity in aspect sensor image. The upper curve is from the narrow band filter and lower curve from the wide band filter. Vertical dotted lines denote times of CCD bakeout. The vertical solid line indicates the time of the first failure (27 October 1992) of outer entrance sectors 6 and 7 (see Figure 14 where sectors are numbered) when a slight increase in optical signal appears. The termination of the curves falls on 13 November 1992 when the first inner entrance filter failed and the SXT was flooded with visible light.
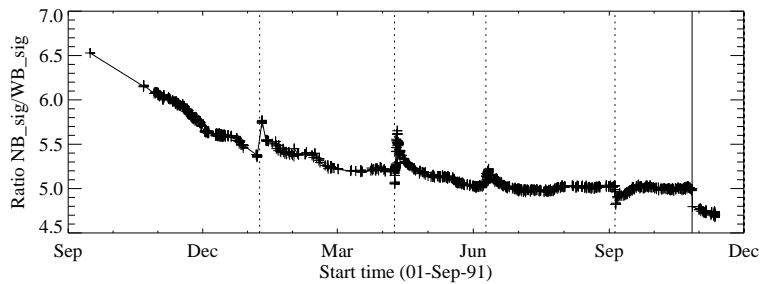

Figure 21. Ratio of NB to WB signal. Times of CCD warmup are indicated by dotted lines and 27 October 1992 entrance filter failure by the solid line.

a quite different light curve. The effects observed here cannot, except perhaps for the first images after the beginning of CCD bakeout, be blamed on dark signal correction. Appropriate warm-CCD dark frames were used in preparation of these data. It is possible that interference effects in a thin layer of contaminant is involved as noted by Narukage *et al.* (2011) for the XRT instrument on *Hinode*.

Another feature seen in some of the aspect sensor light curves is a brief drop in signal at the very beginning of CCD warmup. This can be seen in the WB plot of Figure 23. The most probable cause is that the CCD warms up slower than the CCD camera temperature indicator so that, for early images, the software
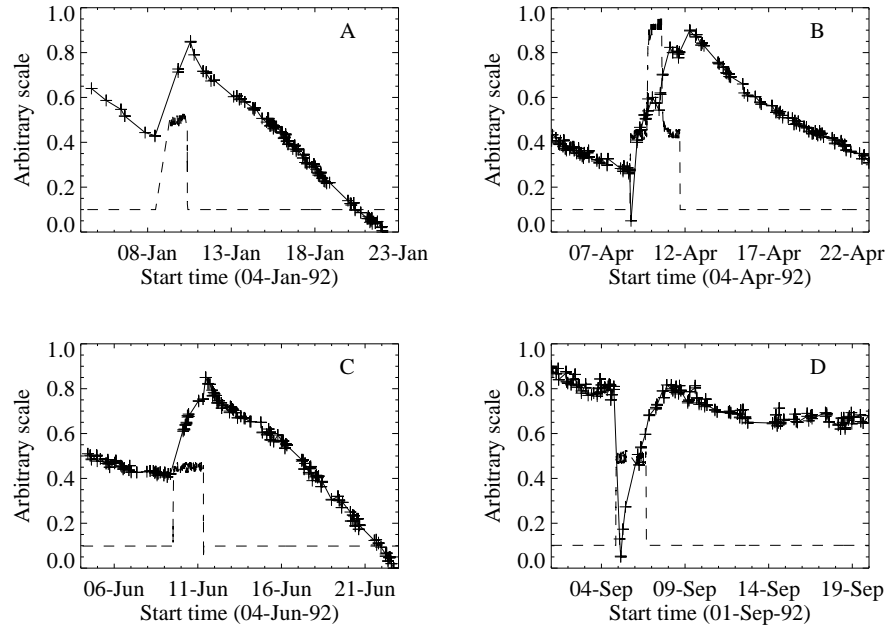
Figure 22. NB signal (+) and CCD temperature (broken line) for the four CCD warmups of 1992. Note that panel B illustrates a warmup (0°C), bakeout (20°C), and warmup (0°C) experiment.

chooses dark frames, taken later in time, that are too warm, thus over–correcting the exposures. Due to the higher dark current and less accurate dark-correction bakeout images are, in general, less accurate photometrically.

7.1.3. Uniformity of Signal Change Over the CCD.

If the decrease in visible-light signal is uniform all over the CCD this would indicate that the cause is in front of the focussing optics. I.e., probably an absorbing layer on the front of the aspect sensor entrance window. As demonstrated in Figures 24 and 25 this is indeed the case.

When illuminated by the out-of-focus solar image coming from the aspect sensor optics the opal glass diffuser provides an approximately uniform illumination of the CCD. This provides a ready means for identifying possible areas of non-uniformity of optical response.

The results of such a comparison of SXT diffuser images, chosen to be near identical *Yohkoh* pointing, is illustrated in Figure 24. There is a notable decrease in optical response in areas (active region belt and the limbs) that were heavily irradiated by soft x-rays. However, the ratio image on the right shows very little departure from uniformity outside of the white area. In the areas indicated in black the average late/early signal ratio is 0.380 ± 0.004. The decrease in CCD sensitivity in radiation-damaged areas is another issue that is discussed in section 10.
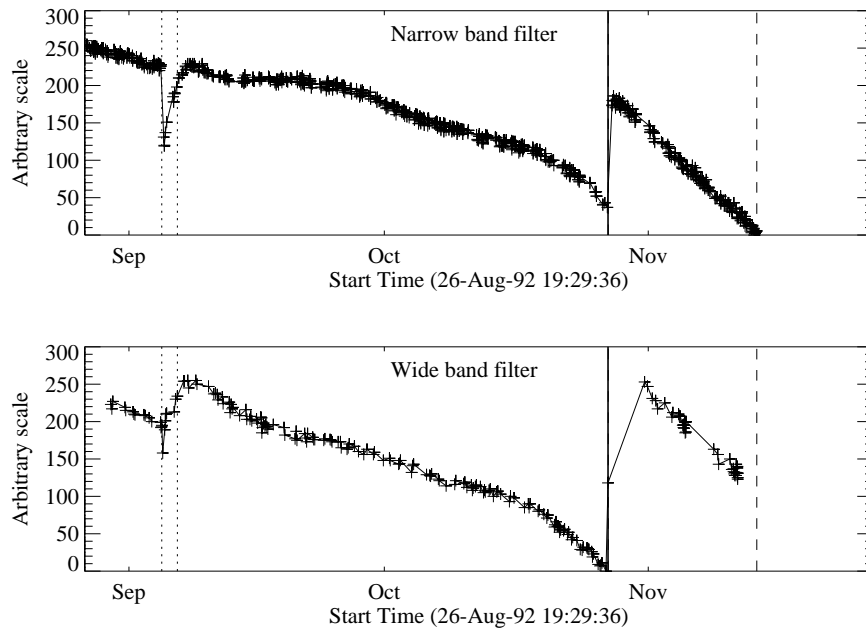
Figure 23. Detail of fourth CCD warmup. Dotted lines; CCD bakeout interval. Solid line: outer entrance filter failure. Dashed line: inner entrance filter failure.

Figure 24. SXT diffuser images. Increased radiation-damaged area is evident in the center (later) image. In the rightmost panel the black portion shows the area of the CCD in which the signal decrease id very uniform, falling between 61.4 and 62.5 percent.

In order to check for uniformity of response decrease within the solar image the mean intensity in 10° sectors between 0.8 and 1.05 $R_\odot$ at the north, west, south, and east points of the disk have been compared. The signals from the four points around the limb decrease in lock step again demonstrating that the absorbing agent is uniform over the field of vies.

In order to determine if scattering of the optical image changed during the mission we compared the signal in an annulus surrounding the narrow-band image with the disk-center signal. Figure 25 shows the areas selected for comparison and the result of the analysis for the first year of the mission.
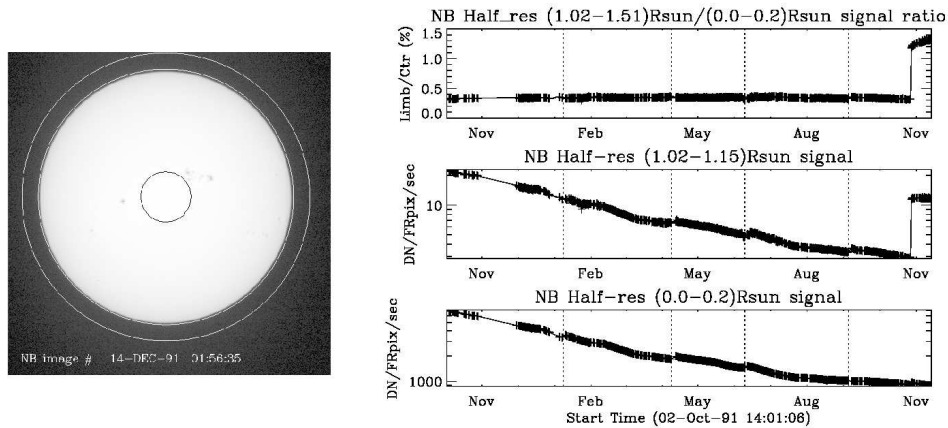
Figure 25. Left panel: Illustration of 2 sample regions. Right panel: Top, scatter to disk center ratio; center, disk center light curve; bottom, scatter light curve.

It is clear from this Figure that, except for minor variations, the scattering of sunlight into the near-sun annulus is constant up until 27 October 1992 when the first entrance filter failure occurred. The increasing ratio following this event is caused by the fact that the disk-center signal, which passed through the aspect sensor optics, continued to decline whereas the annular signal, which entered through the leak in the entrance filter, remained stable. The stability of the above-limb/disk-center ratio for more than a year establishes that whatever caused the response decrease of the aspect sensor signal did not increase the visible-light scatter of the aspect telescope.

All indications from these image uniformity analyses demonstrate that absorbing material must have been deposited on optical elements in front of the focussing lenses or uniformly over the face of the CCD. It seems likely that any hydrocarbon based absorbing layer on the CCD thick enough to reduce the aspect sensor signals by nearly a factor of 8.8 (an optical thickness of 2.2 at 430 nm) would have decreased the soft x-ray signal more than can be inferred from the x-ray data. Thus, some change in the transmission of the aspect sensor lens assembly is to blame for majority of the signal decrease with CCD contamination playing a secondary role.

7.2. Aspect Sensor Performance Summary

The aspect sensor light curves displayed in Figure 20 are not perfectly smooth, even apart from discontinuities at the times of CCD bakeout. A comparison with season (solar diameter), the temperature of the SXT forward support plate (which holds the SXT objective group including the aspect sensor optics), and epochs of heightened energetic particle fluxes from the Van Allen radiation belts revealed no obvious correlation with the loss of aspect sensor sensitivity.

Signals through all optical filters showed a similar decline and loss of signal. I.e., between 15 September 1991 and 13 November 1992 the NB and diffuser

signals decreased by factors of 8.8 and 9.1 respectively. Between 15 September 1991 and 27 October 1992 the WB signal decreased by a factor of 6.6. The decay curve was essentially the same for all optical images: narrow band, wide band, diffuser, or quartz CCD-flood lens. The decay of signal was uniform over the entire CCD. The CCD showed no effects (e.g., from radiation damage) correlating with the decline. The optical elements were all selected for radiation insensitivity so radiation-induced color centers in the optics are unlikely to contribute to the decrease in transmission. All of these facts lead to the conclusion that the optical signal decay was caused by the accumulation of some absorptive or reflective contaminant, reaching an effective optical thickness of about 2.2 by November 1992, on or within the aspect objective lens assembly. It is true that a small fraction of the decrease is caused by ionizing-radiation damage to the CCD in localized areas but this effect accounts for only about 1 percent of the total decrease in optical signal.

The small increases in optical signal at times of some CCD bakeout (Figure 20) probably indicate the removal of a thin layer of absorbing contaminant from the face of the CCD.

We have not been able to determine what material could have deposited on or within the aspect sensor optics with such a large optical thickness. The thermal shield mounted to the space craft in front of the SXT (Figure 16) and the inside of the aspect sensor optical assembly itself were painted with black Chemglaze Z306, applied and baked according to NASA specifications. After more than 2 decades the mystery remains.

8. Entrance Filter Failures and Visible Stray Light

The most serious instrumental anomalies during SXT in-flight operation were periodic failures of the entrance filters in front of the x-ray mirrors. The associated flood of white light into the telescope contaminated x-ray images and precluded collection of any aspect telescope images. Fortunately, it proved possible in large measure to subtract this stray light signal from the x-ray data. Because of the importance of these effects to the scientific return of the SXT the following sections will present a technical description of the stray light effects and their remediation.

As noted in section 5 visible light was excluded from the x-ray telescope by dual metal-coated thin plastic filters in front of the x-ray mirror. These filters began to catastrophically fail beginning 27 October 1992 05:59, about 13 months after launch. The adjacent outer entrance filter segment failed 79 minutes later. With the exception of the very first failure, most of the failures were first detected at orbit sunrise. For this reason we believe that thermal stresses at sunrise ultimately caused the filters to break due to accumulated degradation of the Lexan plastic. For the single case in 1992, when we were able unambiguously to discriminate between failures of outer and inner filters, an inner filter failed shortly (17 days) after the outer filters. For the outer filters the Lexan was protected by the Al and Ti coatings. After the outer filters failed the Lexan plastic of the inner filters was directly exposed to degradation by solar

Table 5. Impacts of SXT Entrance Filter Failures

1.	Light of all wavelengths enters the telescope.
2.	The SXT optical aspect telescope becomes unusable.
3.	The x-ray sensitivity of the instrument increases.
4.	The x-ray spectral response of the instrument is changed.
5.	Solar ultraviolet (UV) light becomes available for CCD photon flood.

UV and atomic oxygen (see e.g., Dever *et al.* (2012)). Typically, as evidenced by Figures 26 and 27, when the filters failed the entire 30° sectors opened. This is consistent with experience with pre-launch testing of these filters. In the 27 October 1992 cases both failed sectors were mounted on a common frame.

The resulting visible stray light affected all subsequent x-ray exposures to some degree and has multiple important impacts on SXT performance as listed in Table 5. The remainder of this section details our diagnosis of stray light effects and steps taken to correct the x-ray data for stray light contamination.

The SXT aspect telescope is a highly filtered bandpass telescope so the direct entry of unattenuated white light into the SXT completely overwhelmed the optical aspect image. The SXT x-ray sensitivity and spectral response are determined in part by the x-ray transmission properties of the entrance filters so each removal from the optical path increases somewhat the x-ray sensitivity of the telescope, particularly at the longer wavelengths. These changes in x-ray response are not evident to the unaided eye in the images and, to the extent that we understand the chronology of failures, the SXT analysis software takes account of the shifts in spectral response.

The fifth effect listed in Table 5 is arguably a benefit. Flooding the CCD with UV light helps to anneal soft x-ray damage to the device (Acton *et al.*, 1991). The fact that the SXT detector survived in usable condition for over a decade may be due, at least in part, to the UV flood routinely carried out at the start of every daylight pass.

8.1. First Entrance Filter Failure

As a result of failures of the thin-film entrance filters stray visible light began to enter the telescope on 27 October 1992. On 13 November 1992 the second layer of one of the the duplex entrance filters failed and the full solar spectrum entered the instrument by reflection off of the x-ray mirror . Aspect sensor images could no longer be acquired, even the shortest exposure were totally saturated.

8.1.1. Visible Signal Change

In late October 1992 SXT observers noted a faint increase in background intensity in solar images taken through the SXT aspect sensor. Marilyn Bruner, designer of the SXT telescope, first suggested that this might be caused by the failure of an entrance filter. As Figure 26 illustrates, the stray light pattern is what would be expected by the failures of one, and soon thereafter a second,
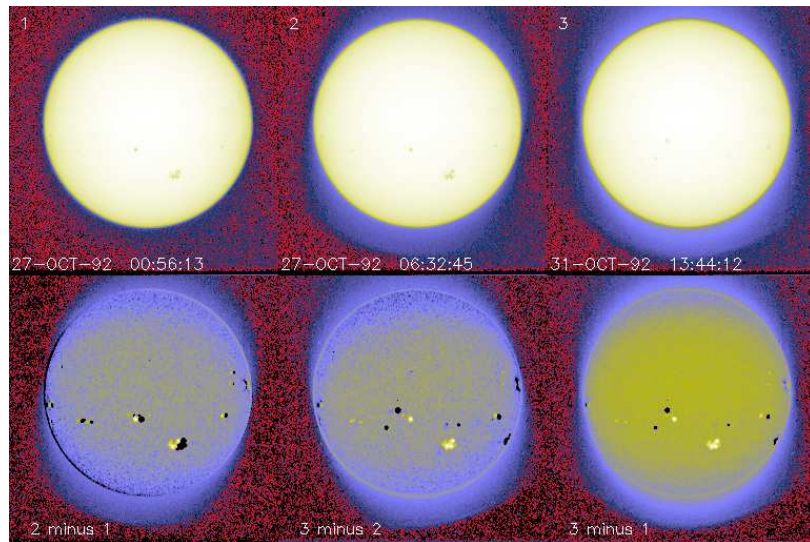
Figure 26. SXT wide-band aspect sensor images. The top three panels are images acquired (1) before the 27 October 1992 failures, (2) after the first failure, and (3) after the second failure. The poor on-disk contrast of these three images is caused by the logarithmic scaling. The bottom three panels are difference images detailing the effects of each failure.

$30°$ filter sector. The fact that the stray light increase is so modest attests to the fact that the inner filters were still intact. Pre-launch testing revealed that a single entrance filter transmits about 10^{-6} in the visible.

The sequence and location of these first entrance filter failures is demonstrated in Figure 26. Visible light focussed off of the x-ray mirror is severely diffracted in the radial direction (0.362 mm aperture) but much less in the circumferential direction where the effective aperture is much wider (~ 53mm, slightly curved). Thus, the rightmost difference image, poorly focussed at 1 and 7 o'clock and well focused at 4 and 10 o'clock, shows that either sector 1 or 7 (see Figure 14 for sector numbers) had opened up. The middle difference image shows that the adjacent sector 6 or 12 subsequently also failed.

Failure of SXT entrance filters increases the instrument sensitivity at long x-ray wavelengths because of the removal of absorbing material in the optical path. However, the interpretation of the stray-light-monitor variations (section 8.3) in terms of changes in x-ray sensitivity is tricky because of the duplex entrance filter design of the SXT. The opening up of a filter sector in a single entrance filter layer will increase x-ray sensitivity. However, except for this early case, both layers must open to register the change in stray light. Thus, after the first inner filter failure of 13 November 1992 the enhanced stray light signal from further outer filter failures was overwhelmed by the signal from sectors already having double-filter failures.

8.1.2. X-ray Signal Change

X-ray scattering from surface micro-roughness of a grazing incidence x-ray optic is predominantly in the axial direction, i.e., perpendicular to the mirror surface
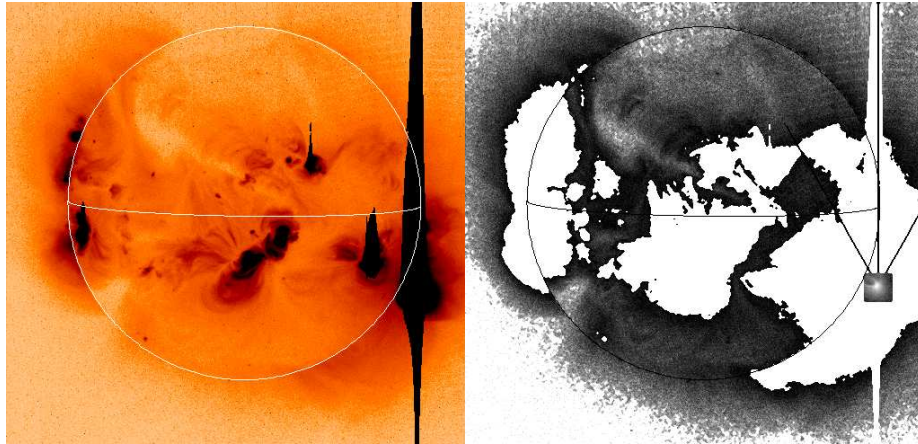
Figure 27. SXT 5.3 second AlMg exposure (2 November 1992 13:24:42) showing enhanced x-ray scatter in a 60° sector directed northwards. Solar limb and equator drawn in for clarity. Left image is a reversed red color table, black areas show CCD saturation and charge bleed. Right image has been scaled to emphasize the striped scattered x-ray pattern northwards on the image in two 30° sectors, indicated by solid lines. A nearly simultaneous partial frame image has been inserted to show the position of the bright x-ray kernel well above the limb.

(Aschenbach, 1985). The x-ray scattering wings of the SXT point spread function appear in exposures of intense solar flares – in this case a useful diagnostic of entrance filter failures. When an entrance filter sector fails the x-ray signal incident on the mirror through that sector increases. Thus, the scattered x-rays in the image direction opposite to that sector are enhanced relative to other directions. This happened on one well-observed occasion between 27 October 1992 and 13 November 1992 and is illustrated in Figure 27. This AlMg image was taken late in a GOES class X10 flare when the intensity had diminished to a C9 level.

The 180° ambiguity of which sectors failed on 27 October is removed by this flare image. Figure 27 shows scattered x-ray pattern to be enhanced in two sectors on both sides of the upward vertical (north). The faint arcs in the scatter area are the shadows of the AlMg filter support mesh. The inset is a helf second Be-filter partial frame image obtained 1 minute after the full frame image. It is interesting that at this late epoch in this great flare the soft x-ray emission is concentrated in a small kernel at the top of a single high loop, like the diamond on a ring. The direction and width of the scatter demonstrates conclusively that the outer entrance filters of sectors 6 and 7, both sections of the filter frame nearest to the instrument baseplate, were the failed sectors.

Because of the spectral dependence of entrance-filter transmission the coolest coronal regions (lower energy photons) should show the greatest signal increase. Figure 28 illustrates quiet regions in the north and south chosen for examination for changes in x-ray signal levels associated with the 27 October 1992 failures.

Only composite full sun images outside the South Atlantic anomaly (SAA) were used in the analysis so that approximate correction for scattered x-rays could be made with the SolarSoft program *sxt_decon.pro*. As this was a period
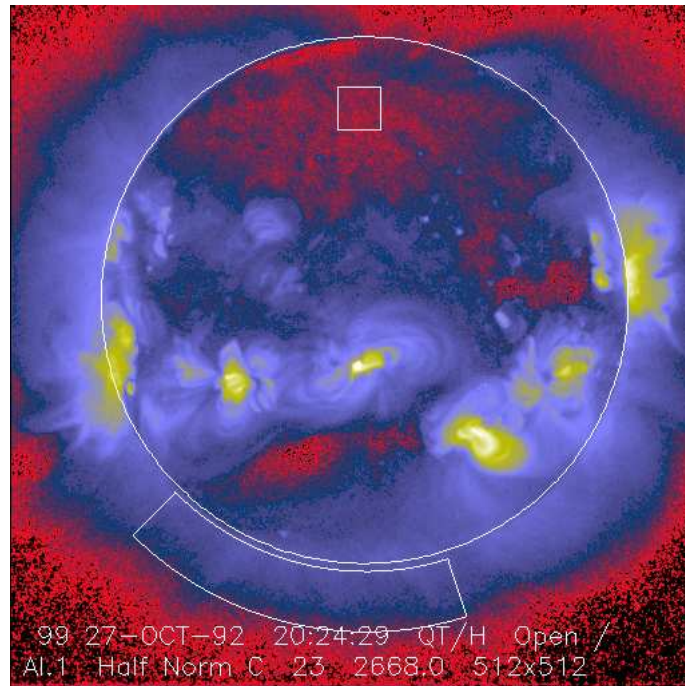
Figure 28. South polar and northern high-latitude areas sampled for filter-failure analysis.

of moderately high x-ray flare activity care was taken to assure that there was no correlation between GOES flux and the SXT signal in the selected area to avoid as much as possible signal enhancements associated with transient x-ray emission. Signals in these regions were sufficiently intense to minimize error in correction for x-ray scatter and also avoid the newly asymmetric scatter to the north shown in Figure 27.

The signal level changes for the two thinnest SXT analysis filters are shown in Figures 29 and 30. The horizontal broken lines display the average signal levels before and after the entrance filter rupture. The center broken line in each upper graph is the average of the upper and lower signal levels. For the bright south polar region it falls precisely through the group of images acquired after the first and before the second rupture events, as would be expected. The data from the northern high latitude region is not as definitive, probably due to weaker signals and more dominant contamination from transient x-rays.

The crosses present data from all available images. The diamonds are the images for which the exposures were taken more than 2 minutes after sunrise and before sunset, for which *Yohkoh* was not in the SAA, and for which the GOES low-channel (1-8 Å) signal falls between $(1.0 - 1.7 \times 10^{-6} \ watt \ m^{-2} \ sec^{-1})$. For the relatively bright south pole region the Al.1 signal increased by a factor of 1.22 and the AlMg signal by 1.16. For the faint high latitude region in the north a more severe constraint on GOES signal of $(0.8 - 1.3 \times 10^{-6} \ watt \ m^{-2} \ sec^{-1})$ is used in the image selection criterion. For the north region the Al.1 signal increased by a factor of 1.46 and the AlMg by 1.30.
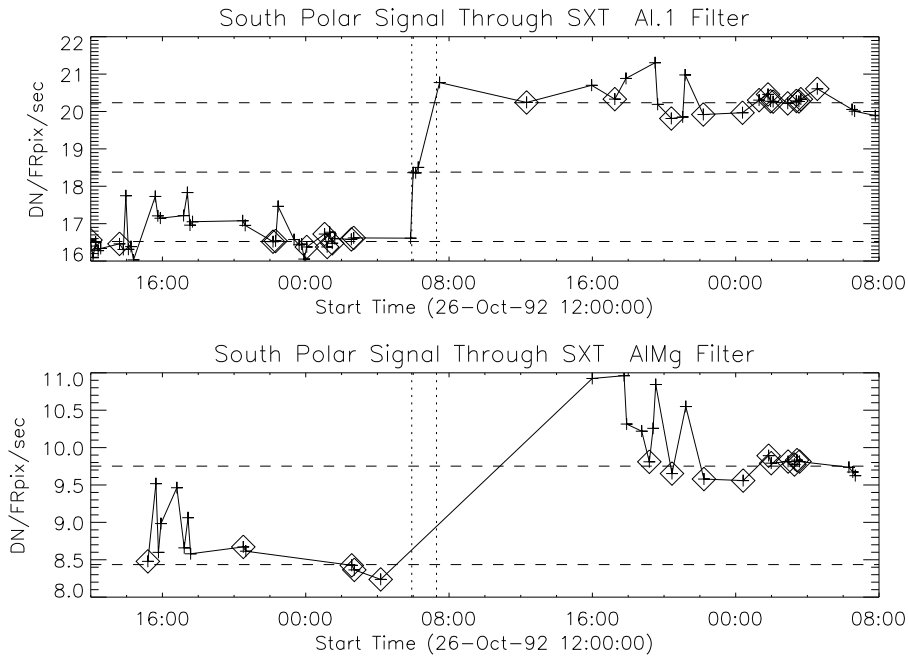
Figure 29. Increase in SXT signal level through the two thin analysis filters for the south pole region of Figure 28. Dotted lines indicate the approximate times of the ruptures. Diamonds identify the data used in computing the expected signal increase.

To test our interpretation of the impact of the 27 October filter failures we used standard SXT analysis software to compute the fractional SXT signal increase versus coronal temperature. The results of this computation are displayed in Figure 31 along with derived results from Figures 29 and 30. A positive result would have the dotted (dashed) lines crossing on or near the solid curve in each panel. For the south pole region (dotted lines) the analysis results are consistent with the result expected for the opening of two 30° outer-entrance-filter sectors.

The comparable results for the weaker-signal north pole coronal hole region (dashed lines) are in poor agreement with the calculations. The observed signal increases larger than expected from the analytical model. This effect may be caused by poorer counting statistics (resulting from both weaker signal and much smaller area sampled) and/or a relatively greater x-ray contamination from transient x-ray activity.

The conclusion from this analysis is that the change in sensitivity and temperature response of SXT following the 27 October 1992 entrance filter failures is consistent with expectations for the total opening of two (numbers 6 and 7) outer entrance filters.

8.2. Stray Light Paths to the CCD

We are able to follow SXT stray light evolution in three ways: the stray-light-monitor, diffuser images, and terminator images.
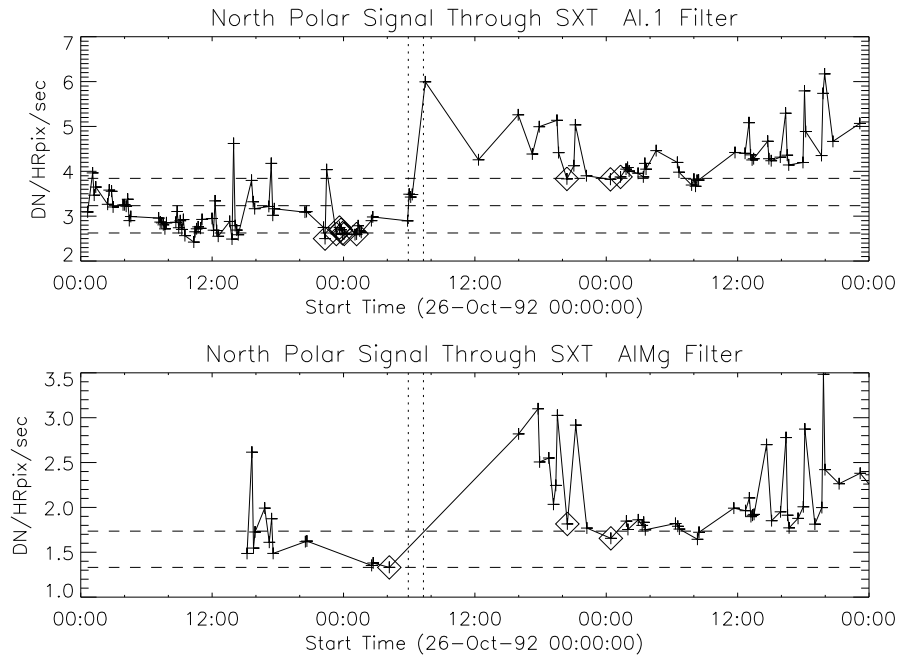
Figure 30. Increase in SXT signal level through the two thin analysis filters for the north pole region of Figure 28. Dotted lines indicate the approximate times of the ruptures. Diamonds identify the data used in computing the expected signal increase.

SXT stray-light-monitor images are obtained with the shutter closed, the AlMg analysis filter in place in filter wheel B, and filter wheel A in the open position. Diffuser images have the opal glass diffuser in place in filter wheel A and filter wheel B in the open position. Terminator images are obtained between 24 and 12 seconds before ephemeris sunset, a period when the light path is opaque to soft x-rays but transparent to visible light. Any one of the x-ray analysis filters in filter B may be used for terminator images. Filter wheel A is always in the open position for terminator images.

The stray light path to the CCD is totally different for the normal x-ray images and the shutter-closed stray-light-monitor images. For the case of the x-ray images the visible image from the x-ray mirror falls upon the x-ray analysis filter in filter wheel B. Depending upon the nature of the filter surface a certain fraction of this bright light is scattered or reflected forward through the open-filter hole in filter wheel A and illuminates the inside of the forward filter wheel aperture plate around its entrance hole or travels further forward into the body of the telescope.

The CCD can see scattered light from this forward filter wheel aperture plate through the triangular weight-relief cutouts on each side of all filter mounting positions in filter wheels B and A. This is where the light comes from that produces the characteristic patterns along the east and west sides of the CCD image for open-shutter x-ray exposures (see Figure 43).
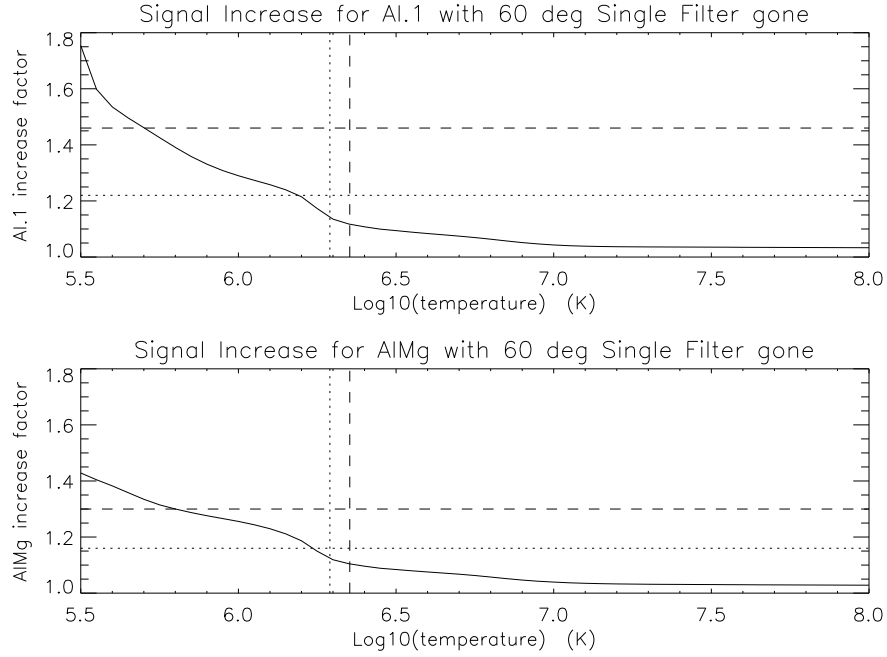
Figure 31. The solid curves delineate the predicted signal increase versus coronal temperature resulting from a 60° entrance-filter rupture (i.e., two filter sectors) for the SXT thin analysis filters. The horizontal lines shows the observed changes and the vertical lines the derived pre-failure filter-ratio temperatures. The dotted lines show the results for the above-limb south polar region and the dashed lines for the northern coronal hole region. (Sampled regions are indicated in Figure 28.)

Table 6. SXT Analysis Filters

Filter	Component	Description
Al.1	Al(126.5 nm)+Si(1.3 nm)+	
	Al$_2$O$_3$(0.3 nm)+SS mesh(0.84%)	shiny, transmits $\approx 10^{-6}$, pinholes
AlMg	Al/Mg/Mn composite	shiny, reflects more than scatters
Be	119 μm Be	diffuse scatterer
Al12	11.6 μm Al	shiny, reflects more than scatters
Mg3	2.52 μm Mg	uneven surface, scatters

This interpretation can explain not only the pattern but the variation in stray light level for the different analysis filters. Figure 43 shows a great variation of stray light intensity from filter to filter, but with nearly the same basic structure (except for the special case of Al.1). The intensity differences can be traced to the reflective and diffuse-scatter properties of the filters as described in Table 6.

Note that, except for Be, the filters are not precisely flat so the detailed scattering/reflecting properties will be unique for each part. These conclusions are consistent with inspection of flight-spare filters and how the filters were

installed in filter wheel B. Small variations in the stray light pattern reflect differences in *Yohkoh* pointing and/or seasonal changes of the angular diameter of the solar disk.

For the case of shutter-closed stray-light-monitor exposures the light path to the CCD is completely different. In this case the poorly focussed visible light image from the x-ray mirror first passes through either the narrow-band (NB) or wide-band (WB) optical filters (passbands shown in 20 and on to the closed shutter blade. The shutter being closed, the CCD cannot see the filter wheel cutouts and the forward aperture plate as is the case for shutter-open exposures. The aperture between the shutter blade and the CCD is a 24.8 mm square with 3.2 mm radius rounded corners. The CCD sensitive area is an 18.43 mm square centered within this aperture.

The shutter-closed stray light path into the CCD volume is apparently a result of the fact that the shutter does not not quite cover the square aperture described above. Careful checking of drawings against an actual spare shutter shows about 1.7 mm overlap on top center and essentially 0.0 mm at the top corners. However, the bottom corners of the aperture plate are not quite covered in either shutter-closed position, leaving a gap about 1 mm^2 in area. As shown in Figure 34 there are two stray-light-monitor states, separated by about a factor of two in intensity, depending on whether the wide gap in the rotating shutter is on one side or the other of the CCD aperture. The high states are associated with shutter-encoder position 26 and low states with encoder position 30. These two positions are 90° apart, centered on the open position.

The illumination is, within about 2%, the same across the CCD for both shutter positions. In the high state the signal goes from 2.1 to 1.8 times the low state value from the bottom to the top of the CCD image. Figures 32 and 26 reveal that the illumination of the CCD by the light leak is strongly concentrated towards the bottom (serial register side) of the CCD. This may account for the fact that there is no sign of the radiation-damaged, low visible-light sensitivity, features in the image – even though they are quite prominent in the diffuser images. Note that the stray light distribution across the CCD is fairly flat but concentrated towards the center. This seems to contradict the interpretation that the light enters the extreme corners of the CCD aperture plate.

8.3. Stray Light Monitor

Beginning early December 1992 a routine stray-light-monitor image was added to the standard full frame image (FFI) observing table. These were quarter resolution (QR) shutter-closed exposures using the shortest exposure (0.96 ms, DPE=2) with filter A in position 2 (NB) and filter B in position 1 (open). In 1999, after the three entrance failures early in the year, the standard stray-light-monitor exposure was approaching saturation so we began to take stray-light-monitor exposures using filter A position 5 (WB). Both NB and WB exposures were taken for about a year for cross calibration. The conversion is NB=3.8*WB for dark-frame corrected images. NB images ceased to be routinely taken on 4 April 2000.

A sample stray-light-monitor image is shown in Figure 32 left hand image. The right hand image has been corrected for dwell time per row during CCD
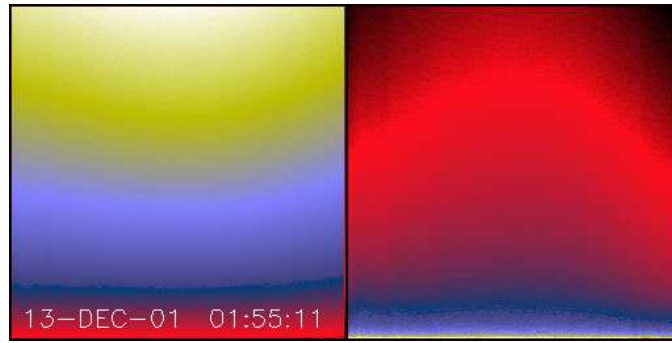
Figure 32. Left: WB stray-light-monitor image (high state). Right: Same image corrected line-by-line for exposure time. This should approximate the actual distribution of stray light on the CCD (detailed in Figure 33).
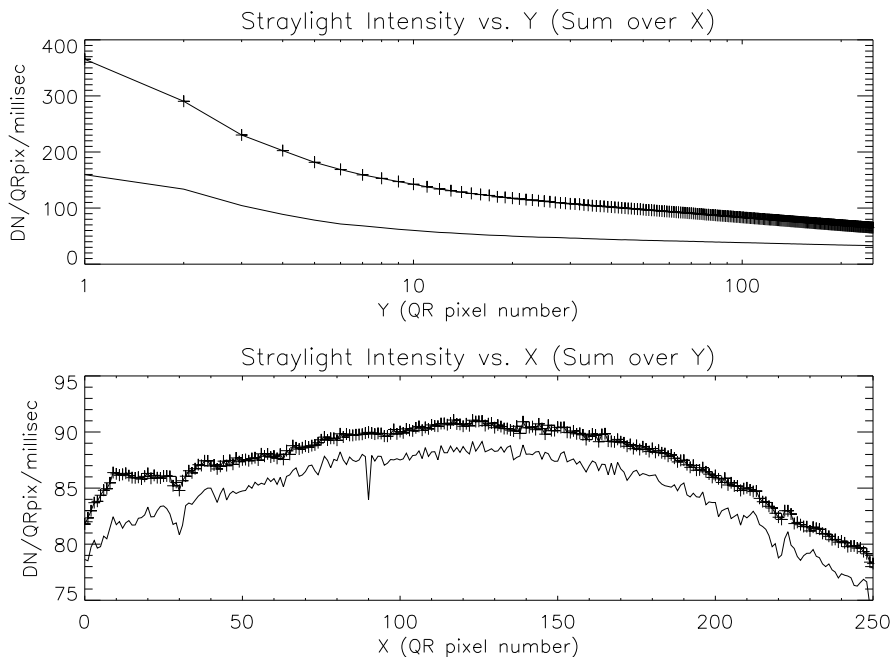

Figure 33. Upper: Stray light CCD illumination in the column (Y) direction. Lower: Illumination in the row (X) direction. High state (crosses): 13-DEC-01 01:55. Low state (solid curve): 13-DEC-01 08:38. In the lower panel the low-state curve has been multiplied by 2.1 for plotting convenience.

read out. Note that the stray light is concentrated towards the bottom edge of the CCD.

Figure 33 illustrates, from one dimensional sums over WB stray light images in both the low and high state, the distribution of illumination on the CCD in a more quantitative fashion. Note that there is very little difference between the two states other than intensity.
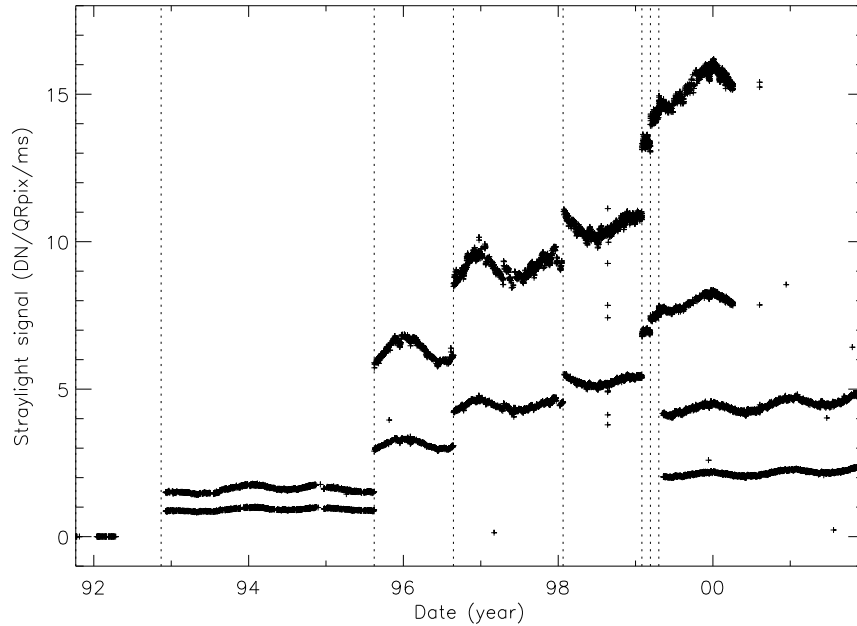
Figure 34. Signal rates from stray-light-monitor exposures. Unless otherwise noted the vertical dotted lines in this and following figures denote times of known entrance filter ruptures (Table 8). The two parallel curves correspond to the two possible "shutter closed" positions, called high-state and low-state in the text. The low pair of curves beginning April 1999 use the less transmissive wide-band (WB) filter in filter wheel A.

Figure 34 displays the total dark-corrected stray light signal from 11,885 stray-light-monitor images. To some degree the stray light levels are affected by *Yohkoh* pointing and seasonal solar diameter. The data points shown for 1992 were from exposures equivalent to the stray light monitors that were obtained as dark frame candidates. They average to zero, i.e., there was no visible stray light reaching the CCD prior to the entrance filter failures.

The stray-light-monitor exposures are taken with the shutter closed, an optical filter in place in the filter A position, and filter B in the open position. While a good way to monitor the total stray light entering the instrument the configuration is quite different from that of the x-ray exposures, terminator leak images or diffuser images. For x-ray images filter A is normally in the open position, an x-ray analysis filter in filter B, and the shutter is open. Figure 35 illustrates the total signal in centrally-pointed Al.1 terminator FFIs (terminator images are described in 8.5). Comparison to Figure 34 shows that, near the end of January 1999, there is a proportionally much larger step in the Al.1 stray light signal than in the stray-light-monitor signal. This is caused by a near-simultaneous entrance filter failure and the opening of a new pinhole in the Al.1 analysis filter.
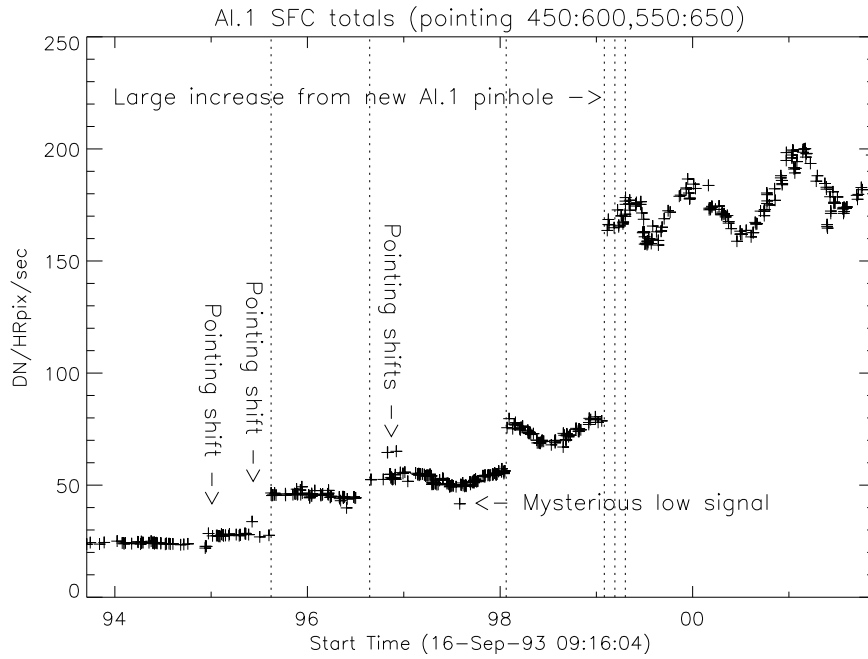
Figure 35. Summed signal in Al.1 terminator (SFC) images. Signal levels are sensitive to *Yohkoh* pointing.

8.4. The SXT Diffuser

An opal glass diffuser was installed in the forward filter wheel of the SXT for use in generating CCD flat-field images on a routine basis. However, the diffuser images were by no means "flat" and also recorded visible light artefacts not present in the x-ray images (see e.g. Figure 24). Thus the diffuser images were of limited use for their original purpose.

Contrary to the stray-light-monitor images discussed in section 8.3, for which the path of stray light to the CCD involved scattering and leakage past the shutter, the diffuser images are normal, shutter controlled, exposures – even after the entrance filters failed and the bulk of the light came off the x-ray mirror rather than through the aspect sensor. This makes the diffuser images better quantitative indicators of stray light levels onto the SXT focal plane than the stray-light-monitor. Furthermore, unlike the wide and narrow band optical images, the diffuser images were not saturated, making them useful monitors of stray light levels within the instrument.

Figure 36 illustrates the evolution of the diffuser images with time. Up until the November 1992 entrance filter failure the major artefacts were the loss of optical sensitivity in the strongly x-ray irradiated areas. This impact is quantitatively illustrated in Figure 37. Here, the broken line denotes the CCD row chosen for the 2 intensity curves. The black curve is from this image. The upper (white) profile from the diffuser image of 15 September 1991 17:55, before any radiation damage had accumulated, has been normalised to the 26 August 1992
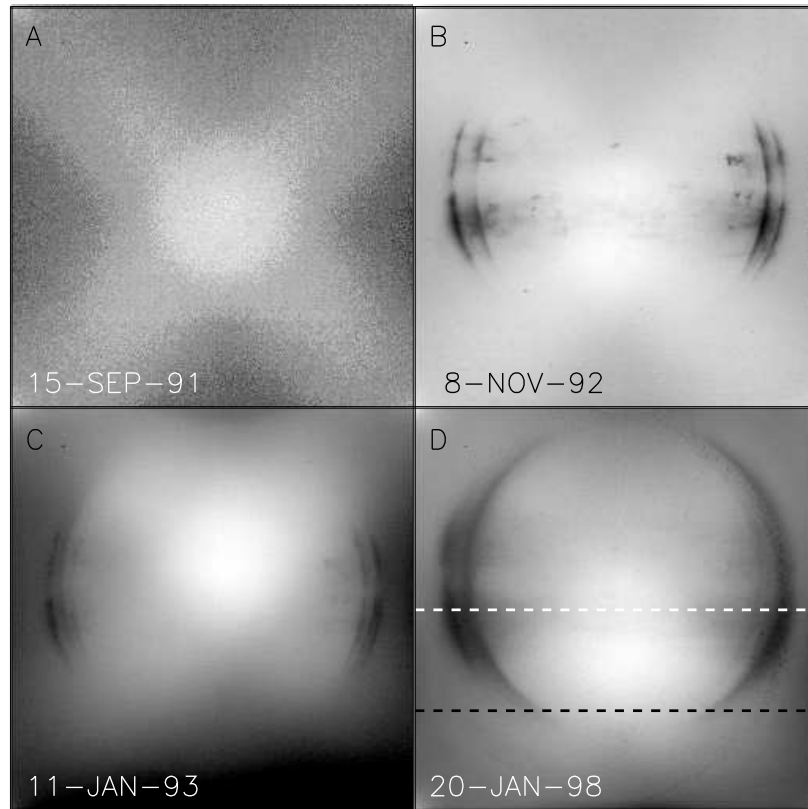
Figure 36. Examples of diffuser images throughout the mission, individually scaled to reveal details. A: First diffuser image. Noisy because of 8 bit compression. B: Shortly before 13 November 1992 entrance filter failure. Damage from x-ray exposure is evident. C: About 2 months after filter failure. About eight percent of x-ray entrance ring is open. D: Five years after C. About two-thirds of x-ray entrance ring is open by this time. The image section between the broken black and white lines denotes the area used for producing the mission-long light curves of Figures 38 and 39.

profile at the left and right wings of the image. At the column indicated by the broken vertical bar, through the deepest part of the damaged area, the sensitivity to light coming through the SXT aspect sensor optics is decreased by 20 percent. This is in rough quantitative agreement with image B of Figure 36 which was obtained a bit over 2 months later. For comparison, the burned-in areas of panels C and D are about 3 and 4 percent respectively. The reason for this relative improvement in optical sensitivity possibly has to do with the change in shortwave cutoff of the every-orbit UV flood from about 340 nm to 170 nm and an intensity increase of a factor of about 625. The implications of these changes for CCD operation will be discussed in section 10.

It is important to emphasize that SXT x-ray images do not show sensitivity artefacts analogous to what is observed in the visible light images. This has been proven by carefully comparing the intensity of the same x-ray feature on a damaged area and at an undamaged place on the CCD at the times of *Yohkoh*
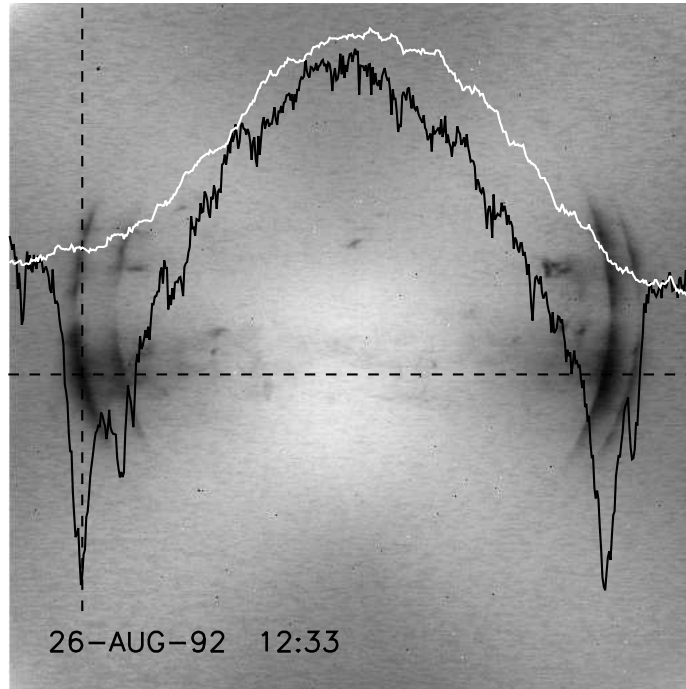
Figure 37. Demonstration of decrease in CCD optical sensitivity caused by soft x-ray damage after nearly one year of use. Image scaled to reveal details. Curves are described in text.

pointing ofsets. The reason the x-ray sensitivity is not impacted by the radiation damage has to do with the overlying gate structure of the uniphase CCDs which causes the device to have a different response to x-rays and long wavelength light.

A mission-long movie of diffuser images (Acton, 2014) nicely demonstrates the evolution of the diffuser image with time. Up until 13 November 1992 radiation damage accumulated with little evidence of annealing After that entrance filter failure most of the smaller artefacts gradually disappeared entirely and the heavily-irradiated limb features became far less dominant.

Figure 38 presents a mission-long light curve of the total signal in CCD rows 256 to 511 and columns 1 to 1023 of each diffuser image. (The limited CCD area sampled is chosen so that full resolution partial images, acquired after 24 January 1998 can be included.) Times of known entrance filter failures are indicated by the dotted vertical lines. Note the quasi-exponential decrease in diffuser signal up until November 1992, shared by all optical images. After this, when almost all of the visible light entering the SXT was coming via the x-ray mirror, such a decrease was never again observed. Interpretation of the mechanisms of optical sensitivity decrease are discussed in 7.1.

Figure 39 displays, on a linear scale, the diffuser signal for the period following 13 November 1992. Between entrance filter failures the diffuser image signal varied sinusoidally in step with apparent solar diameter. In order to study the
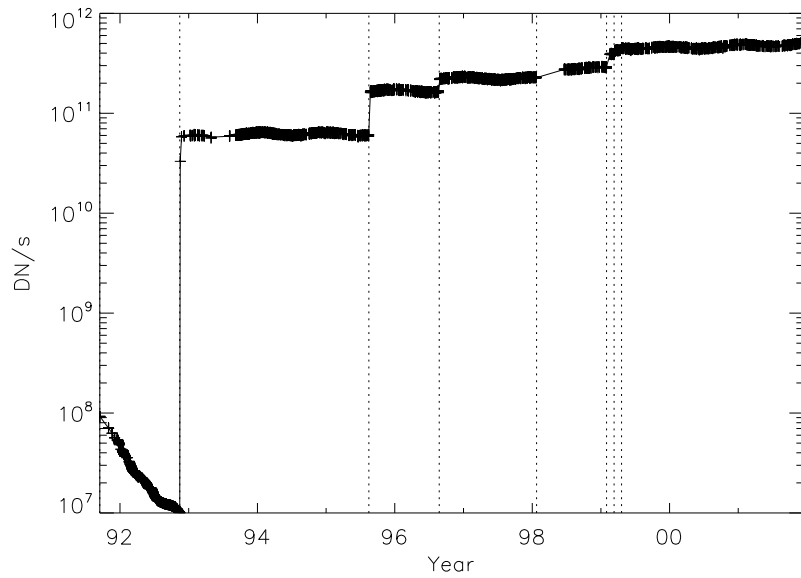
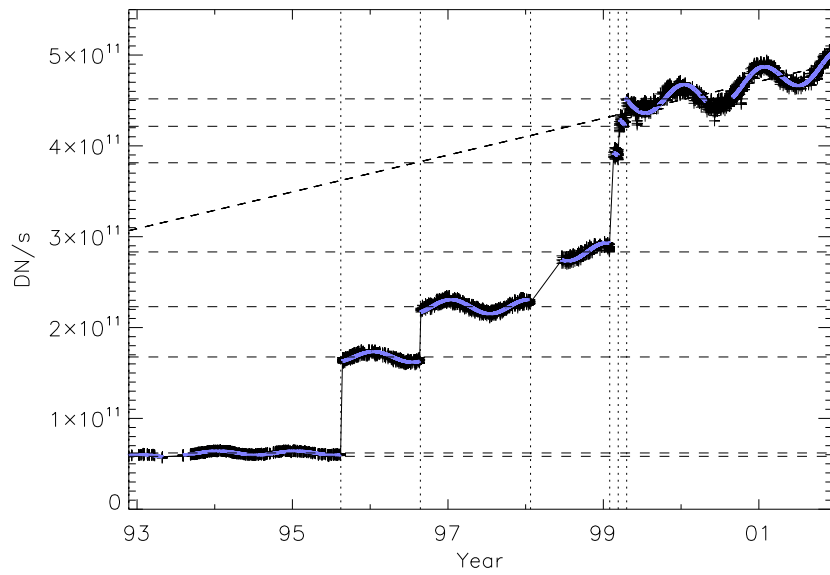**Figure 38.** Mission-long light curve of diffuser image signals.

Figure 39. Sinusoidal fits to diffuser signal amplitudes.

intensity changes at the steps this variation has been fitted with a sinusoidal expression of the form

$$Sig = A + Bt + C\sin(Dt + E) \tag{1}$$

where Sig is the diffuser signal, A is the mean signal, B allows for a slope to the wavetrain, C is the amplitude of the sine wave, $D = 2\pi/period$, E is the phase and t is time in seconds. A, C, and E were determined by fitting the interval 5 August 1993 to 15 August 1995 with B constrained to 0.0 and D to the period of a solar year (365.2425 days). This fitting determined the phase (E) and the ratio of the mean signal to the sinusoidal amplitude, i.e., $C = 0.035A$. For other failure intervals only the mean signal, A, was determined by the fitting. Other parameters were held constant to the values determined by the 5 August 1993 to 15 August 1995 fit. The value of A for each time interval is given in Table 7

Figure 40 illustrates the fitting for early and late in the mission. The two year interval on the right of the upper curve was the reference interval used for determining sinusoidal amplitude and phase. Note that for the fragmentary period prior to 5 August 1993 the signal is lower by about six percent. This and the single low diffuser signal obtained on 16 November 1992, better illustrated in Figure 41, indicate that the diffuser signal did not attain a stable level until about September 1993. Perhaps the entrance filter did not entirely fail or there may have been flaps of filter material partially intruding into the optical path for awhile. An alternative explanation could be that the enhanced UV flood (section 10.2.1) from full-spectrum sunlight off of the x-ray mirror took some time to increase the response of the CCD to visible light by annealing out some of the accumulated damage from ionizing radiation. In any case, we assume that the filter-ring open area derived from the diffuser data represents the open area to be used in adjusting the x-ray sensitivity of the SXT.

Figure 39 and the bottom panel of Figure 40 show that following the entrance filter failures of 1999 the stray light signal began a linear increase of about four to five percent per year that continued until the end of the mission. This increase appeared in every measure of SXT stray light; diffuser, leak monitor and terminator images. It is not understood what caused this stray light evolution as it is too smooth, enduring, and steady to be attributed to entrance filter ruptures. Our best guess is that the UV flood after 1999 was sufficiently strong to gradually anneal the ionizing radiation damage to the CCD that caused the evident decrease in sensitivity to visible light. As this phenomena appears to have no impact on x-ray sensitivity the gradual change evident in Figures 39 and 40 is not taken into account in the SXT x-ray sensitivity adjustment software.

It immediately catches the eye in, e.g., Figure 39 that, except for the failures of 1999 the increases in stray light are very nearly digitally incremental. I.e., the steps are in 1, 2, 1, 1, 2, and 1 increments. This discovery helps to better define the changes in entrance filter open area for the purpose of SXT x-ray sensitivity calibration.

Adding up the increments suggests that there are 8 totally open 30° sectors in the entrance filter ring after the final failure on 20 April 1999. The diffuser signal at that time was 4.52×10^{11} DN^{-1} sec^{-1} indicating a diffuser signal increase
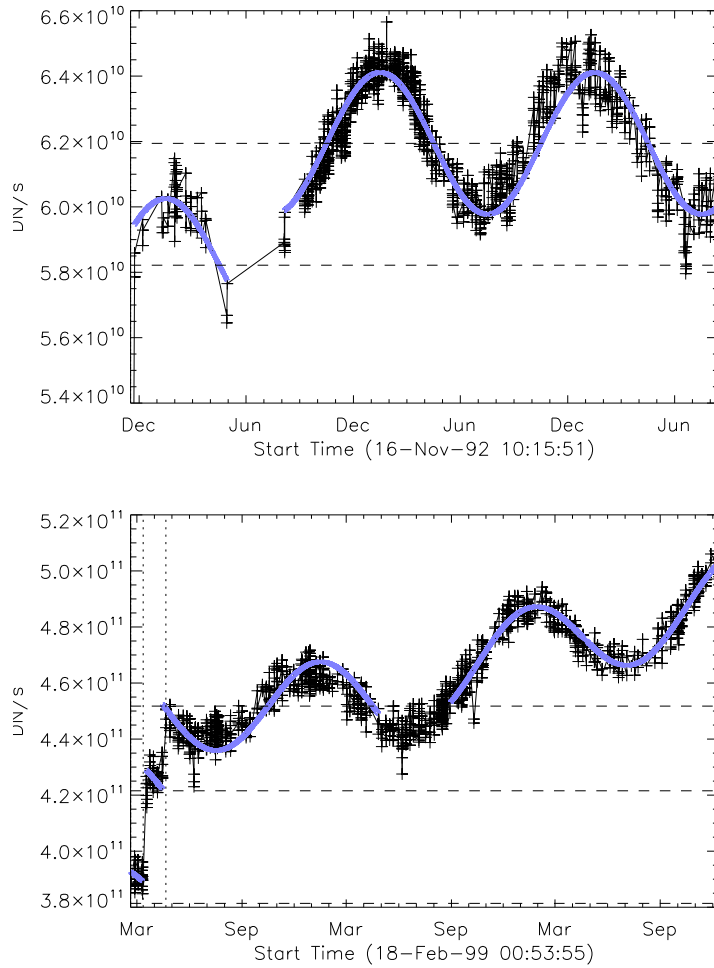
Figure 40. Diffuser signal and sine fits early and late in the *Yohkoh* mission. The horizontal broken lines show the base amplitude of the sine fits.

per open sector of approximately 5.66×10^{10} DN^{-1} sec^{-1}. If we take the fitted amplitudes listed in Table 7 as genuinely measuring the open filter area then we can compute the fractional open area of the entrance filter ring after each failure. The results of this analysis are given in Table 7.

8.5. Visible-light Terminator Images

The scientific return of the SXT would have been severely compromised had it not proven possible to acquire x-ray-free stray light images for an interval of about 13 seconds at the end of each orbital day. During this brief period the upper atmosphere of the earth absorbs the solar soft x-rays but atmospheric refraction and extinction have not yet significantly affected the visible stray light
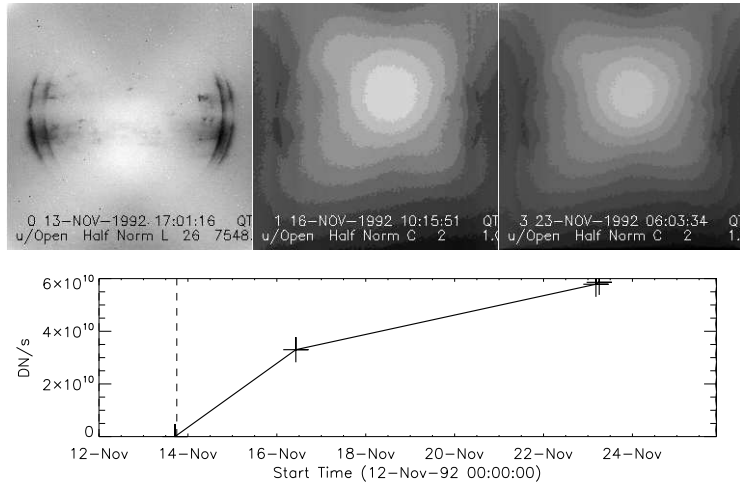
Figure 41. Diffuser signal around time of November 1992 entrance filter failure.

Table 7. Stray Light Amplitude

Failure Date	Diffuser Signal	Open Sectors	Open Fraction
13-Nov-92	5.822×10^{10}	1.03	0.086
1-Aug-93	6.194×10^{10}	1.10	0.091
16-Aug-95	1.676×10^{11}	2.97	0.247
24-Aug-96	2.230×10^{11}	3.95	0.329
24-Jan-98	2.832×10^{11}	5.02	0.418
30-Jan-99	3.814×10^{11}	6.75	0.563
12-Mar-99	4.216×10^{11}	7.47	0.622
20-Apr-99	4.518×10^{11}	8.00	0.667

pattern, yielding exposures recording only the visible stray light. These so-called terminator images are used to correct for stray light in the x-ray images obtained after 13 November 1992 18:00.

Figure 42 displays results of a special calibration experiment, run in flare mode, which acquired partial frame images in x-rays (AlMg filter) and stray visible light from the 2 regions of interest indicated on the inset image. The 2 sunsets were observed on 19-DEC-1994 05:04:24 to 05:09:04 (diamonds and triangles) and 18:02:30 to 18:06:38 (crosses and asterisks). The scaling of the curves has been adjusted to make the pre-sunset signals coincide. Note that x-ray absorption sets in for the west limb region about 12 seconds earlier than for the east limb region because the solar west limb leads at orbit sunset. The increase of the x-ray curve designated by crosses on the left is caused by adjustment of the SXT automatic exposure control during the first 5 exposures of this transit and can be ignored.
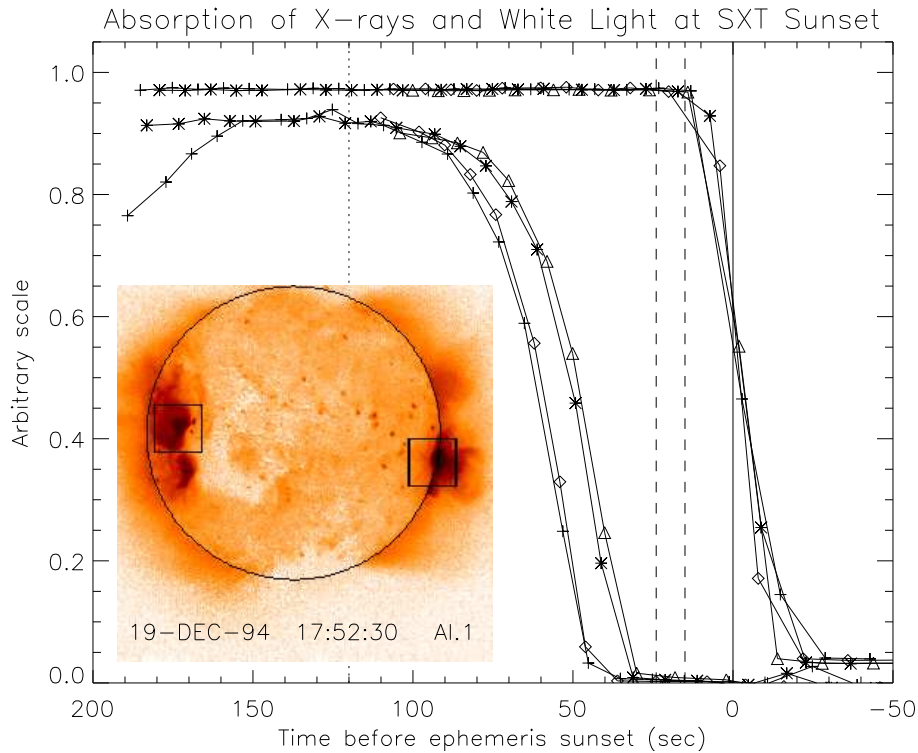
Figure 42. Inset, east and west observing regions. Upper curves, stray visible light. Lower curves, x-rays. Cross and diamond, west limb region. Asterisk and triangle, east limb region. Dotted line at 120 sec, beginning of x-ray absorption. Broken vertical lines, interval (15-24 sec) for acquiring Al.1 terminator images. Interval for other analysis filters is 12-24 sec. Vertical solid line, time of *Yohkoh* ephemeris sunset.

The SXT is equipped with two 6-position filter wheels (see Tables 4 and 6) in front of the focal plane. Each filter wheel has one open position and five filters (Tsuneta *et al.*, 1991). Presence of stray visible light within the telescope dictates that the open-open filter position, the most sensitive x-ray configuration, is unusable. The thinnest SXT analysis filter (Al.1, 126.5 nm Al, approximately six cm in front of the CCD) transmits about 10^{-6} of visible stray light through the thin Al layer. This filter also developed at least three pinholes, which fortuitously lie slightly off of the normal position of the solar image. Finally, the filter wheel assembly itself is not light tight and even for the thicker filters some stray light finds its way through weight relieving holes in the filter wheels and onto the CCD. The pattern and intensity of this stray light varies from filter to filter, with season (solar diameter), and with *Yohkoh* pointing. The stray light intensity increases stepwise with each entrance filter failure. Figure 43 illustrates the pattern and relative intensity of the stray light pattern for all five of the SXT analysis filters for a time about a year following the major failure of 13 November 1992.
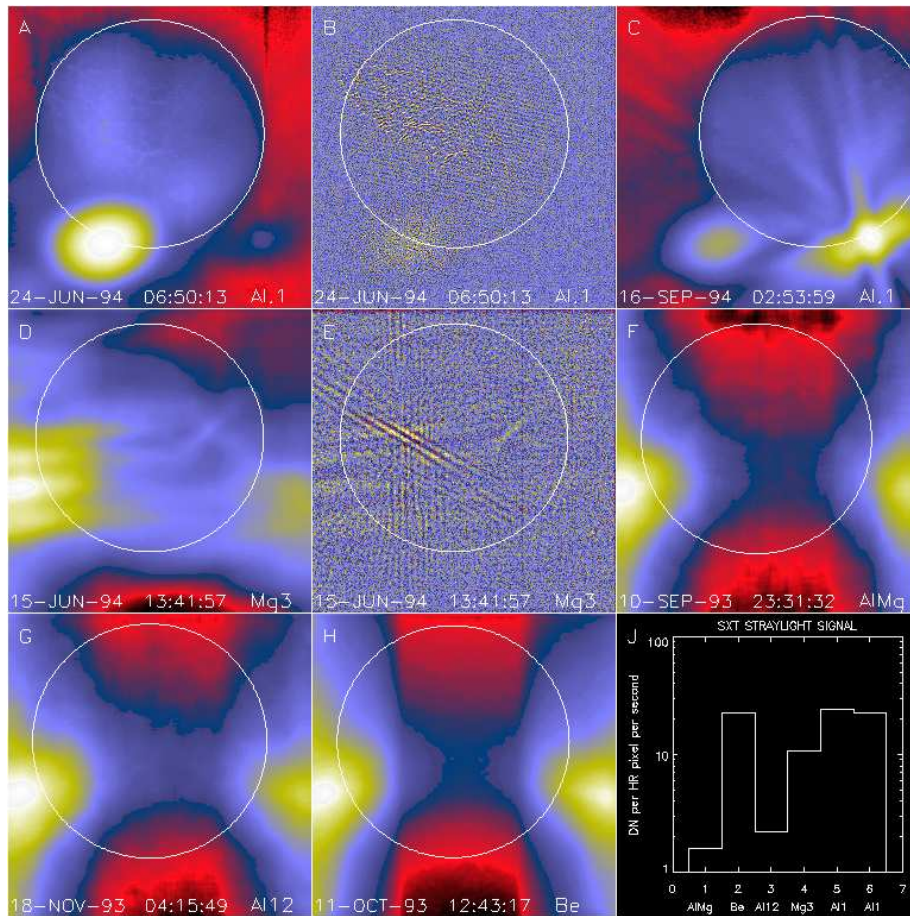
Figure 43. Stray light pattern for each of the SXT analysis filters. The location and size of the solar disk is indicated by the circles. Two examples are given for thin aluminum (Al.1) to demonstrate the effects of pointing on the Al.1 stray light pattern. These two images (A and C) are displayed with logarithmic scaling. All of the others are scaled linearly. Image B is flattened and clipped to show some of the fine scale structure of the Al.1 stray light image. Panel E is a correspondingly processed image for Mg3. Panel J illustrates the relative strength of the stray light signal for each of the filters. The righmost Al.1 datum (#6) of panel J corresponds to the image in panel C. AlMg, the filter least affected by stray light, is used, with the shutter closed, for SXT dark frame exposures. Filter designations are given on the lower right corner of each panel.

As is clearly evident in Figure 43 the stray light patterns for the totally opaque filters AlMg, Al12 and Be are quite similar. The Mg3 stray light patterns shown in panels D and E exhibit what appear to be wrinkles and is not fully understood. This is largely irrelevant as this analysis filter was seldom used.

Panel J of Figure 43 illustrates the relative total intensity in the terminator images on a logarithmic scale. The stray light for AlMg (column 1) and Al12 (column 3) are low because these shiny metals reflect most of the stray visible light which falls on them. The Be filter (column 2) has a diffusive surface so that

much more of the stray light is scattered internal to the filter wheel assembly where it can find its way to the CCD. Most of the stray light of Al.1 (columns 5 and 6) penetrates the 126.5 nm of Al or comes through the pinholes although the characteristic stray pattern of the opaque filters, i.e., coming at the sides, is also present for Al.1.

Figure 44 illustrates the complex, low-level, artefacts in Al.1 images. For this reason AlMg became our primary FFI filter after 1992. Although special care must be exercised in interpreting Al.1 images of faint coronal regions the stray light problem is much less important for the vastly brighter flare and active region features. The Al.1 stray light network varies in detail as well as in position and intensity. It is at its brightest right after CCD bakeout. We believe that this complex pattern is caused by doubly-reflected stray light that enters through the Al.1 filter pinhole(s), reflects off the face of the CCD onto the back of the Al.1 filter and thence back onto the CCD where it is detected. This interpretation can account for the varying pattern as the thin Al membrane distorts under direct solar heating by sunlight focussed on it by the x-ray mirror. Although this particular stray light feature has been extensively studied (see the SXT Observation Notaes section of the YLA) it has not proven possible to derive a general correction for this (faint) stray light pattern.

8.6. Chronology of Entrance Filter Failures

As a result of failures of the thin-film entrance filters, stray visible light began to enter the telescope on 27 October 1992. On 13 November 1992 an inner layer of the duplex entrance filter system failed and the inside of the telescope was flooded with visible light. Aspect sensor images could no longer be acquired as even the shortest exposures were totally saturated.

It has not been possible to ascertain the exact cause of failure. As shown in Figure 16 the filters are quite well protected with a very small area and solid angle viewing space. Micro-meteorite impact cannot be ruled out but seems unlikely to account for so many failures. Most of the failures have appeared with the first exposure following orbit night so it seems likely that cumulative degradation of the Lexan plastic film due to thermal stress at the day-night and night-day transitions may be a factor in the filter ruptures.

As discussed in section 8.1.1 and shown in Figure 26 the stray light image coming off the x-ray mirror is fairly well focussed in the direction orthogonal to the radial direction to the failed sector. Thus, after-minus-before difference images may show a well-defined limb in this orthogonal dimension (i.e., $90^{/}circ$ from the failed sector which identifies (with an $180°$ ambiguity) which sector has failed. Figure 45 was prepared to help identify which entrance filter sectors failed at each event. The terminator images comprising this Figure have been co-aligned. The black cross indicates the location of solar disk center. All panels of Figure 45 have been prepared by subtracting a 21-pixel boxcar smoothed image from the terminator image to bring out the fine structure. Panels A and B were obtained shortly after the November 1992 and August 1995 failures. In A a well-defined limb appears at the 04:00 and 10:00 o'clock positions, indicating failure of sector 6 or 12. As we know that the outer filter of sector 6 failed on 27
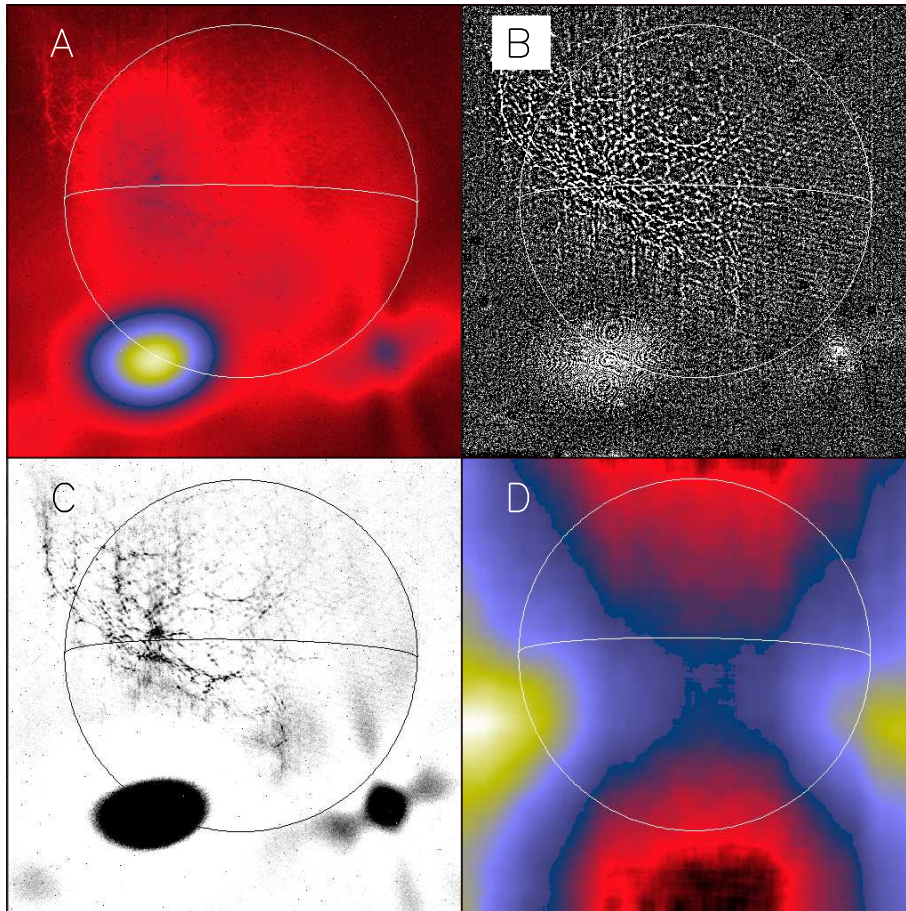
Figure 44. A. Al.1 terminator image of 23 January 1993 05:33. B. Difference image illustrating the NE to SW grill pattern on the solar disk (better seen in Figure **??**). C. Difference image showing the semi-random stray light network. D. AlMg terminator of 25-JAN-1993 07:52, shown for comparison.

October 1992 we assume that the inner filter of sector 6 failed on 13 November 1992. Panel B shows an additional limb feature at about 01:30 and 07:30 o'clock, indicating failure of sector 3 or 9. Panel C is the difference image of the image in B minus a similar image taken shortly before the failure. The new limb features are evident. Panels D through H are similar after-minus-before difference images for subsequent failures, not all of which show clear limb features, perhaps because of inadequate statistics. Panel I, created in the same way as panels A and B, is the last good Al.1 terminator image of the mission, obtained on 22 November 2001 15:18. Except for angles around 12 o'clock a nearly complete limb feature is displayed. Guesses of which sectors failed and when are summarized in Table 8 where the letters in column 2 correspond to the panels of Figure 45.

Table 8 lists the known SXT entrance filter failures. Failures involving the inner filter are readily detected by a step increase in visible stray light within the
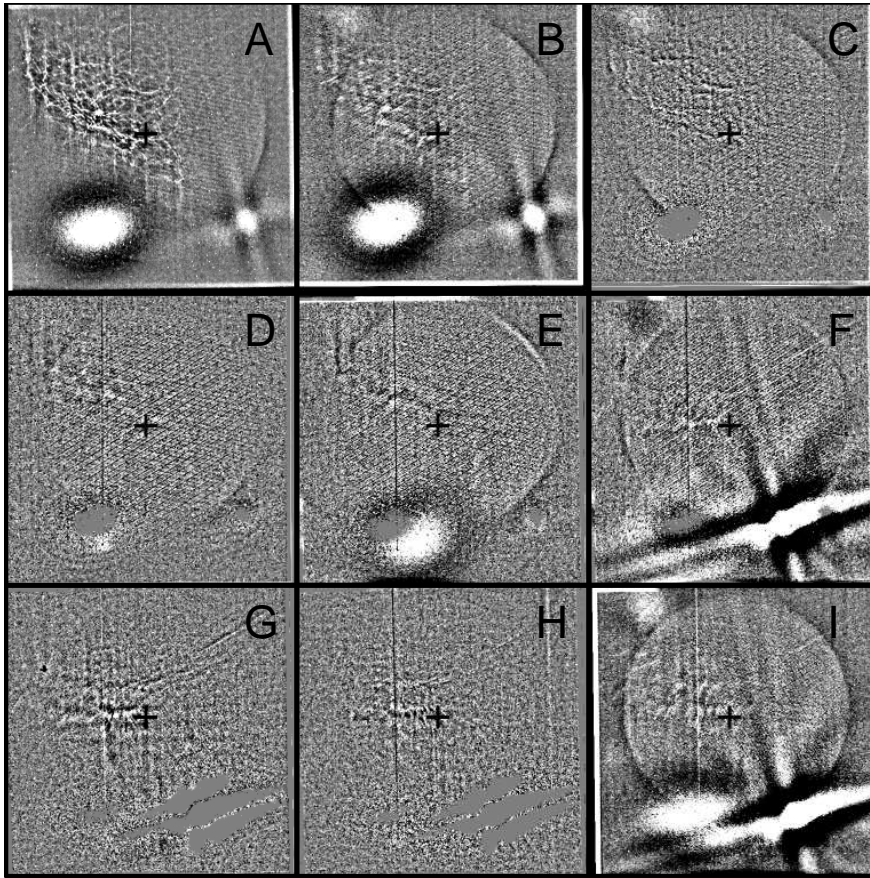
Figure 45. Change in Al.1 terminator at each entrance filter failure.

Table 8. SXT Entrance Filter Events

Event	Fig. 45	Date	Failure	Change
0.		27 Oct 1992 05:59	Outer sector 6	First failure
1.		27 Oct 1992 07:18	Outer sector 7	Second failure
2.	A	13 Nov 1992 18:00	Inner sector 7	PH[1]in the SE
3.	B,C	16 Aug 1995 08:04	Sectors 5 and 11	New PH in the NE
4.	D	24 Aug 1996 07:00	Sector 2	
5.	E	24 Jan 1998 00:00	Sector 8	Expanded PH in the SE
6.	F	30 Jan 1999 23:17	Sectors 6(inner) and 12	PH in the SW
7.	G	12 Mar 1999 02:00	Part of sector 4	Expanded PH in the SE
8.	H	20 Apr 1999 19:02	Rest of sector 4	Now 8 open sectors
9.	I	11 Feb 2000 13:00	No stray light change	X-shift enhances SE PH
10.		14 Dec 2001 21:12		End of mission

[1]Pinhole.
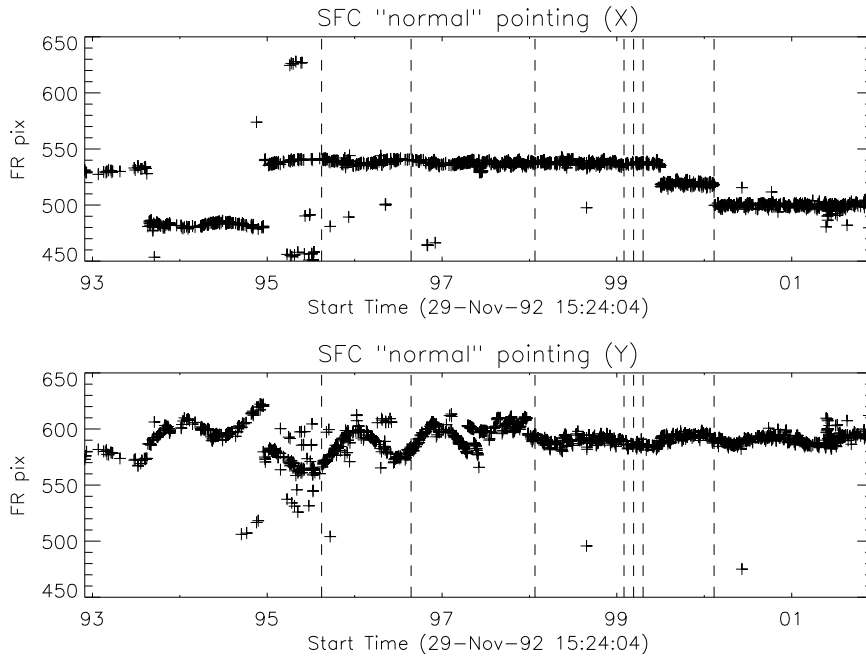
Figure 46. Yohkoh pointing history for so-called "normal" pointing.

instrument. Shortly following the 13 November 1992 failure regular stray-light-monitor images were obtained for the purpose of detecting additional entrance filter changes. Failures involving only the outer filter, such as the two on 27 October 1992, cause too small a change in the stray light to detect after 13 November 1992.

8.7. Details of Stray-light Changes at the Steps

As the SXT entrance filters failed the stray light increased stepwise within the instrument. In addition, on at least 2 occasions, a new pinhole appeared in the Al.1 analysis filter at or near the same time as the stray light step. This is presumably due to the more intense thermal shock to the thin aluminum filter. We were extremely fortunate that there were no Al.1 pinholes on the image of the solar disk in normal *Yohkoh* pointing.

Yohkoh pointing was quite variable with season. Also, from time to time, the pointing was adjusted to move the heavily irradiated limb regions to different places on the CCD. Beginning in 1998 *Yohkoh* pointing was periodically adjusted by the SXT Chief Observer to ameliorate the seasonal variation in Y (north-south) in order to improve our ability to correct for stray light. Figure 46 illustrates the pointing history throughout the portion of the mission affected by stray visible light.

There are 4 means of monitoring stray visible light in SXT. These are the Al.1 and AlMg terminator images (SFCs), the leak monitor images (See Figure 32) and weekly exposures obtained using the opal glass diffuser. The amplitude and
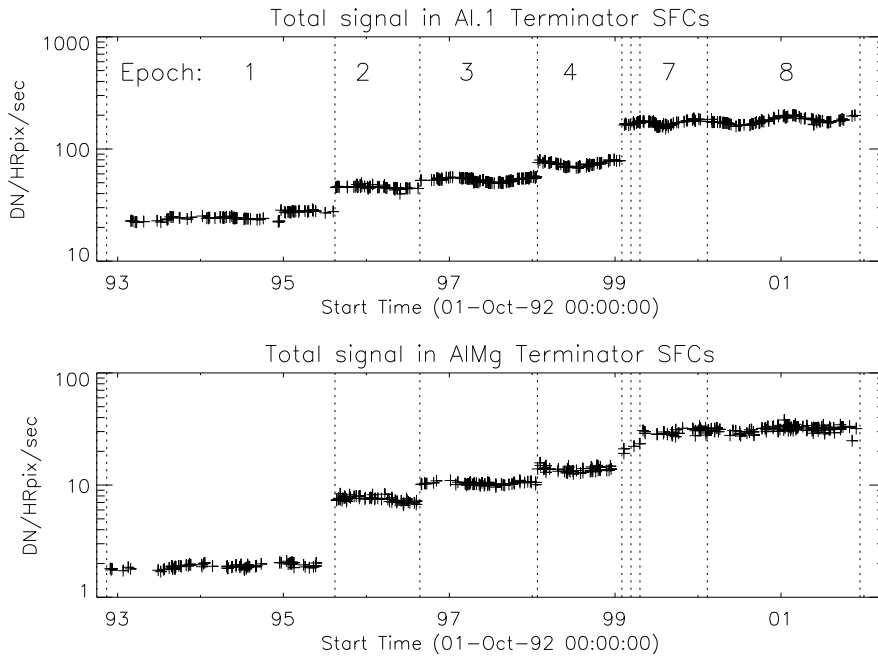
Figure 47. Comparison of Al.1 and AlMg total stray light signals.

evolution of stray light as recoded by the different techniques are illustrated in Figures 47 and 48. The latter figure shows details of the differences in the stray light changes for the interesting interval in 1999 spanning leak epochs 4 to 7. Vertical lines in all these figures denote the time of recorded stray light changes

8.8. Diagnosis of Open Filter Area

Table 8 presents conclusions of which filters opened at each stray light step. Clearly, there are details not grasped by this difficult analysis. E.g., it is very hard to believe that both front and rear filters in 2 sectors (5 and 11 or 6 and 12) 180° from each other would all open simultaneously. Furthermore, examination of Figure 39 shows that filter sectors do not always fail entirely. Therefore a direct measure of stray light levels from analysis of the diffuser signal will be used as a proxy for entrance filter open area.

Assumptions are (1) that the intensity of the diffuser signal after 13 November 1992 is a faithful measure of the fraction of the entrance filter ring for which both outer and inner filters are open, (2) sector 6 of the outer filter ring opened on 27 October 1992 but sector 6 of the inner ring didn't fail until 30 January 1999 and (3) as of 20 April 1999 eight and only eight sectors had completely opened. The second assumption results from the analysis of Figure 45 which seems to indicate that inner sector 6 failed on 30 January 1999. Assumption (3) is buttressed by the semi-digital nature (Table 7) of the failure steps, adding up to 8. We have no way of knowing if additional outer ring filters failed after the first failures in October 1992. Table 8 gives conclusions at which sectors opened and when.
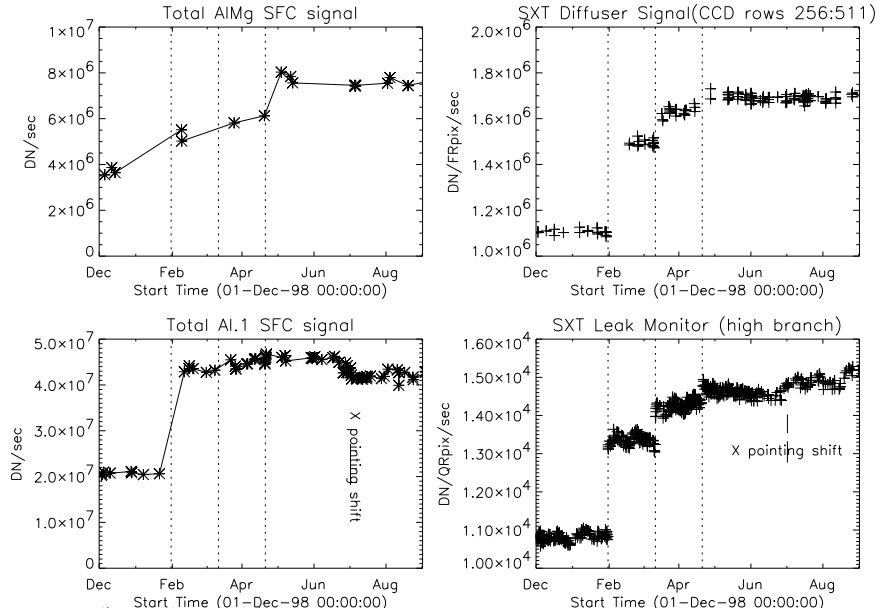
Figure 48. Comparison of stray light signals from all 4 monitoring systems in 1999.

Table 9. Entrance Filter Open Fraction

Event Date	Old open Fraction	New open Fraction
30-Aug-91 01:30	0.000	0.000
27-Oct-92 07:18	-	0.071
13-Nov-92 18:00	0.083	0.123
1-Aug-93 00:00	-	0.128
16-Aug-95 08:04	0.167	0.284
24-Aug-96 07:00	0.250	0.366
24-Jan-98 00:00	0.333	0.455
30-Jan-99 23:17	0.417	0.563
12-Mar-99 02:00	0.500	0.622
20-Apr-99 19:02	0.583	0.666
11-Feb-00 13:00	0.583	0.666
14-Dec-01 21:12	0.583	0.666

Given these assumptions, a model treating each (outer and inner) filter rings separately and the diffuser intensities given in Table 7 it is straightforward to compute the increases in SXT spectral sensitivity at each failure step.

All of the SXT programs for deriving physical parameters from instrumental units treat the entrance filters as a single ring, i.e., combining outer and inner. In order to leave these programs unchanged an effective single ring open area has been derived which yields an SXT spectral sensitivity equivalent to the full
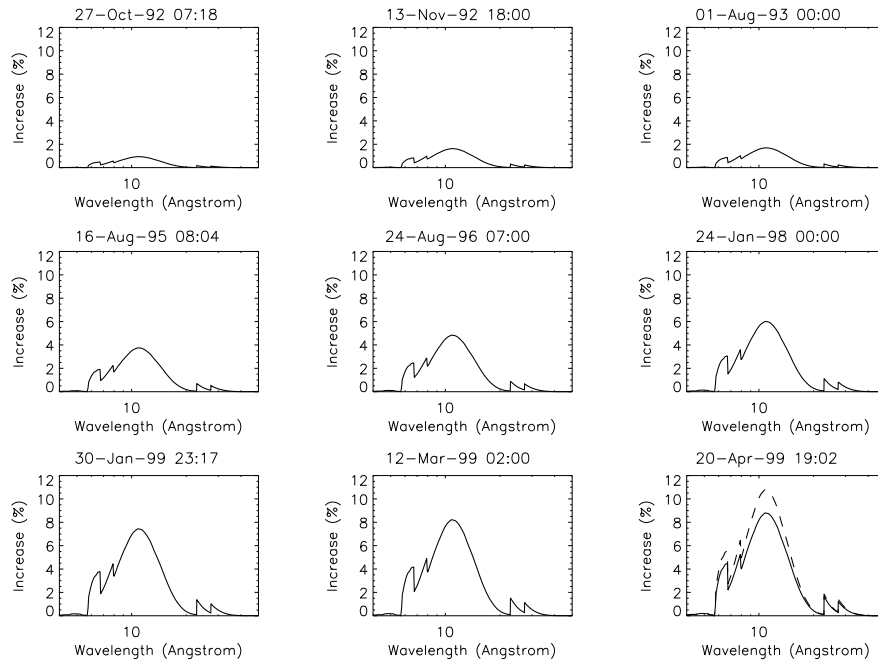
Figure 49. Absolute increase in SXT spectral sensitivity due to entrance filter failures for the thin aluminum analysis filter. The broken curve in the lower right panel shows the increase for the hypothetical case where all outer filters are open, the maximum allowable error in the analysis.

calculation with 2 filter rings. This permits incorporating the new calibration results by the simple updating of a single *Yohkoh* data base. A comparison of the old and revised open entrance filter fraction is given in Table 9. The entry for 11 February 2000 flags the approximate beginning of the linear increase in diffuser signal and has no known relation to the open fraction of the entrance filters. The increase in spectral sensitivity for the thin aluminum analysis filter at each of the 9 failures is illustrated in Figure 49. The increases in sensitivity for all of the thicker filters will be less than for thin aluminum.

9. SXT Stray Light Correction

9.1. Impact of Stray-light Contamination

The comparative signal levels of x-rays and visible stray light are illustrated in Figure 50. For this comparison the on-disk signals of each Half resolution (HR) image were normalized to DN HRpix^{-1} sec^{-1}. For convenience in plotting the x-ray signals from the selected SXT Science Composite (SSC) images are about 14 days apart. All of the stray light terminator (SFC) images are included. For the Al.1 SFCs the disk area sampled does not include the pinholes to the south.
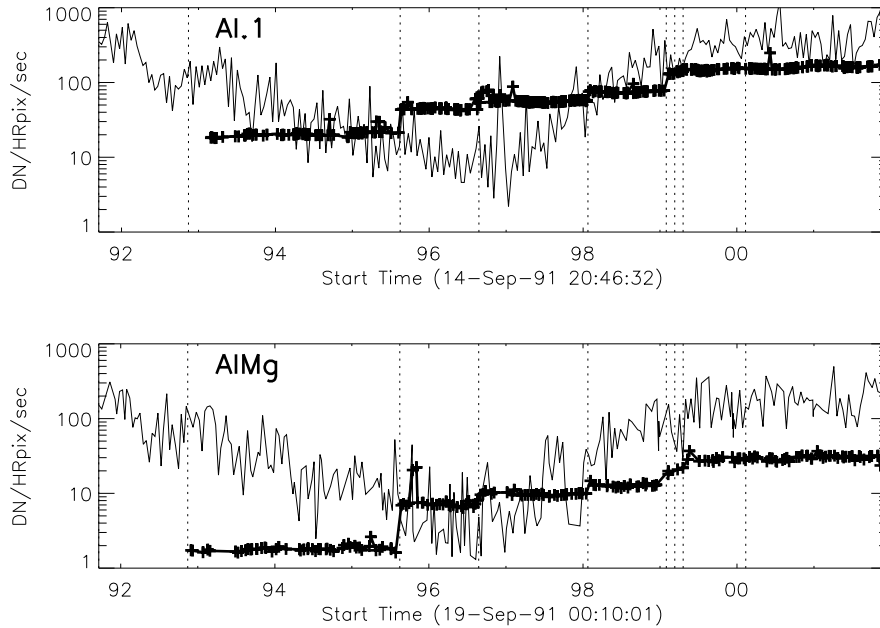
Figure 50. Comparison of mean x-ray (thin lines) and stray light (heavy lines) signals for the two thinnest SXT analysis filters. Dotted lines indicate times of filter failures. Vertical excursions of stray light points are from SXT offpoints.

It is clear from Figure 50 that, for disk-averaged signals, the stray light corrections are significant, especially for Al.1. During solar minimum the stray visible light exceeds the x-rays. However, this is not the whole story because the SXT x-ray images have very high contrast. For example, a typical active region x-ray signal exceeds 20,000 DN HRpix^{-1} sec^{-1}, quiet coronal loops are of the order of 100 DN HRpix^{-1} sec^{-1} while coronal holes have signal levels of only 10 DN HRpix^{-1} sec^{-1}. It is indeed fortunate that it has proven possible, in most cases, to correct the x-ray images for visible stray light by subtracting a properly chosen and adjusted SFC from the x-ray exposures. This is more successful for the AlMg images than for the Al.1 exposures because of the more complicated, time varying, nature of the stray light patterns through the Al.1 analysis filter.

The following sections describe our efforts to obtain the best possible stray light correction throughout the SXT mission.

9.2. Terminator SFCs

Terminator images were collected at every opportunity to get good coverage over a range of spacecraft pointings and time. Periodically over the course of the *Yohkoh* mission, further failures of the front entrance filters occurred. Over each of the epochs a set of terminator images were collected with as complete a coverage of pointing and solar radius as possible. Examples of terminator SFCs

collected during leak epoch 1 are shown in Figure 43. For a variety of operational reasons the coverage is necessarily incomplete. Special observations such as *Yohkoh* offpoints are treated on a case-by-case basis with special terminator images acquired at the time.

The correction is applied by selecting the terminator image for a given leak epoch which best matches the x-ray image in *Yohkoh* pointing and solar diameter. For each x-ray image the SFC is exposure-normalized and subtracted from the x-ray exposure to remove the white light contamination. For Al.1 an additional step of subtracting the grill pattern (see Figure 44) from the on-disk portion of the image. This correction does not alter the total intensity as the net intensity of the correction pattern equals 0.

9.3. Synthetic SFCS

While the correction of the white light leak is adequate in many cases, there are instances where the nearest terminator image is not sufficiently close in pointing and solar radius and the correction is poor. The SXT team (Shirts *et al.*, 2003) derived a multi-dimensional algorithm to interpolate, pixel by pixel, available terminator images to provide parameters for creation of synthetic terminator images for a finer grid of spacecraft pointings and solar radii.

The generation of parameters for synthetic terminator images is done on an epoch by epoch basis corresponding to successive failures of the front entrance filters. Table 8 details the epochs. Throughout each epoch, terminator images are obtained as often as possible.

9.3.1. Application of the Interpolation Algorithm

We have tested the interpolated terminator images by generating a synthetic terminator at the same coordinates and date as the actual terminator. The results are shown in Figure 51 as the ratio of the mean difference between the synthetic terminator and the actual terminator divided by the brightness of the synthetic terminator. This analysis demonstrates that the synthetic method is sound although better in some epochs than in others. The scatter in the figure is indicative of the natural variation of the terminator images. It is much larger forAlMg due to thestatistical variation of the fainter AlMg leak images. This variation is in the form of an overall scale factor and does not unduly affect the morphology of the leak pattern. This residual variation is removed by using a second order leak correction which adjusts the overall scale of the leak or synthetic leak to a particular X-ray data image until the lower left corner of the corrected image is consistent with the expected scattered x-rays from the solar disk.

9.4. Choice of Stray-light Correction Image (SFC)

Neither terminator or synthetic SFCs always provide the optimum correction for stray light, especially for the thin aluminum (Al.1) analysis filter. A procedure is required to choose which type of SFC to use for correcting a given SXT image.
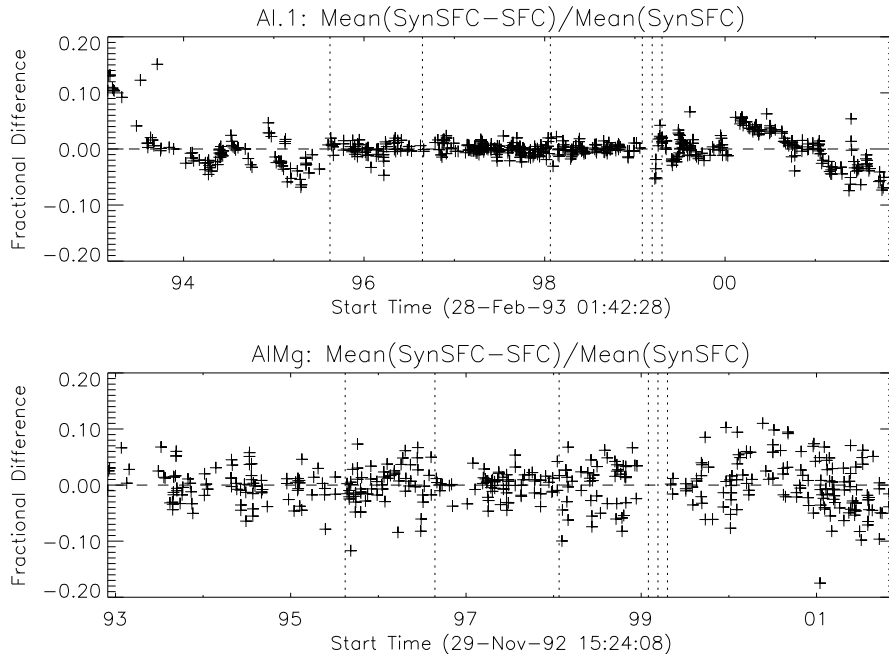
Figure 51. Accuracy of the interpolation algorithm produced by generating interpolated images at the same pointing etc. as a real terminator image. The vertical lines indicate the times of entrance filter failures.

The signal in off-disk areas most affected by stray light, namely 1.1-1.25 Rsun for azimuths 125-220 and 310°-330°, for all Al.1 level-2 FFIs have been prepared for comparison with AlMg FFIs taken near in time. For images taken close together in time, the best-corrected Al.1 image is that for which the signal in the sample areas is closest to twice the signal (under most conditions the SXT full-sun Al.1 images have an integrated signal very close to two times the equivalent AlMg image with the same exposure) in the same area for the AlMg image. The areas sampled for this comparison are shown in Figure 52.

Making this comparison for all Al.1 level-2s corrected with of SynSFC and the same Al.1 FFIs corrected with TermSFC shows where, on average, SynSFC or TermSFC are better. The chosen SFC type boundaries are listed in Table 10. The SXT analysis software employs this choice for both Al.1 and AlMg observations.

10. The SXT Charge-Coupled Device Detector (CCD)

The CCCD camera for the SXT utilizes a 1024×1024 pixel virtual phase (also called a uniphase device) CCD with 18.3 μm pixels manufactured by Texas Instruments (TI) at their Miho, Japan, facility. The principal of operation of this type of CCD is described by (Janesick, 2001). A TI virtual phase CCD was flown on the ESA Giotto mission. The performance of this CCD after seven years in interplanetary space has been dicussed by Kramm, Thomas, and Keller (1993).
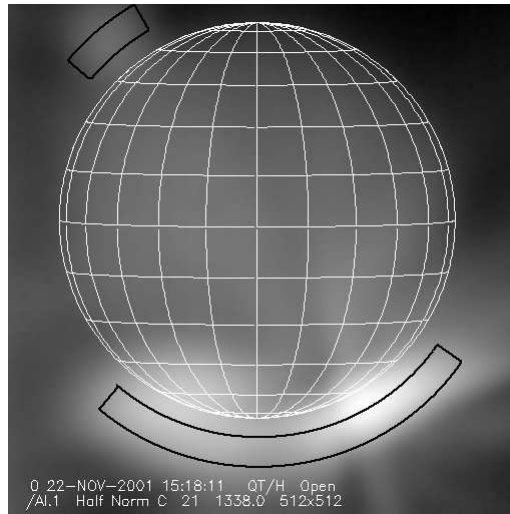
Figure 52. Image areas sampled for stray light correction analysis. The areas are fixed with respect to the solar image, i.e., not as absolute CCD coordinates.

Table 10. Choice of SFC

Start Date	SFC type
Yohkoh launch	No SFC required
13-Nov-92 18:00	TermSFC
24-Jul-93 00:00	SynSFC
16-Sep-94 00:00	TermSFC
24-Aug-96 07:00	SynSFC
30-Jan-99 23:17	TermSFC
20-Apr-99 19:02	SynSFC

The structures overlying the sensitive volume of the CCD are illustrated in Figure 56. Figure 57 shows the quantum efficiency of the CCD alone with and without an entrance filter. The selling points of this CCD for SXT were its relatively good soft x-ray sensitivity in the half of each pixel not covered by the polysilicon gate and its ready availability from JPL research inventory. Shin and Sakurai (2014) have discussed the subtle effect that the CCD pixel structure has on the point spread function of the SXT. Note that, in use, the sensitivity of the device longward of 100 nm was eliminated by metallic analysis filters (Table 6).

10.1. Amplifier Gain of the SXT CCD Camera

If the CCD camera gain changed during the *Yokoh* mission this would result in an over or under estimation of the x-ray flux. The electronic gain of the SXT CCD camera was set to approximately 100 electrons per analog-to-digital-converter (ADC) data number (DN) so that full-well capacity of the CCD would reach
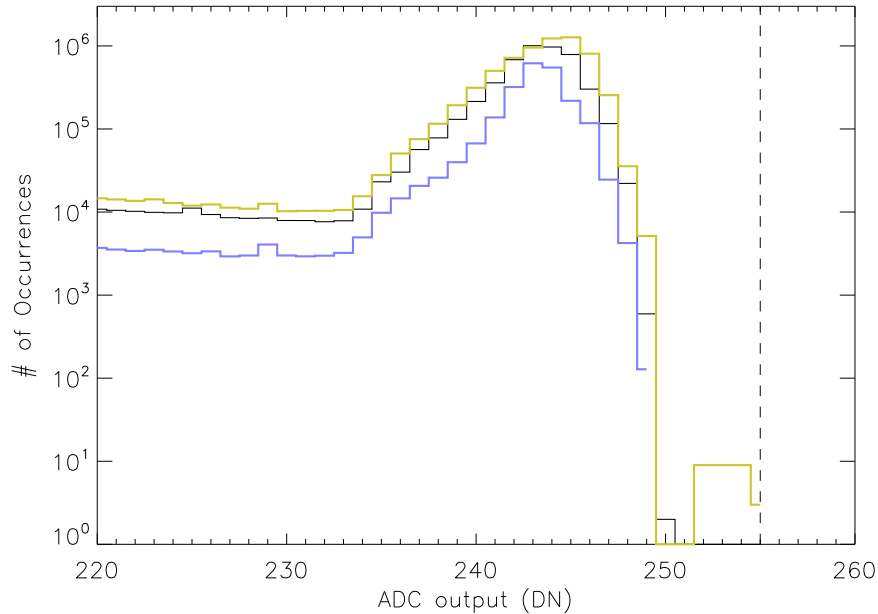
Figure 53. Histograms of DN values of full resolution SXT pixels illustrating full-well signals. The data have been divided into three equal mission time intervals indicated by the color of the histograms. Black: first third (460 images), blue: second third (102 images), yellow: final third (445 images). The broken vertical line denotes the maximum output of the ADC at 255 DN.

saturation (in full resolution mode) before the 12-bit ADC saturated. In 2×2 and 4×4 summed modes the ADC saturates first. The gain was set pre-launch to provide a full-well compressed signal for an average pixel of about 245 DN. Figure 53 illustrates histograms of the high-end signals of the pixels in 789 long-exposure FR images taken throughout the mission. The peak near $DN = 244$ demonstrates that the CCD camera gain was set properly. The width of the peak shows the pixel-to-pixel variation in full-well capacity while the few pixels with DN values above 250 are from anomalous pixels. The histograms for the early, mid, and late phases of the mission prove that the gain was stable throughout the mission. A shift of one DN at 244 DN would represent about a one percent change in gain.

An independent check of the temperature stability of the CCD camera amplifier is given in Figure 54 which shows the mean quiet corona signal (saturated pixels eliminated) taken with the AlMg filter through a CCD bakeout in January 1993. The increased scatter due to enhanced dark signal when the CCD was warmed to +20C does not mask the evidence for x-ray signal stability.

The preferred means of measuring CCD camera gain is by the photon transfer method (Janesick, 2001) whereby an extrapolation of a log-log plot of signal variance versus signal, for a range of exposures, yields the gain. An optical diffuser (section 8.4) was incorporated into the forward filter wheel of the SXT in order to provide CCD illumination for this calibration. Unfortunately, radiation damage
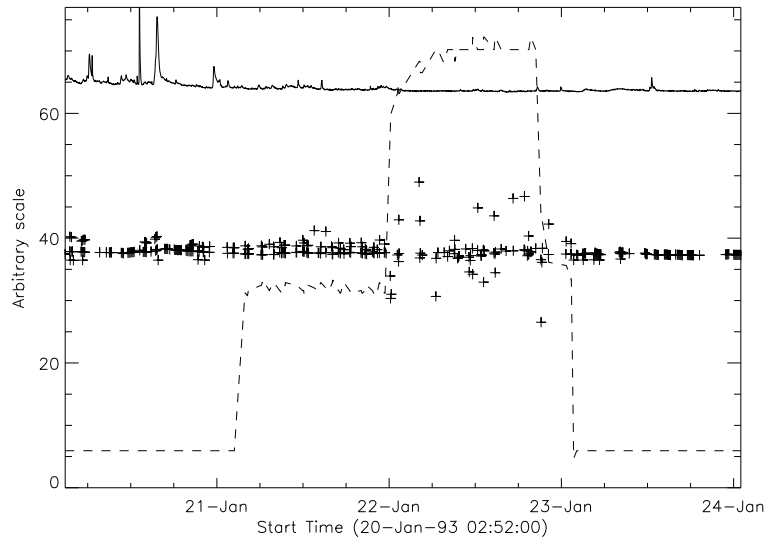
Figure 54. Demonstration that the CCD on-chip amplifier gain is not temperature dependent. Broken line: CCD temperature (-20C, 0C, 20C). Solid curve: GOES low channel signal on a linear scale. Crosses: Mean signal (unsaturated pixels, DN sec^{-1}) in AlMg full frame images. Increased scatter during +20C interval is caused by enhanced dark signal correction.

(section 10.2) increased fixed pattern noise and so compromised the visible-light response of the CCD that photon transfer experiments were difficult. Photon transfer experiments were executed in October 1992, April 1993, and twice in April 1996 (LaBonte, 1996). All of these experiments were consistent with a CCD camera gain of approximately 90 electrons DN^{-1}. The 1996 experiments by Barry LaBonte had a one sigma statistical error of a few percent.

As of June 2014 the default CCD gain in SXT analysis software has been changed from 100 to 90 electrons DN^{-1}. This change will result in a ten percent decrease in x-ray fluxes and emission measures derived from SXT observations.

10.2. CCD Damage from Ionizing Radiation

10.2.1. UV Flood

During CCD testing (only a bit more than one year before launch) Jim Janesick of JPL discovered that these devices suffered damage from ionizing radiation (x-rays in particular) that, when sufficiently severe, caused increased dark current, flat-band shift and, ultimately, unpinning of the device. Janesick interpreted this phenomena and determined that increasing the camera drive voltage (to -6V beyond the inversion point) plus exposure of the CCD to UV photons could, to some degree, ameliorate the problem (Acton *et al.*, 1991; Janesick, 2001). The flight results reported in section 10.2.2 demonstrate that, with sufficient overexposure, the problem persisted but the UV flood appears to have corrected it.
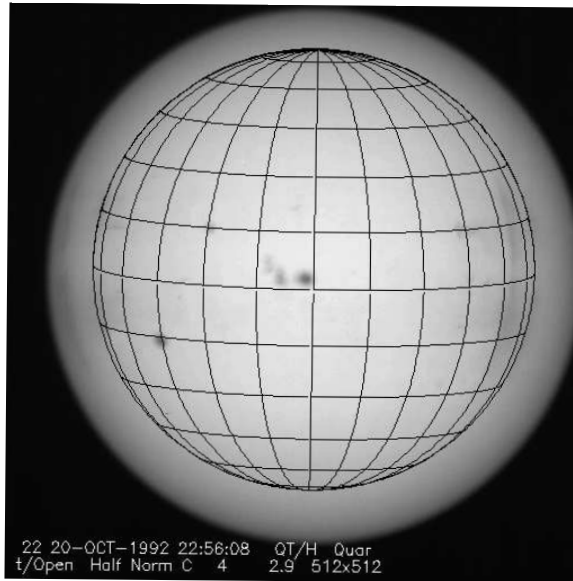
Figure 55. Picture using quartz defocus lens. Overlay shows position and size of an in-focus solar image.

As a result of Janesick's discovery a slightly negative quarts lens was incorporated in the forward SXT filter wheel to illuminate the CCD with an oversized (1.2 Rsun) out-of-focus 330-450 nm image of the sun from light passing through the aspect sensor optics (Figure 55). This blue-light flood, although lesser in photon energy than ideal, was intended to help neutralize the damage caused by the x-rays. The first 3-5 minutes of each daylight pass of *Yohkoh* was devoted to a blue-light flood of the CCD. As the transmission of the aspect sensor optics diminished this blue-light flood became correspondingly less intense. While all optical images showed clear evidence of CCD radiation damage (see section 8) by November 1992 there was asyet no corresponding evidence of enhanced dark signal in CCD dark frames.

After the 13 November 1992 entrance filter failure the blue-light flood became a much more effective UV flood, at least for the half of each pixel not covered by the polysilicon gate structure. As illustrated in Figure 58 intensity through the quartz lens on the CCD became nearly 10^{11} times higher than before. This was determined by modelling the CCD response from 0.1 to 1000 nm using absorption coefficients from the following references Palik (1985); Philipp (1985); Drummond (1936); Green and Keevers (1995); Henke, Gullikson, and Davis (1993); Narukage *et al.* (2011); Tan, Lemon, and French (2003); Kitamura, Pilon, and Jonasz (2007). It is probable that, absent the entrance filter failures, accumulated CCD damage from ionizing radiation would have, in time, rendered the most heavily irradiated portions of the CCD unusable.

Roughly one percent of the soft x-rays incident on the CCD were absorbed in the SiO_2 gate oxide layer, producing electon-hole pairs and the resulting radiation damage. As detailed by Acton *et al.* (1991) a certain fraction of these
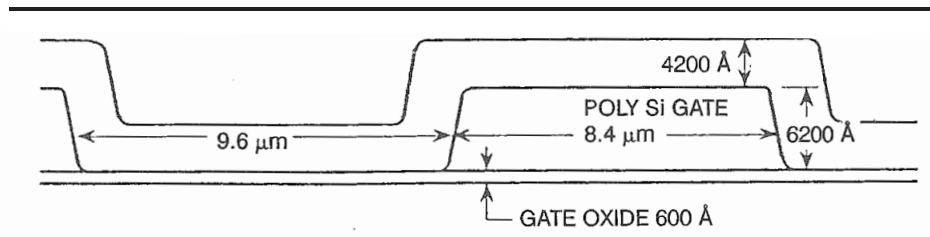
Figure 56. Schematic sketch of the structure of the Texas Instrument uniphase CCD used on the SXT. Not to scale, thicknesses in this figure are approximate. The actual thicknesses of the layers for the SXT flight CCD are: SiO_2 overcoat, 487 nm; Polysilicon gate structure, 770 nm; SiO_2 gate oxide, 63 nm.
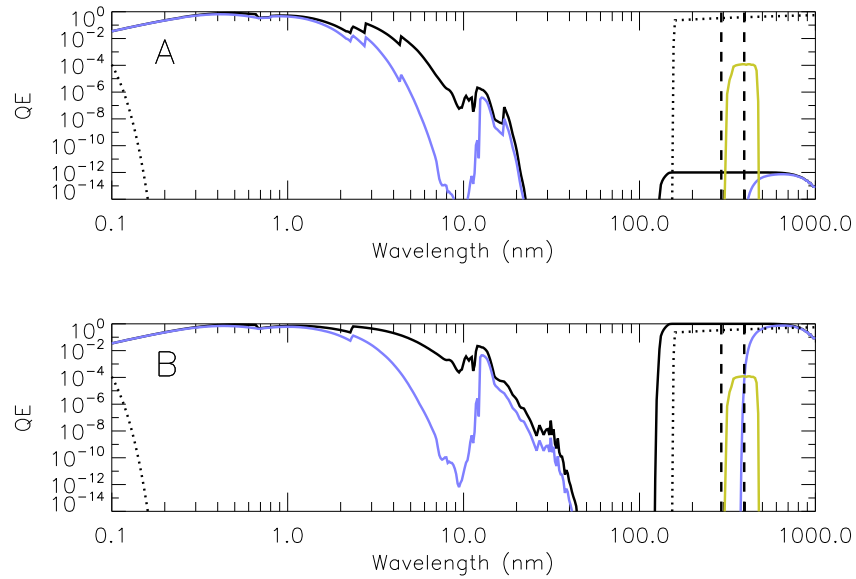

Figure 57. Quantum efficiency of the SXT CCD with (A) and without (B) an entrance filter. The blue curve denotes portions of the CCD pixel covered by the polysilicon gate. The black curve is the part of the pixel with no overlying gate structure. The other curves are, (1) dotted curve: transmission of the quartz defocus lens (4mm thick); (2) yellow curve: transmission bandpass of the SXT aspect sensor optics. The vertical broken lines show the positions of the valence (left) and conduction (right) bands of the bulk silicon beneath the insulating oxide layer.

positively charged holes migrate to the oxide-silicon interface, upsetting the voltage potential of the pixel. Laboratory experiments demonstrated that UV radiation more energetic than the silicon valence band (292 nm), which is absorbed in the bulk silicon very near the oxide-silicon interface (UV flood), results in photo-emission of electrons from the bulk silicon into the oxide – neutralizing the positive charge of the holes produced in the oxide by ionizing radiation. Radiation shortward of the conduction band but longward of the valence band,
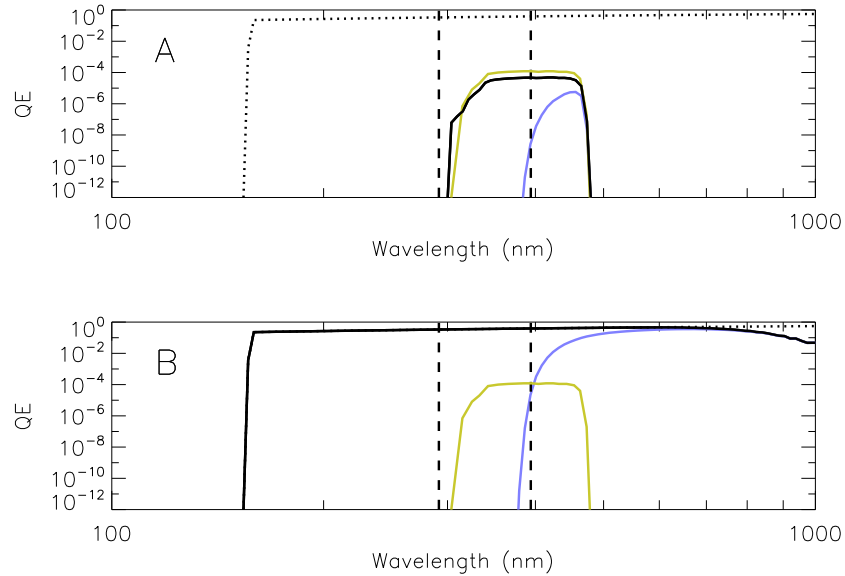
Figure 58. Detail of quantum efficiency of the CCD in the ultra-violet with (A) and without (B) the aspect sensor optics in place and with the quartz defocus lens included in the computation. Description of curves are the same as for Figure 57. The dotted line in A, transmission of the quartz lens, is shown for reference only as this optical element plays no role in system transmission when the aspect sensor assembly is included.

which we termed a blue-light flood, is believed to be less effective but better than nothing.

Figures 57 and 58 clearly demonstrate the response differences of the 2 halves of each CCD pixel. Figure 57 does not include the affect of SXT aspect optics and the quartz defocus lens whereas Figure 58 panel A does include both and panel B the quartz lens alone. Figure 57 shows that, in the visible beyond 400 nm, the 2 halves of the CCD are similar. However, the blue-light and UV floods, especially after 13 November 1992, should be much more effective for the x-ray sensitive half of the CCD than for the gate half. Perhaps this accounts for the radiation damage features in the optical images persisting at the 1 percent level throughout the mission.

10.2.2. CCD Overexposure Glitches

Severe x-ray overexposure of the CCD creates a temporary area of charge trapping that releases charge as the CCD is read out, producing a vertical trail of signal enhancement, a "glitch", above the overexposed region. This effect is illustrated in Figure 59. Note that the intensity of the glitch, while it appears stronger in the short exposure, is actually almost independent of exposure duration. This is because the signal enhancement is caused by charge pickup from the damaged area as the image is clocked out. There will be a small dependence
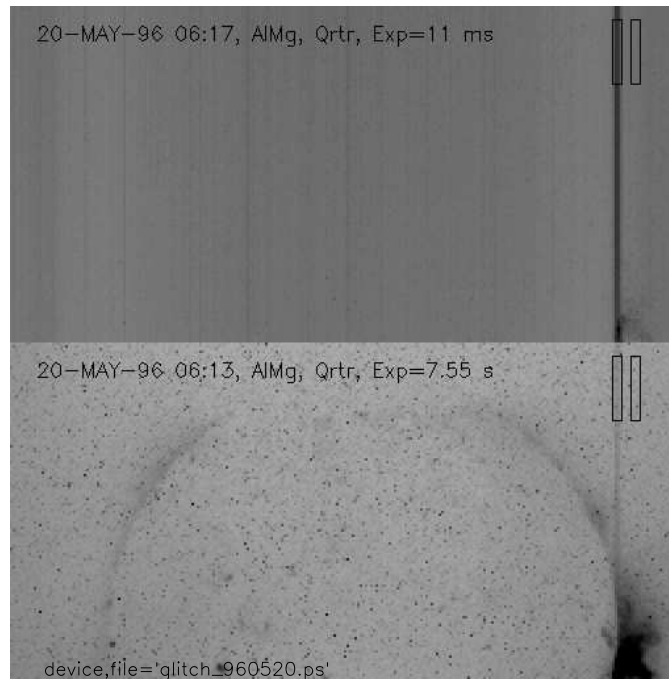
Figure 59. Long and short exposure QR images illustrating the large glitch of May 1996. The boxes show the sampling locations for the light curves of the following figure.

upon exposure time because additional x-ray exposure has a tendency to "charge up" the traps.

The constancy with exposure is demonstrated in Figure 60 where the top panel shows the average signal within the glitch for quarter resolution (QR) exposures ranging from 8 ms to 7.6 sec, uncorrected for stray light or normal dark current. Note that the glitch enhancement is not proportional to exposure but is within a factor of 2.5 in DN for all exposures whereas the exposure times are different by a factor of almost 1000. The lower panel shows signals (from the < 1 sec exposures) with the average signal in the adjacent box subtracted. The negative values reflect the fact that these data are not corrected for stray visible light. The RH box is in a slightly higher leak intensity area than the LH box.

The lower panel of Figure 60 reveals some interesting properties of glitch creation and decay. This particular glitch resulted from the upload of a PFI table on 18-may-96 04:02 that kept the shutter open most of the time. Throughout this period the GOES level was in the A range or below, and falling. Note that the glitch first appeared at about noon on 19 May, some 32 hours after the table upload. The dark current signal gradually built up over the next 12 hours until a standard table was uploaded at 19 May 1996 23:30, indicated by the leftmost vertical dashed marker on the plot. These data demonstrate that there is some threshold level of ionizing radiation damage beyond which a dark current glitch begins to appear.
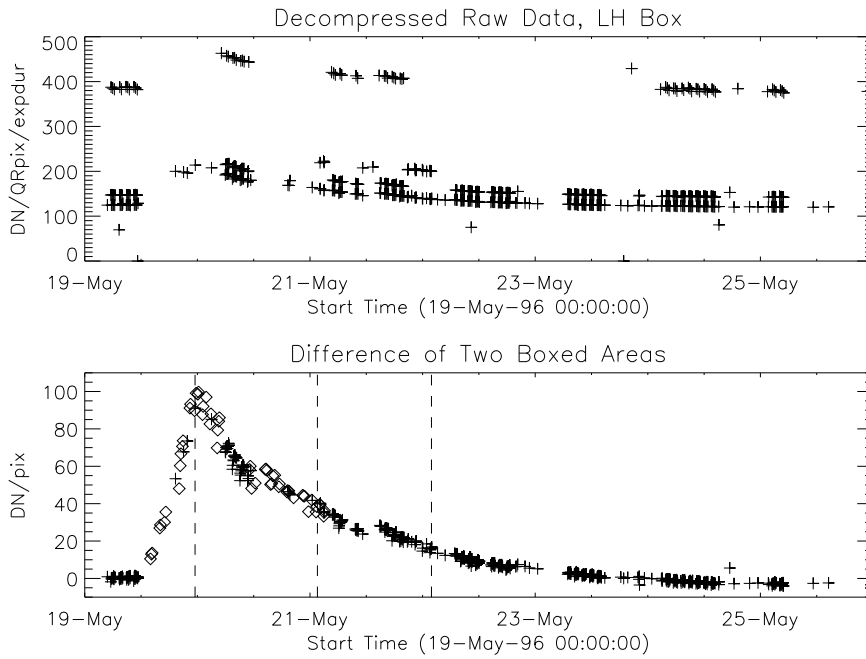
Figure 60. Rise and decay of the May 1996 glitch. In the lower panel the diamonds are glitch data from HR exposures shifted upwards by a factor of 2.4 to fill in the glitch-curve gap. Vertical dashed lines are times of table uploads from Kagoshima Space Center.
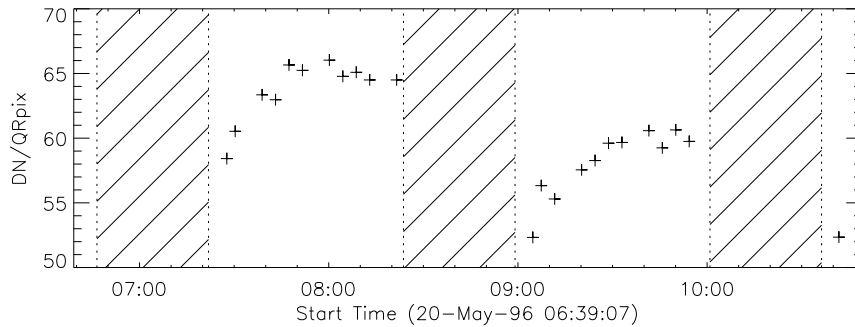

Figure 61. Orbital recharging of glitch following morning interval. Quarter resolution, 668 ms exposures. Cross-hatched intervals are orbit night.

The decay of the glitch is interrupted a couple of times by some observing activity which pumped the damaged area back up a bit. As shown in Figure 61, after each orbit night the glitch is substantially reduced by the morning UV flood. During the day the x-ray exposure steadily increases the glitch intensity. This is in contrast to normal dark signal (see section 10.4.1) amplitude which is high immediately after the UV flood and decreases through orbit day.
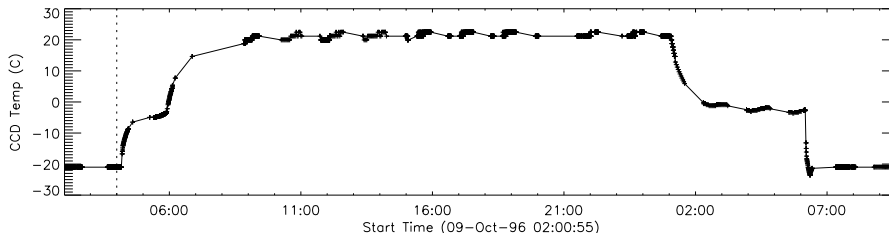
Figure 62. CCD bakeout of October 1996. The vertical dotted line shows when bakeout began.
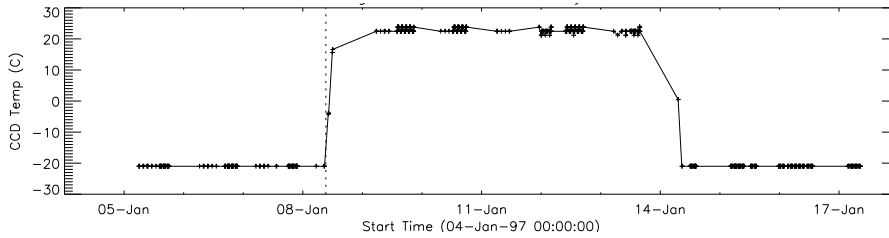
Figure 63. Extra-long CCD bakeout of January 1997. The vertical dotted line shows when bakeout began.

This study was undertaken to try to figure a way to improve the dark correction of glitches. Given the time variability of glitching there seems no obvious way to automatically correct for glitches. There is no evidence, at the level of overexposure seen here, that the sensitivity of the CCD to soft x-rays in the glitch source region has been affected.

10.3. CCD Bakeouts

Early in the *Yohkoh* mission it was observed, from absorption "dashes" in SXT full resolution (FR) images, that contamination was collecting on the surface of the CCD. In January of 1992 a series of warmings of the CCD to room temperature ($+20°$C, termed "bakeouts") was initiated to evaporate off the contaminating material. Careful examination of FR PFI images indicate that the contaminating material tended to disappear at a temperature of $0°$C although the extremely low ambient pressure would seem to rule out water ice as the contaminant. Bakeouts continued throughout the mission although late in the mission the evidence for contamination was never evident in the x-ray images. It took a very long time for the outgassing products to escape from the SXT and spacecraft. The intervals and duration of CCD bakeout, and the maximum CCD temperatures achieved are listed in ylstone.physics.montana.edu/ylegacy/ yo_dates/warm_ccd.html. The time profile of typical bakeouts are illustrated in Figures 62 and 63.

The bakeouts helped considerably to control dark current as illustrated in Figure 64. This figure was prepared from 7734 quarter resolution (QR) dark frames with an "exposure" time of 1 ms (DPE=2). For each image, row 15 was subtracted from row 250 to eliminate digital offsets, pedestal, etc., to yield the
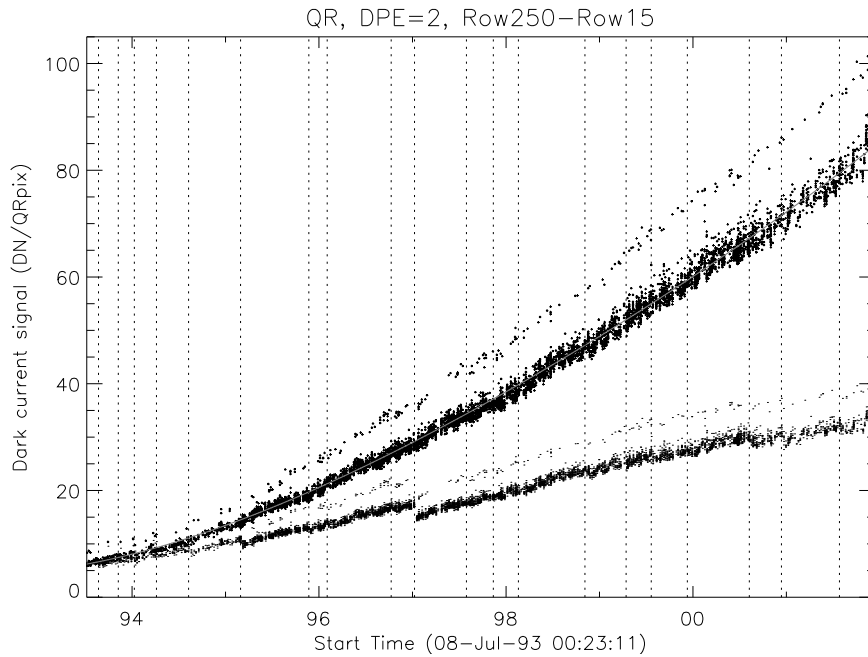
Figure 64. Lower curve: Actual SXT dark current signal $(0.46 \text{ sec})^{-1}$ $(\text{QR pixel})^{-1}$. Upper curve: Adjusted dark current signal with all bakeout down-steps removed. The overlaid line is a fourth order fit to the adjusted data. CCD bakeouts are indicated by vertical dotted lines. The elevated dots are data obtained shortly after the end of the UV flood.

pure dark current signal. The dark signal accumulation time is set by the image readout rate of 131 072 pixels sec^{-1}, independent of on-chip pixel summation. Thus, the dark signal accumulation time for this analysis was the time to readout a 256 pixel row (0.002 sec) × 215 rows or 0.43 sec. The relatively large decrease in January 1997 is associated with the extra long (143 hour) bakeout illustrated in Figure 63.

10.4. SXT Dark Frames

10.4.1. SDC Orbit Correction

There is a drift in dark signal throughout each daylight pass of the SXT orbit, engendered by the UV flood at each orbit sunrise (Acton, 1996). The adjusted curve in Figure 64 provides a smooth data set for study of dark signal as a function of time since UV flood. These results are displayed in Figure 65 which displays the dark signal versus time since UV flood and our standard orbit-correction algorithm, derived in 1994 (Acton, 1994). Compared to other sources of error the algorithm is adequate beyond four or five minutes past the end of the UV flood. For routine analysis, dark frames acquired earlier then 5.5 minutes after orbital sunrise are not used. SXT analysis software, e.g., *sxt_prep.pro* include orbit-dependent dark signal correction by default.
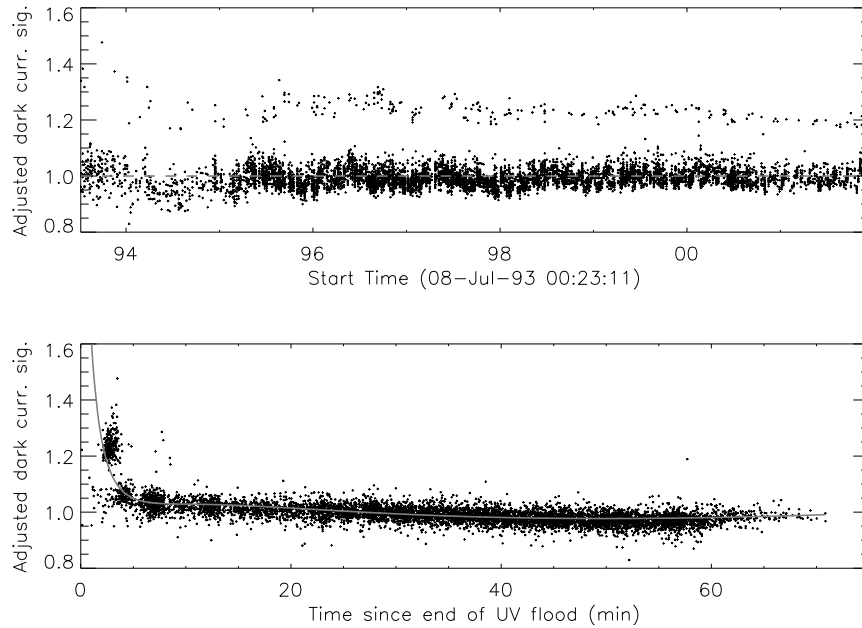
Figure 65. Upper panel: Adjusted (long-term increase removed) CCD dark signal versus time. Lower panel: Adjusted dark current versus time since end of morning interval. The overlaid line is the 1994 dc_orbit_correction algorithm.

10.4.2. Morning Interval Without UV Flood

The analysis reveals another unexpected feature, better illustrated in Figure 66. Note several very early dark frames, without significant enhancement, in the lower left of the figure. All of these anomalous dark frames were obtained in connection with special operations at Kagoshima Space Center, involving manual commanding, that disabled the morning UV flood (Dr. T. Shimzu, private communication). They are useful in demonstrating the strong transient effect of the UV flood on the CCD dark signal.

10.5. CCD Camera Read Noise and Pedestal

Our best estimate of the read noise and pedestal (static offset of zero signal) can be obtained by analysis of 1 ms dark exposures (DPE=2). For the bottom rows of the image there is, effectively, no time to accumulate dark current signal. However, the first **n** rows must be avoided because of charge bleedback from the serial register. Our first task is to determine which row to use for read noise/pedestal analysis for each pixel summation resolution.

10.5.1. Full Resolution Case

Full resolution (FR) dark images with DPE=2 were not routinely taken before the end of March 1993. Fortunately, 3 such images of the bottom half of the CCD were acquired shortly before the 14 November 1992 entrance filter failure.
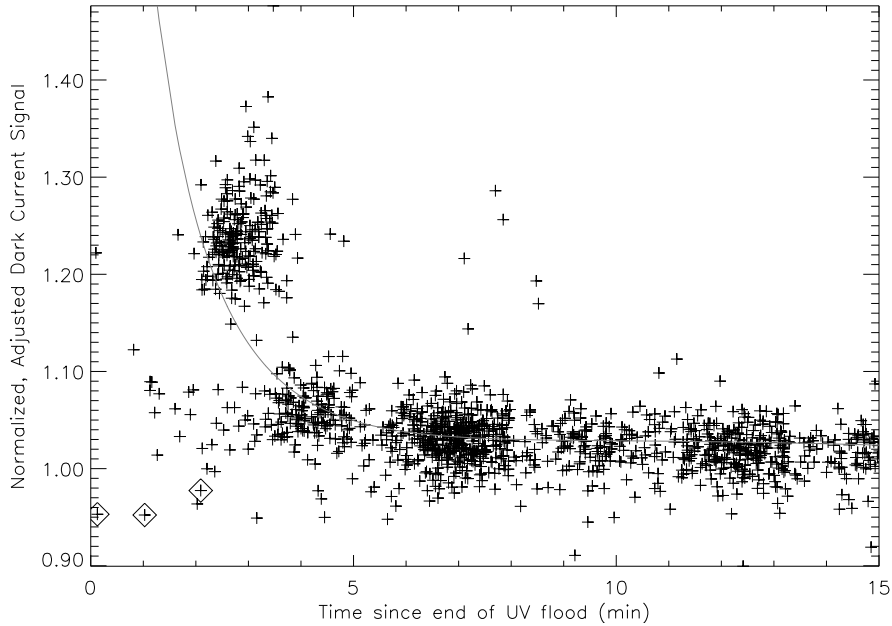
Figure 66. Magnified version of Figure 65 bottom. The diamonds identify three dark frames obtained on 5 December 1997 as part of a special high rate dark frame table designed to study orbital dark current effects.

```
26-OCT-92   20:07:25
27-OCT-92   02:52:13
10-NOV-92   11:34:52
```

The mean signal levels in the FR darks, the mean signal in row 20, the mean signal in row 500, and the pure dark current in the difference of rows 500 and 20 are illustrated in Figure 67 for the entire mission. Note the large jump in the readnoise+pedestal signal (row 20, second curve from top in figure) caused by the November 1992 entrance filter failure with relatively little variation thereafter. On the contrary, the pure dark current signal (bottom curve) does not show a significant step associated with the November 1992 entrance filter failure.

10.5.1.1. FR Read Noise and Pedestal, pre-November 1992 The mean signal in the three pre-November 1992 SDCs noted above are so nearly the same (13.12, 13.12, and 13.10 DN FPpix^{-1} expdur^{-1}) that the three are summed to obtain better statistics for analysis to determine the best row to use for further analysis of read noise and pedestal. A straight line fit to the resulting curve for rows above, say, row 30 can be extrapolated to row 0 to yield the effective offset pedestal. Inspection of where the data deviate from this straight line fit at low row numbers because of bleed-back from the serial register show which row is appropriate for use in estimating pedestal plus read noise. The statistics of the signals along that row quantify the read noise. This analysis is presented in Figure 68.
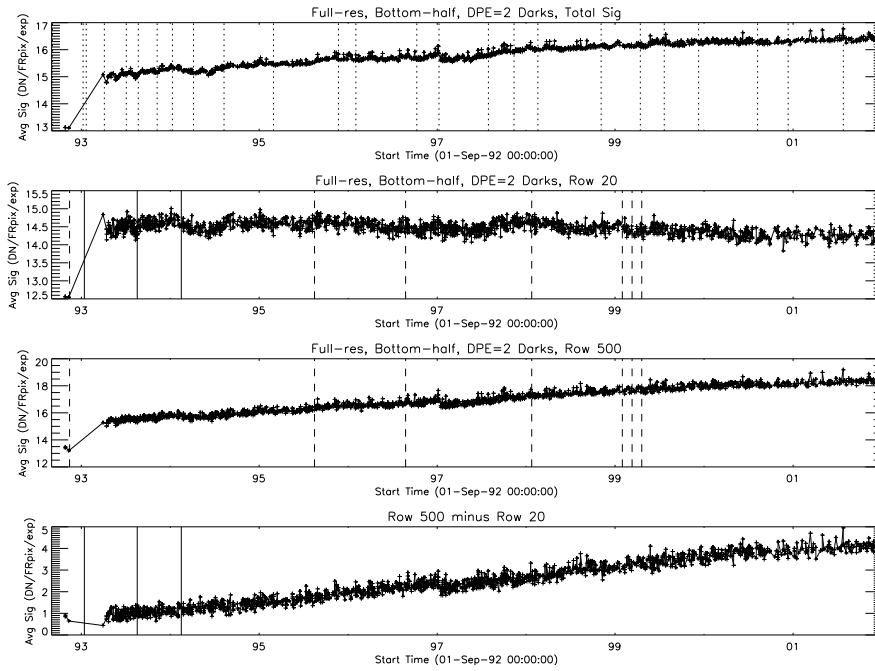
Figure 67. Signals in full resolution dark frames with DPE=2. Note titles for details. The dotted vertical lines in the top panel denote CCD bakeouts. The solid vertical lines denote times when the duration of morning UV flood was changed. The broken vertical lines denote the times of entrance filter failures.
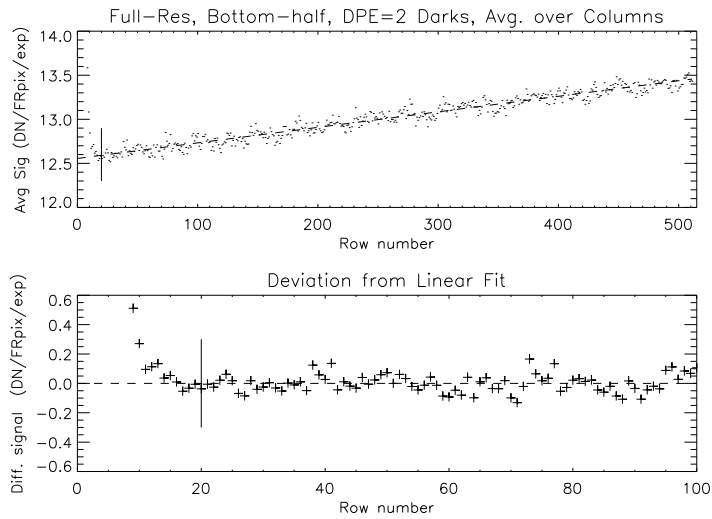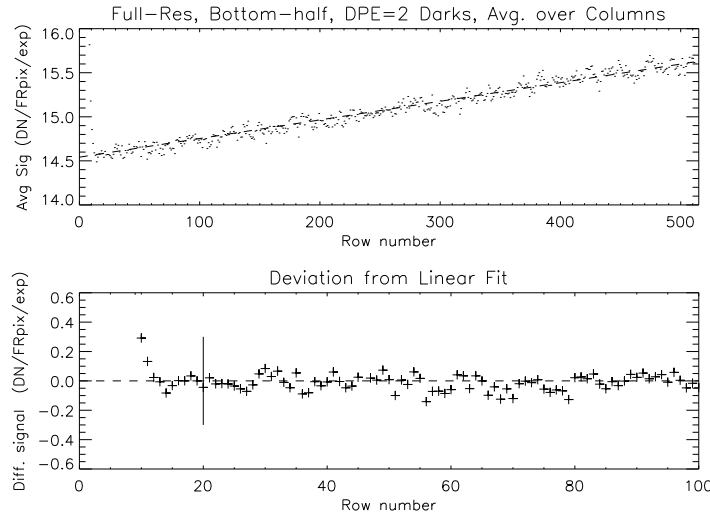

Figure 68. Upper: Fit to dark current wedge for pre-November 1992 FR dark images. Lower: Deviation of signals from fit for bottom 100 rows. The vertical bars at Row number 20 indicate where the CCD read noise is measured.

Figure 69. Upper: Fit to dark current wedge for September 1993 FR dark images. Lower: Deviation of signals from fit for bottom 100 rows.

The intercept of the fit, 12.559 DN, is the offset pedestal. The slope of the fit, (0.226 DN FRpix^{-1} s^{-1}), gives the dark current rate. The 0.00781250 sec is the time to read out a single 1024 pixel row at 131,072 pixels sec^{-1}. The read noise is given by the statistics of the signal in row 20. For the three SDCs used in this analysis the standard deviations are 0.881, 0.901, and 0.891 for an average read noise of 0.89 DN FRpix^{-1}.

10.5.1.2. FR Read Noise and Pedestal, post-November 1992 It is evident from Figure 67 that the non-dark current signal was increased by about two DN FRpix^{-1} as a result of the November 1992 entrance filter failure. The three FR darks in 1993 and three in 2001 are analyzed in order to study the variation in the non-dark current signals. The 1993 darks were chosen to have time since sunrise between 40 and 45 minutes.

```
28-SEP-93   12:55:55
28-SEP-93   14:34:03
28-SEP-93   16:11:07
```

For this set the pedestal is 14.5422 DN FRpix^{-1}, the dark current rate is 0.270 DN FRpix^{-1} sec^{-1} and the read noise is 1.07 DN FRpix^{-1}. The data and linear fit are displayed in Figure 69.

The situation at the end of the mission is illustrated in Figure 70. The 3 SDCs analyzed, all between 45 and 55 minutes since sunrise, were:

```
27-NOV-01   01:54:54
27-NOV-01   08:22:30
27-NOV-01   09:55:56
```

At the end of the mission the pedestal was 14.1440 DN HRpix^{-1}, the dark current rate was 1.051 DN FRpix^{-1} sec^{-1}, and the read noise was 1.13 DN
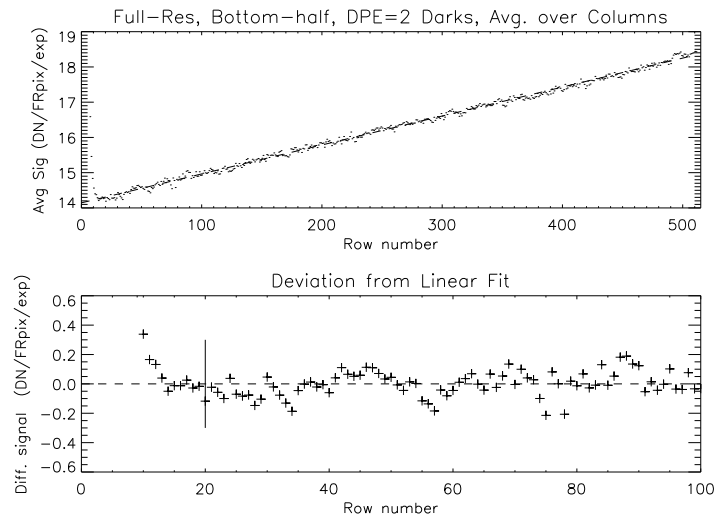
Figure 70. Upper: Fit to dark current wedge for November 2001 FR dark images. Lower: Deviation of signals from fit for bottom 100 rows.

FRpix^{-1}. Note that the read noise and pedestal changed very little since 1993 whereas the dark current rate increased by a factor of 4.2. The step in the pedestal and read noise related to the November 1992 entrance filter failure is probably caused by an increase in spurious charge in the serial register of the CCD (the properties are consistent with this). It is not clear why or how the change in CCD environment associated with the filter failure engendered this change.

10.5.1.3. FR Read Noise and Pedestal, entire mission The read noise and pedestal+spurious offset is required for determination of detector gain by the photon transfer technique. Figure 71 shows the pedestal+spurious (average of Row 20) and read noise (standard deviation of Row 20) for all qualified FR dark frames throughout the mission.

10.5.2. Half Resolution Case

For binned images all background signals are increased. This is illustrated for HR DPE=2 dark frames in Figure 72. In this case there is a single dark frame acquired shortly after launch in 1992 that indicates the slight decrease in row 15 signal and, in the bottom panel, the approximately linear increase in dark current from the very beginning of the mission. Also note the apparent high signals in the bottom panel. These are all from dark frames acquired within a few minutes of the end of the UV flood. The evident block of dark frames in mid 1999 resulted from a command table error.

Our ability to determine read noise and pedestal+spurious depends upon the characteristics of the bottom rows of the CCD. This is illustrated for the HR case in Figure 73. It appears that row 15 is a good choice for this analysis.
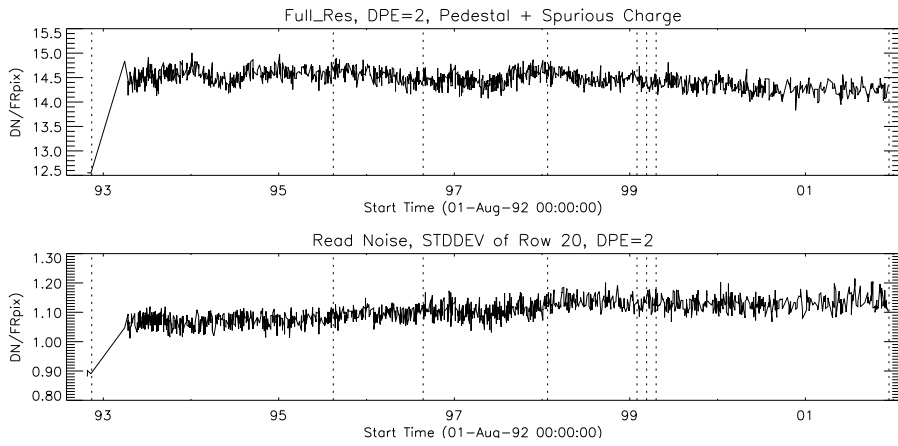
Figure 71. Full resolution pedestal+spurious and read noise. Upper: Pedestal plus spurious charge. Lower: Read noise. The vertical dotted lines denote the times of entrance filter failure.
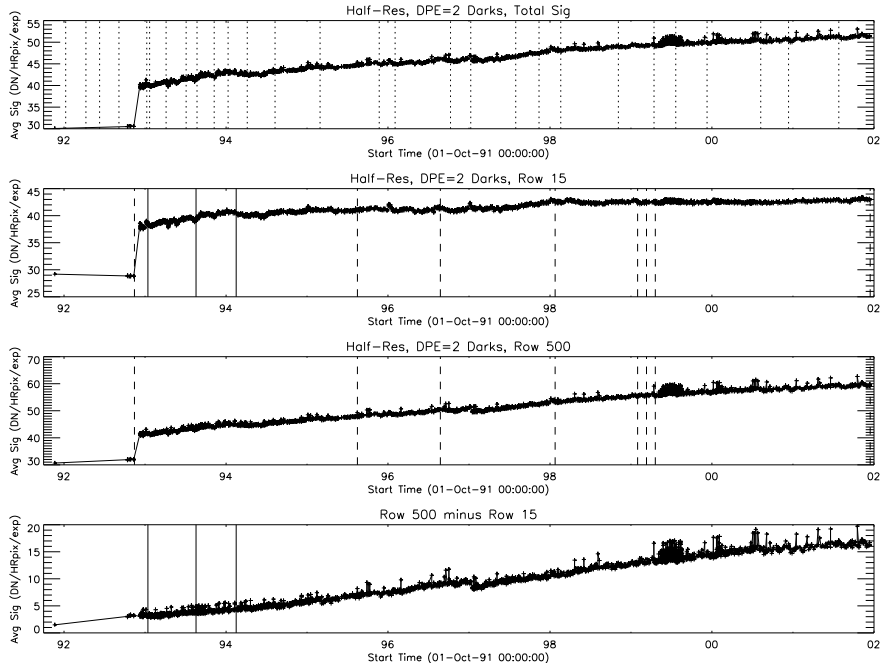

Figure 72. Signals in half resolution dark frames with DPE=2. The vertical markers are the same as in Figure 67.

The evolution of HR read noise and pedestal+spurious DC offset is illustrated in Figure 74 for the mission.
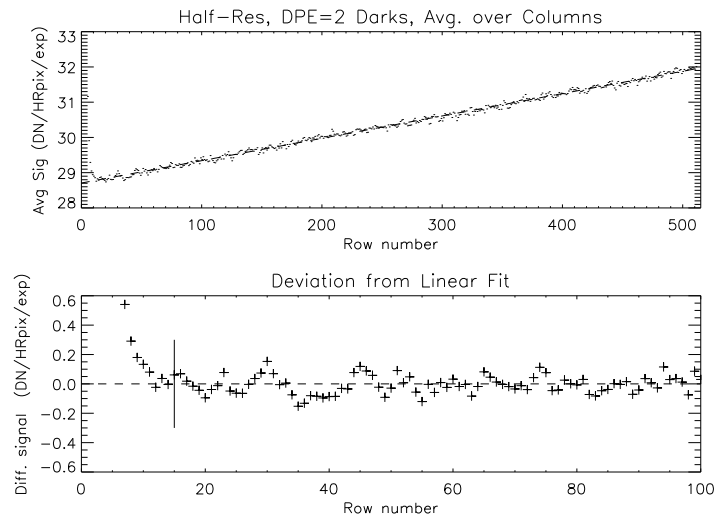
Figure 73. Upper: Fit to dark current wedge for October 1992 HR dark images. Lower: Deviation of signals from fit for bottom 100 rows.
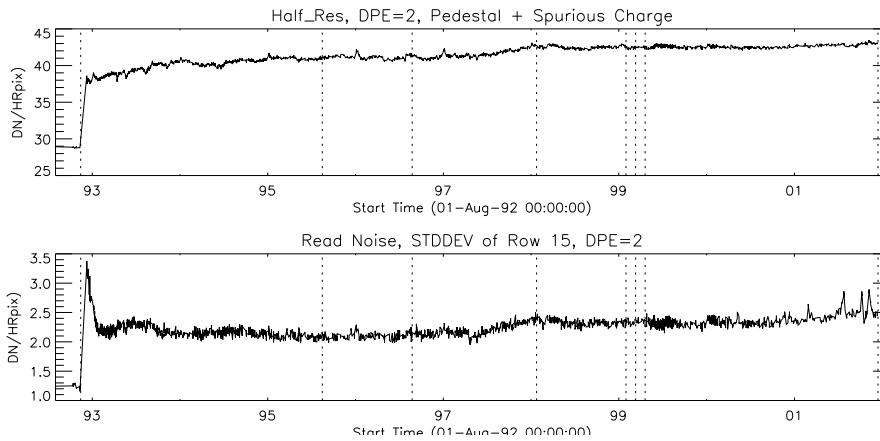

Figure 74. Half resolution pedestal+spurious and read noise. Upper: Pedestal plus spurious charge. Lower: Read noise. The vertical dotted lines denote the times of entrance filter failure.

10.5.3. Quarter Resolution Case

Quarter resolution DPE=2 dark frames were routinely acquired throughout the mission as dark signal monitors so are particularly useful for secular analysis. For example, there are 7734 dark frames represented in QR Figure 75. The corresponding number for HR is 3106 and for FR it is 1674. Figures 75 and 77 from this QR data base dramatically illustrate the impact of the November 1992 entrance filter failure and the period of several months it took for the CCD to reach a new equilibrium with the more intense and spectrally different UV flood. The QR dark current wedge and choice of row for pedestal+spurious charge and read noise analysis is detailed in Figure 76.
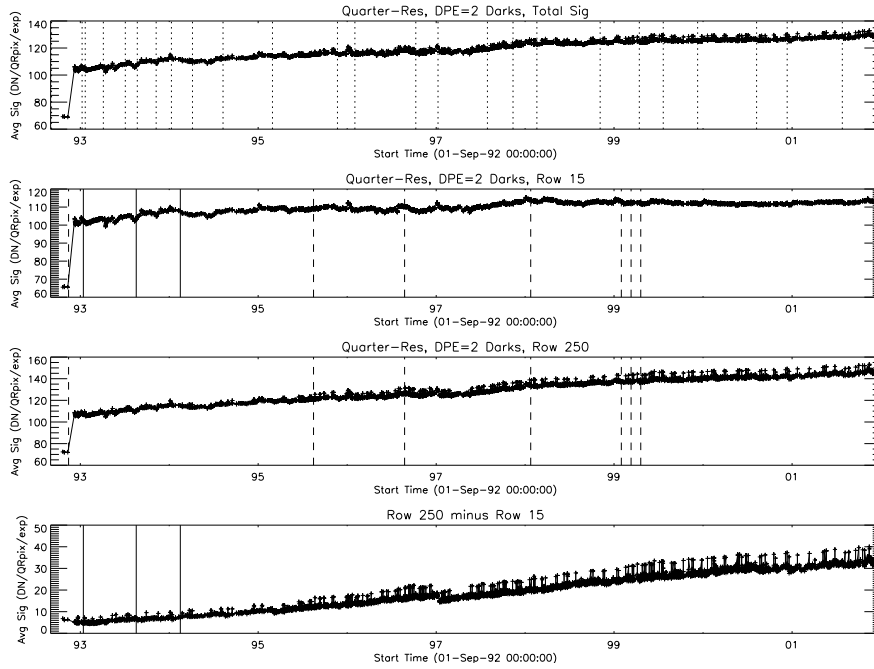
Figure 75. Signals in quarter resolution dark frames with DPE=2. Vertical markers are the same as in Figure 67.
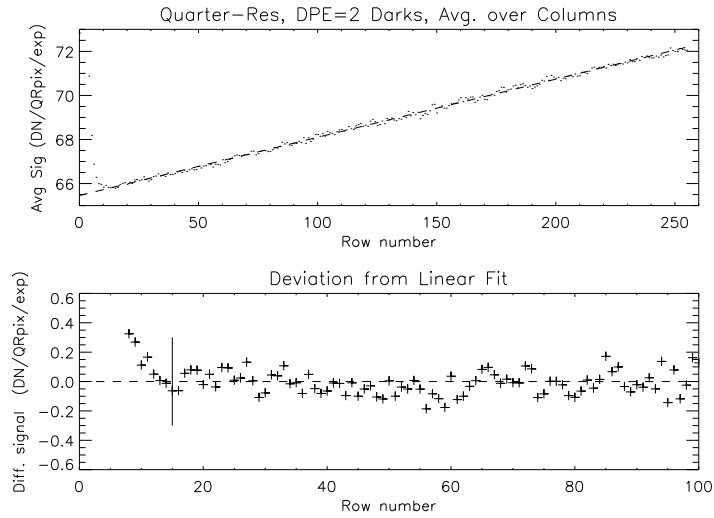

Figure 76. Upper: Fit to dark current wedge for October 1992 QR dark images. Lower: Deviation of signals from fit for bottom 100 rows.
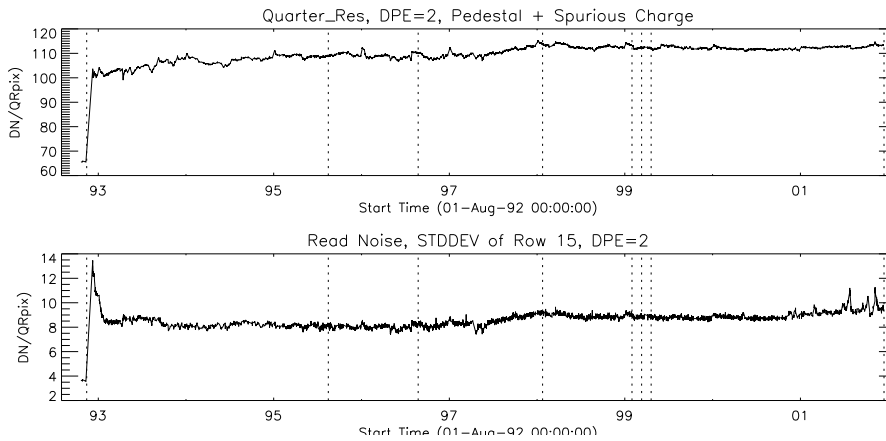
Figure 77. Quarter resolution pedestal+spurious and read noise. Upper: Pedestal plus spurious charge. Lower: Read noise. The vertical dotted lines denote the times of entrance filter failure.

10.6. Dark Frame Selection Criteria

In preparing data for this dark frame study and selecting images for the SXT dark frame (SDC) data base the following selection criteria are used:

1. Percent data = 100.
2. Full frame image (FFI).
3. Filter-wheel A in open position.
4. Not in CCD bakeout.
5. Not in South Atlantic anomaly.

Despite this care several problem dark frame cases slipped through. These images have been removed from the SDC dark frame data base.

11. Summary

By any standard, *Yohkoh* was an eminently successful scientific mission as evidenced by the more than 1500 refereed publications traced to it as reported by http://www.lmsal.com/~aschwand/publications/yohkoh.html.
The SXT on *Yohkoh* produced x-ray observations of the active sun and corona from October 1991 until December 2001 that remain unique and valuable because of the epoch of the observations, the quality of the images, and the spectral response of the telescope. The S-054 x-ray photographs from Skylab (14 May 14 1973 to 8 February 1974) (Batchelor, 1995) dramatically demonstrated the worth of x-ray movies for studies of solar activity. The SXT carried on that tradition with greatly improved resolution, cadence, quantitative accuracy, usability, and accessibility. The purpose of this paper has been to document many important aspects of SXT data and their preparation for serious future users. Material such as outgassing problems, filter failures and CCD performance has been treated in sufficient detail to, hopefully, be of some benefit to future space experimenters.

I dedicate this work to the memory of esteemed *Yohkoh* colleagues who have passed away; K. Kai, I. Kondo, T. Kosugi, B. LaBonte, T. Metcalf, M. Oda, T. Takakura, K. Tanaka, and Y. Uchida.

Appendix

A. ATT File Format

The ATT data base comprises weekly files named, e.g., `att99_33.18`. Here, 99 refers to the year 1999, 33 designates week 33 of that year, and 18 identifies the version number. These weekly files are not strictly calendar weeks because *Yohkoh* daylight passes are not permitted to be broken by a week boundary. Thus, `att99_33.18` could begin up to 90 minutes after Saturday midnight and include data up to an hour into week 34.

There is one record in the ATT file for each and every SXT image. The records are in the form of IDL structures. E.g.,

```
** Structure ATT_SUMMARY_REC, 9 tags, length=24, data length=24:
   TIME            LONG          78564340
   DAY             INT           4639
   DP_MODE         BYTE       141
   DP_RATE         BYTE       128
   PNT             LONG      Array[3]
   STATUS1         BYTE         2
   STATUS2         BYTE        12
   ADS             BYTE         1
   SPARE           BYTE      Array[1]
```

Where the tag PNT contains the attitude information, i.e.,

PNT(0)/100. is the X coordinate of sun center in CCD pixels,

PNT(1)/100. is the Y coordinate of sun center in CCD pixels, and

PNT(2)/36000. is the S/C roll angle in degrees (CW positive).

TIME and DAY are time codes and the other tags provide housekeeping information.

References

Acton, L.: 1994, *Orbital Variation of SXT Dark Current*. http://solar.physics.montana.edu/ ylegacy/obs_notes/html/Orbital_Dark_Variation.html. [Acton1994]

Acton, L.: 1995, *Azimuthal Time Variation of X-ray Scatter*. http://solar.physics.montana. edu/ylegacy/obs_notes/html/Variations_in_xray_scatter.html. [Acton1995]

Acton, L.: 1996, *Orbit Variation of CCD Dark Current*. http://solar.physics.montana.edu/ ylegacy/obs_notes/html/FMS_DARKSIGNAL_CHANGE.html. [Acton1996]

Acton, L.: 1997, *Statistical Properties of SXT Darkframes*. http://solar.physics.montana.edu/ ylegacy/obs_notes/html/DARKFRAME_STATISTICS.html. [Acton1997]

Acton, L.: 1999, *SXT Calibration Note 13. Entrance annulus of SXT*. http://solar.physics. montana.edu/ylegacy/documents/sxt_cal_note/SXT_cal_note_13.pdf. [Acton1999]

Acton, L.: 2014, *Long-term Variation of Diffuser Images*. http://solar.physics.montana.edu/ ylegacy/obs_notes/html/Diffuser_longterm_variation.html. [Acton2014]

Acton, L.W.: 1992, *SXT Calibration Note 29. Preliminary Calibration of SXT Flight X-ray Filters*. http://solar.physics.montana.edu/ylegacy/documents/sxt_cal_note/SXT_cal_note_ 29.pdf. [Acton1992]

Acton, L.W., Morrison, M.D., Janesick, J.R., Elliott, T.S.: 1991, Radiation concerns for the Solar-A soft x-ray telescope. In: Blouke, M.M. (ed.) *Society of Photo-Optical Instrumentation Engineers (SPIE) Conference Series*, *Society of Photo-Optical Instrumentation Engineers (SPIE) Conference Series* **1447**, 123. ADS. [Acton1991]

Aschenbach, B.: 1985, X-ray telescopes. *Reports on Progress in Physics* **48**, 579. DOI. ADS. [Aschenbach1985]

Batchelor, D.: 1995, *Solar X-ray Images From Skylab Available Over the Internet*. http:// nssdc.gsfc.nasa.gov/nssdc_news/march95/06_d_batchelor_0395.html. [Batchelor1995]

Dever, J., Banks, B., de Groh, K., Miller, S.: 2012, *Degradation of Spacecraft Materials*, 2nd edn. Elsevier, ???, 465. Chap. 23. ISBN 978-1-4377-3455-3. [dever2012]

Doschek, G.A., Strong, K.T., Tsuneta, S.: 1995, The bright knots at the tops of soft X-ray flare loops: Quantitative results from YOHKOH. *Astrophys. J.* **440**, 370. DOI. ADS. [Doschek1995]

Drummond, D.G.: 1936, The infra-red absorption spectra of quartz and fused silica from 1 to 7.5μ [II] - experimental results. *Proceedings of the Royal Society of London, Series A, Mathematical and Physical Sciences* **153**, 328. [drummond1936]

EICA: 1990, *Soft X-ray Telescope (SXT) for Solar-A Experiment Interface Control Agreement*, Lockheed Palo Alto Research Laboratory. http://solar.physics.montana.edu/ylegacy/ documents. [eica1990]

Foley, C.R., Culhane, J.L., Acton, L.W.: 1997, Yohkoh Soft X-Ray Determination of Plasma Parameters in a Polar Coronal Hole. *Astrophys. J.* **491**, 933. ADS. [Foley1997]

Fuller, R., Lemen, J., Acton, L.: 1994, *SXT Calibration Note 37. SXT X-ray Vignette Function*. http://solar.physics.montana.edu/ylegacy/documents/sxt_cal_note/SXT_cal_note_37.pdf. [Fuller1994v]

Gburek, S., Sylwester, J.: 2002, Search for Compact x-ray Sources in sxt Observations. *Solar Phys.* **206**, 273. DOI. ADS. [Gburek2002]

Green, M.A., Keevers, M.: 1995, Optical properties of intrinsic silicon at 300 K. *Progresss in Photovoltaics* **3**, 189. [green1995]

Grillot, P., Cruz, T.: 1990, *Soft X-Ray Telescope Aspect Telescope Design Note No.31*. In SXT Expt. Interface Contrl. Agrmnt., p. C-4. http://solar.physics.montana.edu/ylegacy/ documents/SXT_Expt_Intrface_Contrl_Agrmnt.pdf. [grillot1990]

Hara, H., Tsuneta, S., Acton, L.W., Bruner, M.E., Lemen, J.R., Ogawara, Y.: 1994, Temperatures of coronal holes observed with the YOHKOH SXT. *Pub. Astron. Soc. Japan* **46**, 493. ADS. [Hara1994]

Henke, B.L., Gullikson, E.M., Davis, J.C.: 1993, X-Ray Interactions: Photoabsorption, Scattering, Transmission, and Reflection at E = 50-30,000 eV, Z = 1-92. *Atomic Data and Nuclear Data Tables* **54**, 181. DOI. ADS. [Henke1993]

Janesick, J.R.: 2001, *Scientific charge-coupled devices*, *SPIE Press monograph, xvi*, Optical Engineering Press, Bellingham, WA. [Janesick2001]

Kitamura, R., Pilon, L., Jonasz, M.: 2007, Optical constants of silica glass from extreme ultraviolet to far infrared at near room temperature. *Applied Optics* **46**, 8118. DOI. ADS. [kitamura2007]

Kosugi, T., Masuda, S., Makishima, K., Inda, M., Murakami, T., Dotani, T., Ogawara, Y., Sakao, T., Kai, K., Nakajima, H.: 1991, The hard X-ray telescope (HXT) for the Solar-A mission. *Solar Physics* **136**, 17. DOI. ADS. [Kosugi1991]

Kramm, J.R., Thomas, N., Keller, U.E.: 1993, *The CCD Detectors of the Halley Multicolour Camera After Seven Years in Flight*. Technical Report MPAE-W-1000-93-22, Max-Planck Institut für Aeronomie. [Kramm1993]

LaBonte, B.: 1996, *On Orbit Measurementof SXT CCD Electronic Gain*. http://solar.physics.montana.edu/ylegacy/obs_notes/html/sxt_ccd_gain.html. [LaBonte1996]

Lemen, J.R.: 1992, *SXT Calibration Note 30. Effective Area of SXT Mirror (In-Flight)*. http://solar.physics.montana.edu/ylegacy/documents/sxt_cal_note. [Lemen1992]

Lemen, J.R.: 1993, *SXT Calibration Note 31. SXT X-ray Effective Area*. http://solar.physics.montana.edu/ylegacy/documents/sxt_cal_note/SXT_cal_note_31.pdf. [Lemen1993]

Lemen, J.R., Hudson, H.S.: 1990, *SXT Calibration Note 5. The SXT X-ray Neutral-density Filters*. http://solar.physics.montana.edu/ylegacy/documents/sxt_cal_note. [Lemen1990]

Martens, P.C., Acton, L.W., Lemen, J.R.: 1995, The point spread function of the soft X-ray telescope aboard YOHKOH. *Solar Phys.* **157**, 141. DOI. ADS. [Martens1995]

Narukage, N., Sakao, T., Kano, R., Hara, H., Shimojo, M., Bando, T., Urayama, F., Deluca, E., Golub, L., Weber, M., Grigis, P., Cirtain, J., Tsuneta, S.: 2011, Coronal-Temperature-Diagnostic Capability of the Hinode/ X-Ray Telescope Based on Self-Consistent Calibration. *Solar Physics* **269**, 169. DOI. ADS. [Narukage2011]

Ogawara, Y., Takano, T., Kato, T., Kosugi, T., Tsuneta, S., Watanabe, T., Kondo, I., Uchida, Y.: 1991, The Solar-A Mission - an Overview. *Solar Physics* **136**, 1. DOI. ADS. [Ogawara1991]

Palik, E.D.: 1985, *Handbook of optical constants of solids*, *Academic Press Handbook Series*, Academic Press, New York, NY. [palik1985]

Philipp, H.R.: 1985, Silicon dioxide (SiO$_2$) glass. In: Palik, E.D. (ed.) *Handbook of optical constants of solids, Vol. I Academic Press Handbook Series*, Academic Press, New York, NY, 749. [philipp1985]

Preś, P., Kołomański, S.: 2009, Are Soft X-ray Flare Loop-top Sources Diffuse or Filamentary? *Central European Astrophysical Bulletin* **33**, 233. ADS. [Pres2009]

Sato, J., Matsumoto, Y., Yoshimura, K., Kubo, J., Masuda, S., Sawa, M., Suga, K., Yoshimori, M., Kosugi, T., Watanabe, T.: 2006, YOHKOH/WBS Recalibration and a Comprehensive Catalogue of Solar Flares Observed by YOHKOH SXT, HXT and WBS Instruments. *Solar Physics* **236**, 351. DOI. ADS. [Sato2006]

Shin, J., Sakurai, T.: 2013, Vignetting Effect in the Soft X-Ray Telescope Onboard Yohkoh: I. Numerical Simulation. *Solar Phys.*. DOI. ADS. [Shin2013]

Shin, J., Sakurai, T.: 2014, The Effect of the CCD Gate Structure in the Determination of the Undersampled Point Spread Function. *Solar Phys.* **289**, 2803. DOI. ADS. [Shin2014]

Shirts, P., Metcalf, T.R., Lemen, J.R., Freeland, S., Acton, L.W.: 2003, *SXT Calibration Note 41. Correcting Yohkoh/SXT X-ray Images for White Light Contamination*. http://solar.physics.montana.edu/ylegacy/documents/sxt_cal_note. [Shirts2003]

Spiga, D.: 2007, Analytical evaluation of the X-ray scattering contribution to imaging degradation in grazing-incidence X-ray telescopes. *Astron. Astrophys.* **468**, 775. DOI. ADS. [Spiga2007]

Švestka, Z., Uchida, U. (eds.): 1991, *The YOHKOH (SOLAR-A) Mission*, Kluwer, ??? ISBN 0-7923-1532-4, Reprinted from Solar Physics, Volume 136, No. 1, 1991. [redbook1991]

Takeda, A.: 2015, *Yohkoh Legacy Data Archive*. http://solar.physics.montana.edu/ylegacy/. [YLA2015]

Takeda, A., Acton, L., McKenzie, D., Yoshimura, K., Freeland, S.: 2009, Resident archive services of the yohkoh legacy data archive. *Data Science Journal* **8**, IGY1. DOI. [Takeda2009]

Tan, G.L., Lemon, M.F., French, R.H.: 2003, Optical properties and London dispersion forces of amorphous silica determined by vacuum ultraviolet spectroscopy and spectroscopic ellipsometry. *Journal of the American Ceramic Society* **86**, 1885. DOI. [tan2003]

Tsuneta, S., Acton, L., Bruner, M., Lemen, J., Brown, W., Caravalho, R., Catura, R., Freeland, S., Jurcevich, B., Owens, J.: 1991, The soft X-ray telescope for the SOLAR-A mission. *Solar Physics* **136**, 37. DOI. ADS. [Tsuneta1991]

Wuelser, J.P., Hudson, H.S., Nishio, M., Kosugi, T., Masuda, S., Morrison, M.: 1998, Precise Determination of the Coordinate Systems for the YOHKOH Telescopes and the Application of a Transit of Mercury. *Solar Physics* **180**, 131. ADS. [Wuelser1998]

Zhao, P., Van Speybroeck, L.P.: 2003, A new method to model x-ray scattering from random rough surfaces. In: Truemper, J.E., Tananbaum, H.D. (eds.) *X-Ray and Gamma-Ray*

Telescopes and Instruments for Astronomy., *Society of Photo-Optical Instrumentation Engineers (SPIE) Conference Series* **4851**, 124. DOI. ADS. [Zhao2003]